Atomic Scale Insights for Structure-Function Relationships on Model Catalytic Surfaces

A dissertation submitted by:

Paul L. Kress

In partial fulfillment of the requirements for the degree of:

Doctor of Philosophy, Chemistry

Tufts University

February 2022

Advisor: Prof E. Charles H. Sykes

Abstract

Heterogeneous catalysis is key to many industrial processes and is responsible for the production of trillions of dollars of goods a year. These catalytic processes are complex and are not fully optimized in terms of activity of the catalysis while maintaining high selectivity. Many of these catalytic processes use expensive transition metals such as Pt, Pd, and Rh, which themselves are costly and not earth abundant. Finding the optimal way to utilize these precious metals is of vital importance. This thesis follows a rational design approach whereby theory combined with surface science and practical catalysis give us insight into the fundamental mechanism and optimal structure for the reaction of interest.

The work in this thesis specifically looks at Ni, Pd, Cr, and Pt metals deposited in small amounts into Cu, Ag, and Au hosts. The effects of different ensembles of the group 10 metals were investigated for the ability to bind CO, H_2 dissociation, C-H, and O-H bond cleavage. By optimizing the amount of group 10 metal in the group 11 host, highly active and selective catalysts are formed. Specifically a class of catalysts called Single-Atom Alloys will be studied, these catalysts are active, CO tolerant, and highly selective. Pt in Cu will show its ability to dissociate H_2 and hydrogenate adsorbed ethyl groups on the surface. PtCrAg and NiAu will be optimized for their ability to non-oxidatively dehydrogenate ethanol to form acetaldehyde. The optimized geometry for NiAu catalyst to be able to activate the C-I bond in methyl iodide, and maintain the selective coupling to form ethane will be demonstrated. Lastly NiAu and PdAu will be examined at elevated pressures for their ability to bind CO and infrared studies will show the optimized ensemble and most strongly binding site for these catalysts are atop sites in the surface. Atomic scale resolution of these catalysts informs the structure-activity relationship of

these alloy catalysts. The atomic level details of several reactions and their intermediates are investigated through various different surface science techniques.

Acknowledgements

My time is graduate school was made enjoyable and successful with the help of many people, mainly, my teachers, friends, co-workers, collaborators, and least by not last my family. I would like to thank everyone for helping me through these years. I would like to first thank my advisor, Charlie Sykes, for being an amazing PI and always having great guidance. He was always there to talk about research and guide me, while also pushing me to improve as a scientist. Along with being a great P.I. in terms of science, he was also an amazing person outside of lab and I have enjoyed talking with him and have really appreciated the culture he has made in the lab to make things all around more enjoyable during my time here.

I would also like to thank my other committee members for being generous with your time. Professor Art Utz has been there any time I need to ask fundamental surface science questions and during meetings has always made me think about things in a very challenging, but fundamental way. Professor Samuel Thomas has always provided a great organic background to bounce ideas off of for trying random reactions in that space and understanding the scope of that field in more detail than I would have ever been able to do on my own. Also thank you to Anibal Boscoboinik for being my outside committee member, I have appreciated being in IMASC with you and I have truly enjoyed doing research at the Center for Functional Nanomaterials with you. I especially enjoyed that you have let me use the equipment down there liberally, and were always useful in providing me with good scientific input, especially when it came to the field of ambient-pressure analysis.

It was always very fun and exciting to work with various different collaborators during my time here, including, Romain Réocreux, Michail Stamatakis, Matthew Montemore, Shengjie Zhang, Georgios Giannakakis, and Maria Flytzani-Stephanopoulos. I have always enjoyed finding the connections between the work I have done and working that in to make more complete stories using computational power and chemical engineering.

Thank you to all the past and present members of the Sykes lab that have been here for my time and made it more enjoyable. Dr. Zhitao Wang, Dr. Matt Marcinkowski, Dr. Natalie Wasio, Dr. Amanda Larson, Dr. Andy Therrien, Chris Ivimey, Dr. Ted Thuening, Matthew Uhlman, Dr. Ben Coughlin, Dr. Dipna Patel, Dr. Alex Achilling, Dr. Ryan Hannagan, Dr. Laura Cramer, Dr. Tedros Balema, Volkan Çinar, Yicheng Wang, Audrey Dannar, Cole Easton, Helen Chen, Avery Daniels, and Elizabeth Happel for always making the lab an enjoyable place to be in. I would like to especially a few people from above. Ryan for not only being an amazing sounding board for scientific and political ideas to bounce off of, but for a great friend during my time here, see you in 2024. Laura for always being there to help solve problems, whether they are experiment based problems, or making me not the only one to get stuck in things. I would like to thank George and Dipna, especially for making my transition into IMASC easier and less stressful than it would have been without you. I have appreciated learning a lot from both of you both scientifically, and also for being good friends. Thank you to Matt Macknowski and Andy for training me when I first joined the lab. Thank you to Matt and Alex for being good friends and especially for making my adjustment to a new city a lot more enjoyable. Thanks Yicheng and Volkan for making my life inside and outside of lab enjoyable and the discussions on the supremacy of different empires.

Thank you to people in the department outside of the Sykes Lab. Firstly, Thank you to the Utz lab for always being there to bounce UHV ideas off of and oftentimes having random parts in times of dire need. Thank you Dan Tinney, Laurin Joseph, and Dr. Eric High for always being there when we needed some help. Thank you also to many other people in our year that made my time here a good one, Dr. William Mullin, Dr. Kirsten Deprey, Dr. Subbarao Yalamanchili, Colin Mizia, and Amanda Carey.

There are numerous people in the department that have helped me be able to do research. Thank you to Larry Aulenback for always being there to help us fix things and not judging us too hard when we ask elementary engineering questions. I would also like to thank Justin Cronin, Debbie

D’Andrea, Kirsten Hickey, Sarah Iacobucci, Mike Lanza, Karen O’Hagan, and Allison Ramirez for always helping us navigate the logistical hurdles of research.

Thank you to my friends who have helped me along the way stay sane and been a source of constant entertainment. Thank you Mark, Allison, Zach, and Sarah whom have always been willing to change your schedules to make time for me when I traveled back home to enjoy the outdoors of Minnesota, and giving me support to keep going through. Thank you to Zach and Lauren for being amazing friends in Boston and showing me what the amazing city of Boston has to offer and support in achieving my goals.

Thank you especially to my family whom has kept me grounded and given me constant support throughout my Ph.D. I have greatly appreciated all the times you have visited me and given me amazing breaks during my time here, I could have never done it without you. To mom, dad, Katie, and Dan, you have always inspired me and pushed me to achieve my goals, and I am forever grateful for your constant support. Thank you again to everyone who has made this journey possible and enjoyable.

-Paul Kress

Table of Contents

Tables and Figures

Introduction

1.1 Heterogeneous Catalysis

The value of catalysts is around 20 billion dollars annually and the value of goods they produce is estimated to be about 15 trillion[1]. A catalyst is a substance that lowers the activation barrier for a process thereby allowing a chemical reaction to occur at lower temperatures and/or pressures[2,3]. The catalyst itself is not consumed during the reaction and can typically produce many orders of magnitude more product by mass than the mass of the catalytic material. Catalysts can also change the selectivity towards the products for a given reaction to make more desirable chemical commodities. Catalysis has always played an important role in many natural biological systems allowing many life forms to exist[4], but humanity has only taken advantage of the industrial possibilities of catalysis in the last 150 years[2]. Catalysis plays a crucial role in many parts of society, including but not limited to energy production[5], pharmaceuticals[6], the food industry[2], and the environmental sector[5,7–10]. Most of these catalytic processes are done with heterogeneous catalysts and it is estimated that 90% of all chemicals and materials have gone through a catalytic step at some point during the process[11].

Most catalytic processes use a heterogeneous catalyst wherein the catalyst and the reactants exist in different phases[11]. For most heterogenous processes the catalyst is in the solid phase while the reactants are in gas phase. The active form of most heterogeneous catalysts is often a metal nanoparticle that is placed on a high surface area support[12]. The nanoparticle itself is often made of expensive precious metals such as Pt, Pd, or Rh. Nanoparticles are not homogeneous and have many different types of sites available for reacting, so finding out the most energetically favorable and probably active site for

certain reactions can be difficult to deduce[3,13–16]. In addition to a variety of active sites available, nanoparticles also have the disadvantage of only having a fraction of the total atoms available for reaction. In heterogeneous catalysis, the gas phase reactants can only interact with the atoms on the surface of the nanoparticle, which makes the expensive precious metal inside the nanoparticle unavailable for reaction and thus reduces the mass efficiency relative to a homogeneous liquid phase catalyst. Despite these mass inefficiencies, heterogeneous catalysts are more commonly used in industrial reactions due to superior thermal stability and the ease of recovery of the catalyst after the reaction due to the catalyst and reactants being in different phases. In this thesis I take a surface science approach and identify key active sites for a variety of reactions along with studying the fundamental stability of these catalysts

1.2 Surface Science Approach

Surface science is a way of approaching catalysis by breaking downreactions and interactions into simple steps to better understand complex reaction pathways. It works through building a fundamental understanding of the underlying thermodynamic and kinetic processes behind complex catalysts at the atomic scale. The most famous example of this is the work of Gerhard Ertl who won the Nobel Prize in 2007 for understanding the role of step sites in the Haber-Bosch process[2]. This approach relies on generating conditions that are conducive for

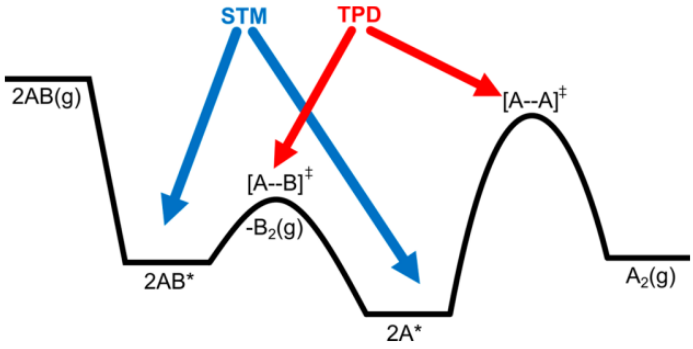

Figure 1.1: Model system approach whereby the STM visualizes initial and final states, while TPD gains information about the activation energy barriers for reaction. From reference[33]

surface sensitive studies to take place, namely ultra-high vacuum pressures (pressures below 1x 10^{-9} Torr) to ensure that the sample to be studied stays free of other adsorbates that could complicate the study. These conditions also allow for various different spectroscopy techniques that cannot normally be performed under atmospheric conditions. There are many facets to a nanoparticle, but in this thesis the (111) lattice is most often studied. This is due to the fact that the (111) lattice exposes atoms at the surface that are the most stable due to their increased metallic bonds compared to other lattices. The (111) lattice contains atoms at the surface that are coordinated to 9 atoms, whereas the bulk atoms are coordinated to 12. In the (111) lattice the surface atoms have 6 nearest neighbor pairs in the surface, and 3 bonding atoms underneath them. This thesis will mainly use scanning tunneling microscopy (STM) and temperature programmed desorption (TPD) to gain information about the catalytic properties of surfaces, and more specifically their structure-reactivity relationships. This combination of techniques is shown in Figure 1.1 for its ability to gain structural details about the catalytic surface and intermediates with STM, and information about the energetic barriers through TPD. This combined approach allows the effective study of many catalytic trends, and the discovery of new catalytic surfaces.

1.3 Trends in Heterogenous Catalysis

There are several overarching trends that guide the design of next generation catalysts. One important trend is the Sabatier principle, which states that the optimum catalyst for a given reaction has an intermediate binding strength to the molecules with which it interacts[17,18]. The catalyst needs to bind the molecule strongly enough to activate the bonds of interest, whilst not binding the final product so strongly that the molecule is

unable to leave the surface and blocks the active site for further catalytic reactions. This relationship between final binding strength and activation energy is more clearly explained through the Brønsted–Evans–Polanyi (BEP) relationship. These two important relationships are shown in Figure 1.2. The BEP relationship states that when a catalyst of interest has a lower activation barrier for a given reaction, the binding strength to the final product on the surface is stronger. This relationship refers to a single site on a surface for both the activation barrier and the final binding site of the molecular intermediate. This relationship exists because as one increases the binding strength of the intermediates to the surface, the formation of those intermediates becomes more favorable and thus the activation barrier is also lowered. The problem with relying on a linear relationship for catalytic materials, is that sometimes the Sabatier optimum does not intersect the BEP line[19,20]. In cases where the BEP line does not intersect the Sabatier optimum, it can be due to not being able to lower the activation barrier of a certain reaction low enough, or due to lowering the activation barriers so low that the intermediates are bound too strongly to the surface, thus causing the reaction to be kinetically inefficient. In cases like this it would be ideal to be able to deviate from these linear scaling relationships. These two principles in tandem with the d-band model for catalysis has allowed for the study and design of better catalytic materials[21,22].

D-band theory states that the electronic center of d-band electrons for a given metal is directly related to its catalytic activity and ability to activate and bind molecules. This electronic center of the d band is relative to the fermi level for each respective metal of interest. As one moves from left to right across the different transition metals the d

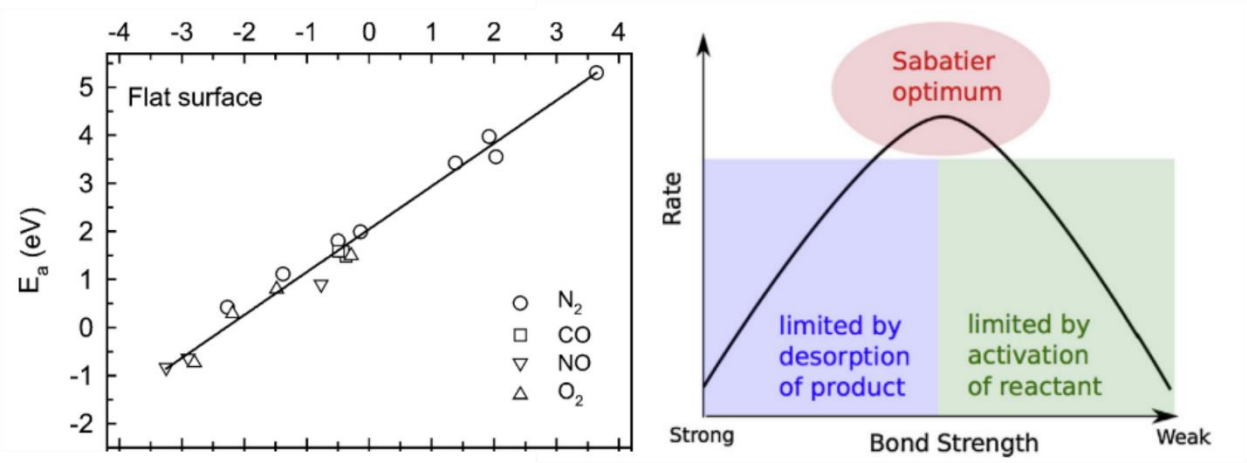

Figure 1.2: (a) Schematic of the BEP relationship adapted from above showing the relationship between activation of small molecules on various different surfaces relative to binding energy **(b)** Sabatier volcano relationship adopted from above whereby the optimum catalyst is a material that activates the desired bond, but does not overbind the intermediates to the surface. Taken from references[21,22].

orbitals become more filled and as a result, the d-band of the metals also becomes more filled. As the d-band becomes more filled this increases the distance from the fermi level to the center of the d band.. This results in a lower relative d band center, and when a molecular orbital is formed with the metal the resultant bond has more of the anti-bonding orbital filled, thus creating weaker binding[22,23]. In contrast, as one moves left in the periodic table, the d-band shiftsrelatively higher and when it interacts with a new molecular orbital a larger amount of the anti-bonding orbitals is left unfilled, thus creating stronger metal-adsorbate bonds. Using the Sabatier and BEP theories in conjunction with d-band values for many different metallic systems has aided in finding

possible catalysts that can exist on the optimum of the Sabatier curve, without having to empirically test all imaginable catalysts. This theory led approach is especially useful for surface scientists since experimental setups can be quite costly and time consuming, so being able to quickly identify and study the most promising catalysts is beneficial.

1.4 Bimetallic Alloys

Oftentimes the optimum catalyst for a given reaction is not purely one metal. Generally, properties of a metal can be altered through alloying with another metal. This generates alloys that can have different properties than either metal alone, which is due to two important effects, electronic and ensemble effects. Electronic effects come from the physical phenomenon that when one metal is alloyed with another there is a mixing of their D-bands and thus their electronic structure is a mixture of the two metals. Traditionally it is believed that mixing will create a linear combination of electronic structures, so alloys will not deviate off of BEP scaling due to electronic effects. Electronic effects can also be introduced via thin shell bimetallic alloys. The electronic donation and change in energy level effects on many types of reactions[24,25] The other major effect of alloying is the ensemble effect. Certain ensembles of bimetallic alloys are known to be active for certain reactions[7,26,27]. A famous example of this effect was shown by Goodman et al[28] whereby Pd dimers were the necessary ensemble to break C-C bonds in the synthesis of vinyl acetate, but isolated monomers could not break the C-C bond. Understanding the interplay of electronic and ensemble effects is key in understanding catalysts[17,29].

1.5 Single-Atom Alloys

In the last decade the Sykes lab has studied a particular type of alloys called

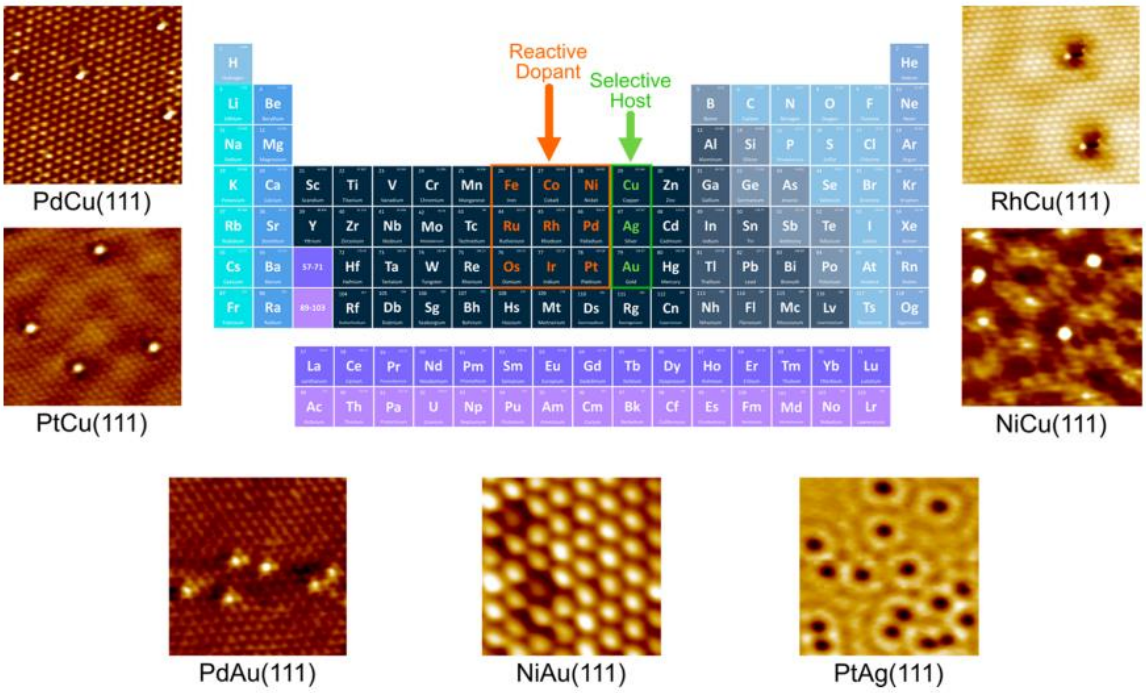

Figure 3: Periodic table showing the design principle behind SAAs of adding small amounts of reactive dopants to selective group 11 hosts. STM images of these alloys are shown around the table. From reference[33].

Single-Atom Alloys[30–33] (SAAs). These alloys are defined as having trace amounts of group 8, 9, and 10 transition metals doped into group 11 metals (Cu, Ag, Au)[33]. The term was first established by the work of Sykes and Flytzani-Stephanopoulos[32] which showed that isolated Pd atoms in Cu were capable of dissociating hydrogen and spilling over those atoms to the selective Cu host for hydrogenation reactions[32,34]. This new class of catalysts has a few advantages over traditional bi-metallic catalysts. Firstly, since the more reactive atom is isolated in a more selective host, these types of catalysts have shown tremendous coke resistance to reactions that involve the breakdown of hydrocarbons. This is mainly due to the ensemble effect of not having sites next to each other, which is a necessary condition for the hydrocarbon decomposition reaction[28,35]

which is known to be responsible for producing coke . In addition to their coke resistant nature, SAAs are also resistant to another common poison for platinum group metals (PGM), CO. This is due due to their much weaker binding of CO relative to their pure PGM counterparts[36]. Both of those are traditionally explained by a combination of ensemble and electronic effects, but recent results from Greiner et al[37] has shown the existence of a unique electronic state when one metal is isolated in another, suggesting that SAAs do not electronically mix the same way other bimetallic alloys do. This novel electronic structure has been predicted to exist by theory,[38,39] but seeing it through experimental means has proven that there is a unique electronic benefit to this class of alloys. These combined properties have allowed for single-atom alloys to deviate from linear scaling. Their deviation comes from observed phenomenon of having the transition state binding site be different from the final binding site[20], spillover of the intermediate molecule to the more weakly binding host[27,32,34,40], and the unique electronic nature that exists at the active site in many of these catalysts[37,41].

1.6 Stability of SAAs

There are two important factors that determine the stability of and ability to form single-atom alloys. The first is aggregation energy[36,42], which is the tendency for one

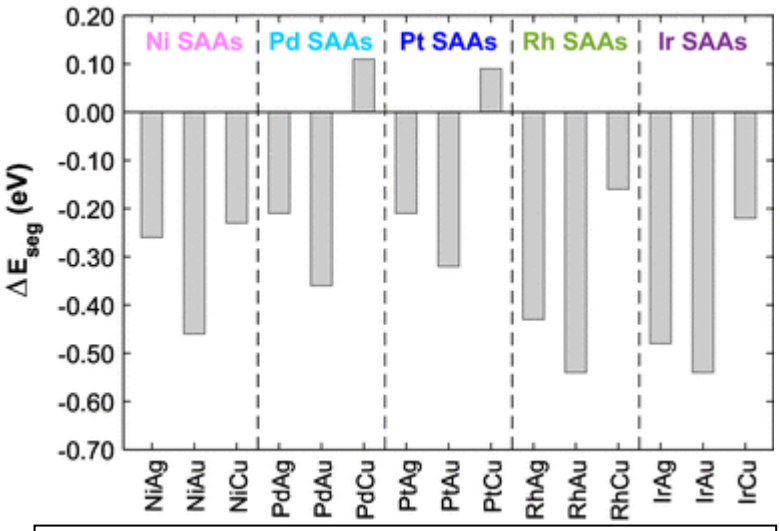

Figure 1.4: Segregation energies for various different dopant atoms to migrate into the bulk of a group 11 (111) host. Taken from reference[36]

metal to form a dopant-host bond or to form a dopant-dopant bond. The other consideration for the stability of a SAA is the segregation energy of the dopant in the host. This is the tendency of one metal to be preferentially at the surface over another. In most single-atom alloy systems the dopant atom prefers to be in the bulk as seen in Figure 1.4. However, it has been shown both experimentally and with theory that adsorbates such as CO and reactants such as ethanol can hold the dopant at the surface under thermal conditions where the dopant would prefer the bulk in many SAA systems[36,42–45].

1.7 Reactions of Interest

Industrially there are many reactions that play a vital role in transforming our society, and a variety of them were studied using fundamental surface science in this thesis. In studying these reactions, various different single crystal hosts were used: Cu(111), Ag(111), and Au(111). These hosts generally offer high selectivity towards desired products for many industrial reactions, but can have quite high activation barriers[35,46–50]. This lower activity is generally due to the lower D band centers of these metals compared to metals further left on the d block. To make these metals more active Pt, Pd, and Ni were doped into the group 11 surfaces, and their effect on reactivity was

examined. To first understand their reactivity, we must first know the active site and characterize it. In this thesis, much of the fundamental characterization of the alloys has been previously studied[40,51–53]. Further characterization of these alloys is documented in this thesis. Chapter 3 examines C-C coupling on NiAu SAAs in comparison to PdAu[54]. Chapter 4 looks at dehydrogenation/hydrogenation of ethyl groups on a PtCu SAA[55], working with theorists to elucidate the key steps of the reaction. Chapter 5 examines non-oxidative ethanol dehydrogenation on a NiAu SAA in collaboration with theory and nanoparticle work. Chapter 6 examines high pressure infrared studies that look at various single-atom alloys under elevated pressures of CO and examine the effect of elevated pressure on PdAu and NiAu SAAs. Chapter 7 examines non-oxidative ethanol dehydrogenation on a trimetallic PtCrAg alloy.

1.7.1 C-C coupling over NiAu SAA

C-C coupling is a key reaction for many fine chemical syntheses[28,56–61]. It is typically performed on homogeneous Pd catalysts, and recently there have been reports of the reaction happening on heterogeneous Pd catalysts[62]. We examined the reaction of methyl iodide with a NiAu SAA. We previously studied PdAu for this selective C-C coupling and found it was active for both parts of the reaction, C-I bond cleavage and C-C coupling[63]. On Au(111) under UHV conditions, the Au is inactive to breaking the C-I bond[64], but will couple the methyl groups if they are present on the surface. In this study the effect of Ni atoms in Au towards breaking the C-I bond are examined and the Ni site is active for this. To gain further insight into the system, computational theory is used to further understand the system. Similarities between homogeneous and heterogeneous catalysis are made with the aid of DFT and KMC.

1.7.2 Ethyl (De)hydrogenation over PtCu SAA

Dehydrogenation of small molecules is the first step in creating the building blocks for many fine chemicals[65]. Understanding reactions at the molecular scale will help aid in designing more efficient catalysts for reactions involving these key steps[66]. Beta hydride elimination is the most facile step on most catalytic surfaces, so studying this reaction in more detail is important in understanding the full catalytic cycle[67]. Traditionally this reaction takes place over platinum catalysts[68,69]. In this thesis, a PtCu SAA is used to examine the activity and selectivity towards this beta hydrogen and the selectivity is shown to be controllable by altering the amount of pre-adsorbed hydrogen.

1.7.3 Non-oxidative ethanol dehydrogenation

Ethanol dehydrogenation to acetaldehyde is important as acetaldehyde is one of the primary renewable biofuel feedstocks[70–72]. The first step of these transformative processes is the dehydrogenation of ethanol. Thus, studying the exact nature of the active sites that perform this dehydrogenation selectively is important. Two different materials were studied for this conversion, firstly NiAu SAA was examined for the conversion of ethanol to acetaldehyde under surface science conditions. Then PtCrAg was studied for converting ethanol into acetaldehyde. In PtCrAg the selective conversion of ethanol into acetaldehyde is shown and it requires both a unique active site of both Pt and Cr in an Ag host. The unique activity of the site and the reaction pathway is supported by DFT calculations. Unique activity is fundamentally due to the ability of Cr to stabilize an ethoxy intermediate, and Pt to stabilize the H surface intermediate. This uniqueness of active sites allows for the conversion of ethanol at very low loadings of combined reactive catalytic material in the Ag host, while still being selective. It was shown that

larger amounts of either pure Cr or pure Pt are unable to convert the ethanol into acetaldehyde. Through a combination of STM and TPD the sites were characterized. The STM image in Figure 1.5 shows that there is formation of mixed dimer sites on the surface, with both a larger scale image to show many mixed sites, and an enlarged image with greater detail to show the dimer sites more clearly.

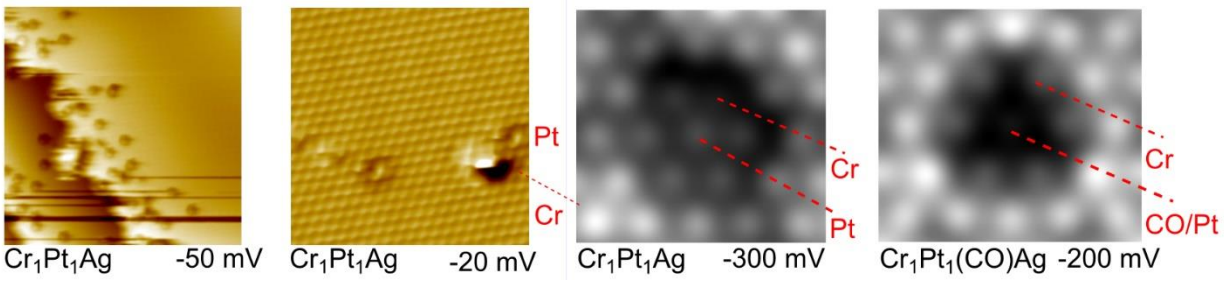

Figure 1.5: (a) STM image of PtCrAg at a step edge showing evidence of many close Cr and Pt sites in the Ag(111) surface **(b)** close up STM image of PtCr dimer site in Ag(111). **(c)** DFT simulated image of CrPt dimer site without CO **(d)** STM image of PtCr dimer site with CO atop on Pt, which more closely matches with

References

(1) C. Adams. Applied Catalysis: A Predictive Socioeconomic History. *Top. Catal.* **2009**, *52* (8), 924–934.

(2) G. Ertl. Reactions at Surfaces: From Atoms to Complexity (Nobel Lecture). *Angew. Chemie - Int. Ed.* **2008**, *47* (19), 3524–3535.

(3) G. A. Somorjai. Surface Science. *Science (80-.).* **1978**, *201* (4355), 489–498.

(4) T. J. Schwartz; B. J. O'Neill; B. H. Shanks; J. A. Dumesic. Bridging the Chemical and Biological Catalysis Gap: Challenges and Outlooks for Producing Sustainable Chemicals. *ACS Catal.* **2014**, *4* (6), 2060–2069.

(5) I. Fechete; Y. Wang; J. C. Védrine. The Past, Present and Future of Heterogeneous Catalysis. *Catal. Today* **2012**, *189* (1), 2–27.

(6) Z. Ma; F. Zaera. Organic Chemistry on Solid Surfaces. *Surf. Sci. Rep.* **2006**, *61* (5), 229–281.

(7) S. Schauermann; H. J. Freund. Model Approach in Heterogeneous Catalysis: Kinetics and Thermodynamics of Surface Reactions. *Acc. Chem. Res.* **2015**, *48* (10), 2775–2782.

(8) R. Ciriminna; E. Falletta; C. Della Pina; J. H. Teles; M. Pagliaro. Industrial Applications of Gold Catalysis. *Angew. Chemie - Int. Ed.* **2016**, *55* (46), 14210–14217.

(9) R. A. Sheldon; R. S. Downing. Heterogeneous Catalytic Transformations for Environmentally Friendly Production. *Appl. Catal. A Gen.* **1999**, *189* (2), 163–183.

(10) D. Rodríguez-Padrón; A. R. Puente-Santiago; A. M. Balu; M. J. Muñoz-Batista; R. Luque. Environmental Catalysis: Present and Future. *ChemCatChem* **2019**, *11* (1), 18–38.

(11) S. B. A. Hamid; R. Schlögl. The Impact of Nanoscience in Heterogeneous Catalysis. *Nano-Micro Interface Bridg. Micro Nano Worlds Second Ed.* **2015**, *2–2* (March), 405–430.

(12) R. J. Farrauto; L. Dorazio; C. H. Bartholomew. *Introduction to Catalysis and Industrial Catalytic Processes*; John Wiley {\&} Sons, 2016.

(13) X. Tian; X. Zhao; Y. Q. Su; L. Wang; H. Wang; D. Dang; B. Chi; H. Liu; E. J. M. Hensen; X. W. Lou; et al. Engineering Bunched Pt-Ni Alloy Nanocages for Efficient Oxygen Reduction in Practical Fuel Cells. *Science (80-.).* **2019**, *366*

(6467), 850–856.

(14) J. Osswald; K. Kovnir; M. Armbrüster; R. Giedigkeit; R. E. Jentoft; U. Wild; Y. Grin; R. Schlögl. Palladium-Gallium Intermetallic Compounds for the Selective Hydrogenation of Acetylene. Part II: Surface Characterization and Catalytic Performance. *J. Catal.* **2008**, *258* (1), 219–227.

(15) F. Besenbacher. Scanning Tunnelling Microscopy Studies of Metal Surfaces. *Reports Prog. Phys.* **1996**, *59* (12), 1737–1802.

(16) R. Imbihl; a Scheibe; Y. F. Zeng; S. Günther; R. Kraehnert; V. a Kondratenko; M. Baerns; W. K. Offermans; a P. J. Jansen; R. a van Santen. Catalytic Ammonia Oxidation on Platinum: Mechanism and Catalyst Restructuring at High and Low Pressure. *Phys. Chem. Chem. Phys.* **2007**, *9* (27), 3522–3540.

(17) A. J. Medford; A. Vojvodic; J. S. Hummelshøj; J. Voss; F. Abild-Pedersen; F. Studt; T. Bligaard; A. Nilsson; J. K. Nørskov. From the Sabatier Principle to a Predictive Theory of Transition-Metal Heterogeneous Catalysis. *J. Catal.* **2015**, *328*, 36–42.

(18) M. Che. Nobel Prize in Chemistry 1912 to Sabatier: Organic Chemistry or Catalysis? *Catal. Today* **2013**, *218–219* (April), 162–171.

(19) A. M. Larson; K. Groden; R. T. Hannagan; J. S. McEwen; E. C. H. Sykes. Understanding Enantioselective Interactions by Pulling Apart Molecular Rotor Complexes. *ACS Nano* **2019**, *13* (5), 5939–5946.

(20) A. R. Singh; J. H. Montoya; B. A. Rohr; C. Tsai; A. Vojvodic; J. K. Nørskov. Computational Design of Active Site Structures with Improved Transition-State Scaling for Ammonia Synthesis. *ACS Catal.* **2018**, *8* (5), 4017–4024.

(21) M. Andersen; A. J. Medford; J. K. Nørskov; K. Reuter. Scaling-Relation-Based Analysis of Bifunctional Catalysis: The Case for Homogeneous Bimetallic Alloys. *ACS Catal.* **2017**, *7* (6), 3960–3967.

(22) L. G. M. Pettersson; A. Nilsson. A Molecular Perspective on the D-Band Model: Synergy between Experiment and Theory. *Top. Catal.* **2014**, *57* (1–4), 2–13.

(23) B. Hammer; J. K. Nørskov. Electronic Factors Determining the Reactivity of Metal Surfaces. *Surf. Sci.* **1995**, *343* (3), 211–220.

(24) J. Zhang; M. B. Vukmirovic; Y. Xu; M. Mavrikakis; R. R. Adzic. Controlling the Catalytic Activity of Platinum-Monolayer Electrocatalysts for Oxygen Reduction with Different Substrates. *Angew. Chemie - Int. Ed.* **2005**, *44* (14), 2132–2135.

(25) J. Greeley; M. Mavrikakis. Alloy Catalysts Designed from First Principles. *Nat. Mater.* **2004**, *3* (11), 810–815.

(26) V. Ponec. Alloy Catalysts: The Concepts. *Appl. Catal. A Gen.* **2001**, *222* (1–2), 31–45.

(27) F. R. Lucci; M. D. Marcinkowski; T. J. Lawton; E. C. H. Sykes. H2 Activation and Spillover on Catalytically Relevant Pt-Cu Single Atom Alloys. *J. Phys. Chem. C* **2015**, *119* (43), 24351–24357.

(28) M. Chen; D. Kumar; C. W. Yi; D. W. Goodman. The Promotional Effect of Gold in Catalysis by Palladium-Gold. *Science (80-.).* **2005**, *310* (5746), 291–293.

(29) T. Bligaard; J. K. Nørskov; S. Dahl; J. Matthiesen; C. H. Christensen; J. Sehested. The Brønsted-Evans-Polanyi Relation and the Volcano Curve in Heterogeneous Catalysis. *J. Catal.* **2004**, *224* (1), 206–217.

(30) J. Liu; M. B. Uhlman; M. M. Montemore; A. Trimpalis; G. Giannakakis; J. Shan;

S. Cao; R. T. Hannagan; E. C. H. Sykes; M. Flytzani-Stephanopoulos. Integrated Catalysis-Surface Science-Theory Approach to Understand Selectivity in the Hydrogenation of 1-Hexyne to 1-Hexene on PdAu Single-Atom Alloy Catalysts. *ACS Catal.* **2019**, *9* (9), 8757–8765.

(31) G. Giannakakis; M. Flytzani-stephanopoulos; E. C. H. Sykes. Single-Atom Alloys as a Reductionist Approach to the Rational Design of Heterogeneous Catalysts. *Acc. Chem. Res.* **2018**, *52*, 237–247.

(32) G. Kyriakou; M. B. Boucher; A. D. Jewell; E. A. Lewis; T. J. Lawton; A. E. Baber; H. L. Tierney; M. Flytzani-Stephanopoulos; E. C. H. Sykes. Isolated Metal Atom Geometries as a Strategy for Selective Heterogeneous Hydrogenations. *Science (80-.).* **2012**, *335* (6073), 1209–1212.

(33) R. T. Hannagan; G. Giannakakis; M. Flytzani-Stephanopoulos; E. C. H. Sykes. Single-Atom Alloy Catalysis. *Chem. Rev.* **2020**, *120*, 12044–12088.

(34) F. R. Lucci; J. Liu; M. D. Marcinkowski; M. Yang; L. F. Allard; M. Flytzani-Stephanopoulos; E. C. H. Sykes. Selective Hydrogenation of 1,3-Butadiene on Platinum–Copper Alloys at the Single-Atom Limit. *Nat. Commun.* **2015**, *6*, 8550.

(35) M. D. Marcinkowski; M. T. Darby; J. Liu; J. M. Wimble; F. R. Lucci; S. Lee; A. Michaelides; M. Flytzani-Stephanopoulos; M. Stamatakis; E. C. H. Sykes. Pt/Cu Single-Atom Alloys as Coke-Resistant Catalysts for Efficient C–H Activation. *Nat. Chem.* **2018**, No. January.

(36) M. T. Darby; E. C. H. Sykes; A. Michaelides; M. Stamatakis. Carbon Monoxide Poisoning Resistance and Structural Stability of Single Atom Alloys. *Top. Catal.* **2018**, *61* (5–6), 428–438.

(37) M. T. Greiner; T. E. Jones; S. Beeg; L. Zwiener; M. Scherzer; F. Girgsdies; S. Piccinin; M. Armbrüster; A. Knop-Gericke; R. Schlögl. Free-Atom-like d States in Single-Atom Alloy Catalysts. *Nat. Chem.* **2018**, *10* (10), 1008–1015.

(38) A. Dasgupta; Y. Gao; S. R. Broderick; E. B. Pitman; K. Rajan. Machine Learning Aided Identification of Single Atom Alloy Catalysts. *J. Phys. Chem. C* **2020**, *124* (26), 14158–14166.

(39) H. Thirumalai; J. R. Kitchin. Investigating the Reactivity of Single Atom Alloys Using Density Functional Theory. *Top. Catal.* **2018**, *61* (5–6), 462–474.

(40) F. R. Lucci; M. T. Darby; M. F. G. Mattera; C. J. Ivimey; A. J. Therrien; A. Michaelides; M. Stamatakis; E. C. H. Sykes. Controlling Hydrogen Activation, Spillover, and Desorption with Pd-Au Single-Atom Alloys. *J. Phys. Chem. Lett.* **2016**, *7* (3), 480–485.

(41) H. Thirumalai; J. R. Kitchin. Investigating the Reactivity of Single Atom Alloys Using Density Functional Theory. *Top. Catal.* **2018**, *0* (0), 0.

(42) K. G. Papanikolaou; M. T. Darby; M. Stamatakis. CO-Induced Aggregation and Segregation of Highly Dilute Alloys: A Density Functional Theory Study. *J. Phys. Chem. C* **2019**, *123* (14), 9128–9138.

(43) G. Giannakakis; A. Trimpalis; J. Shan; Z. Qi; S. Cao; J. Liu; J. Ye; J. Biener; M. Flytzani-Stephanopoulos. NiAu Single Atom Alloys for the Non-Oxidative Dehydrogenation of Ethanol to Acetaldehyde and Hydrogen. *Top. Catal.* **2017**, *77030* (0), 1–23.

(44) F. Tao; M. E. Grass; Y. Zhang; D. R. Butcher; J. R. Renzas; Z. Liu; J. Y. Chung; B. S. Mun; M. Salmeron; G. A. Somorjai. Reaction-Driven Restructuring of Rh-Pd

and Pt-Pd Core-Shell Nanoparticles. *Science (80-.).* **2008**, *322* (November), 932–935.

(45) F. Gao; Y. Wang; D. W. Goodman. CO Oxidation over AuPd(100) from Ultrahigh Vacuum to near-Atmospheric Pressures: CO Adsorption-Induced Surface Segregation and Reaction Kinetics. *J. Phys. Chem. C* **2009**, *113* (33), 14993–15000.

(46) F. Zaera. Hydrocarbon Conversion on Metal Surfaces. *Acc. Chem. Res.* **2009**, *42* (8), 1152.

(47) C. J. Jenks; B. E. Bent; N. Bernstein; F. Zaera. The Chemistry of Alkyl Iodides on Copper Surfaces. 1. Adsorption Geometry. *J. Phys. Chem. B* **2000**, *104* (14), 3008–3016.

(48) Z. Ma; F. Zaera. Organic Chemistry on Solid Surfaces. *Surf. Sci. Rep.* **2006**, *61* (5), 229–281.

(49) B. Paul, Anumita; Bent. Alkyl Coupling on Copper, Silver, and Gold: Correlation between the Coupling Rate and the Metal-Alkyl Bond Strength. *J. Catal.* **1994**, 264–271.

(50) M. D. Marcinkowski; J. Liu; C. J. Murphy; M. L. Liriano; N. A. Wasio; F. R. Lucci; M. Flytzani-Stephanopoulos; E. C. H. Sykes. Selective Formic Acid Dehydrogenation on Pt-Cu Single-Atom Alloys. *ACS Catal.* **2017**, *7* (1), 413–420.

(51) F. R. Lucci; T. J. Lawton; A. Pronschinske; E. C. H. Sykes. Atomic Scale Surface Structure of Pt/Cu(111) Surface Alloys. *J. Phys. Chem. C* **2014**, *118* (6), 3015–3022.

(52) D. A. Patel; P. L. Kress; L. A. Cramer; A. M. Larson; E. C. H. Sykes. Elucidating

the Composition of PtAg Surface Alloys with Atomic-Scale Imaging and Spectroscopy. *J. Chem. Phys.* **2019**, *151* (16).

(53) Z. T. Wang; M. T. Darby; A. J. Therrien; M. El-Soda; A. Michaelides; M. Stamatakis; E. C. H. Sykes. Preparation, Structure, and Surface Chemistry of Ni-Au Single Atom Alloys. *J. Phys. Chem. C* **2016**, *120* (25), 13574–13580.

(54) P. Kress; R. Réocreux; R. Hannagan; T. Thuening; J. A. Boscoboinik; M. Stamatakis; E. C. H. Sykes. Mechanistic Insights into Carbon-Carbon Coupling on NiAu and PdAu Single-Atom Alloys. *J. Chem. Phys.* **2021**, *154* (20).

(55) R. Réocreux; P. L. Kress; R. T. Hannagan; V. Çınar; M. Stamatakis; E. C. H. Sykes. Controlling Hydrocarbon (De)Hydrogenation Pathways with Bifunctional PtCu Single-Atom Alloys. *J. Phys. Chem. Lett.* **2020**, *11* (20), 8751–8757.

(56) E. A. Lewis; M. D. Marcinkowski; C. J. Murphy; M. L. Liriano; A. J. Therrien; A. Pronschinske; E. C. H. Sykes. Controlling Selectivity in the Ullmann Reaction on Cu(111). *Chem. Commun.* **2017**, *53* (55), 7816–7819.

(57) M. D. Marcinkowski; J. J. Liu; C. J. Murphy; M. L. Liriano; N. A. Wasio; F. R. Lucci; M. Flytzani-Stephanopoulos; E. C. H. Sykes; W. Paw?owski; A. Zalewska; et al. Unusual Hydrogen Effect in Olefin Dehydrogenation: 1-Methylcyclohexene Dehydrogenation Initiated by Excess Hydrogen over Pt(111) Surfaces, a Combined Sum Frequency Generation Spectroscopy and Kinetic Study. *J. Catal.* **2009**, *24* (1), 125–140.

(58) L. Yin; J. Liebscher. Carbon-Carbon Coupling Reactions Catalyzed by Heterogeneous Palladium Catalysts. *Chem. Rev.* **2007**, *107* (1), 133–173.

(59) N. T. S. Phan; M. Van Der Sluys; C. W. Jones. On the Nature of the Active

Species in Palladium Catalyzed Mizoroki-Heck and Suzuki-Miyaura Couplings - Homogeneous or Heterogeneous Catalysis, a Critical Review. *Adv. Synth. Catal.* **2006**, *348* (6), 609–679.

(60) F. Monnier; M. Taillefer. Catalytic C-C, C-N, and C-O Ullmann-Type Coupling Reactions. *Angew. Chemie - Int. Ed.* **2009**, *48* (38), 6954–6971.

(61) T. Borkowski; A. M. Trzeciak; W. Bukowski; A. Bukowska; W. Tylus; L. Kepiński. Palladium(0) Nanoparticles Formed in Situ in the Suzuki-Miyaura Reaction: The Effect of a Palladium(II) Precursor. *Appl. Catal. A Gen.* **2010**, *378* (1), 83–89.

(62) Z. Chen; E. Vorobyeva; S. Mitchell; E. Fako; M. A. Ortuño; N. López; S. M. Collins; P. A. Midgley; S. Richard; G. Vilé; et al. A Heterogeneous Single-Atom Palladium Catalyst Surpassing Homogeneous Systems for Suzuki Coupling. *Nat. Nanotechnol.* **2018**, *13* (August), 1–6.

(63) R. Réocreux; M. Uhlman; T. Thuening; P. Kress; R. Hannagan; M. Stamatakis; E. C. H. Sykes. Efficient and Selective Carbon-Carbon Coupling on Coke-Resistant PdAu Single-Atom Alloys. *Chem. Commun.* **2019**, *55* (100), 15085–15088.

(64) A. Paul; X. Michael; B. E. Bent. Disproportionation and Coupling Reactions of Alkyl Iodides on a Au(111) Surface. **1993**.

(65) S. Chen; X. Chang; G. Sun; T. Zhang; Y. Xu; Y. Wang; C. Pei; J. Gong. Propane Dehydrogenation: Catalyst Development, New Chemistry, and Emerging Technologies. *Chem. Soc. Rev.* **2021**.

(66) Z. Zhao; J. Jiang; F. Wang. An Economic Analysis of Twenty Light Olefin Production Pathways. *J. Energy Chem.* **2021**, *56*, 193–202.

(67) D. Sung; A. J. Gellman. Ethyl Iodide Decomposition on Cu(1 1 1) and Cu(2 2 1). *Surf. Sci.* **2004**, *551* (1–2), 59–68.

(68) F. Zaera; D. Chrysostomou. Propylene on Pt(111) II. Hydrogenation, Dehydrogenation, and H-D Exchange. *Surf. Sci.* **2000**, *457* (1), 89–108.

(69) O. A. Bariås; A. Holmen; E. A. Blekkan. Propane Dehydrogenation over Supported Pt and Pt-Sn Catalysts: Catalyst Preparation, Characterization, and Activity Measurements. *J. Catal.* **1996**, *158* (1), 1–12.

(70) J. Sun; Y. Wang. Recent Advances in Catalytic Conversion of Ethanol to Chemicals. *ACS Catal.* **2014**, *4* (4), 1078–1090.

(71) C. Angelici; B. M. Weckhuysen; P. C. A. Bruijnincx. Chemocatalytic Conversion of Ethanol into Butadiene and Other Bulk Chemicals. *ChemSusChem* **2013**, *6* (9), 1595–1614.

(72) T. Takei; N. Iguchi; M. Haruta. Synthesis of Acetoaldehyde, Acetic Acid, and Others by the Dehydrogenation and Oxidation of Ethanol. *Catal. Surv. from Asia* **2011**, *15* (2), 80–88.

Chapter 2: Experimental

2.1. Introduction

The two main techniques that are used in this thesis are scanning tunnelling microscopy (STM) and temperature programmed desorption (TPD). These two techniques in tandem allow for a powerful understanding of the catalytic landscape. Whereby the STM allows for an atomic level understanding of the catalytic surface and then TPD can allow for a better understanding of the energetics of the reaction pathway. Through this relationship structure-activity relationships can be determined and the key active sites that transform one chemical into another can be related. Other techniques explored in this thesis include X-Ray Photoelectron Spectroscopy, Reflection Absorption Infrared Spectroscopy.

The techniques used in this thesis are all primarily surface science techniques. These require ultra-high vacuum (UHV) to operate and are capable of producing an atomistic understanding of what the surface of interest looks like. The use of UHV is advantageous for many reasons, it allows for the surfaces to remain clean of impurities so to ensure that studies conducted on these surfaces are of the desired species of interest. Ultra-High Vacuum consists of pressures below 1.0×10^{-9} mbar. This allows for the careful study of the interaction of molecules and atoms with carefully prepared surfaces. The surfaces primarily studied in this thesis are single-crystal (111) type surfaces whereby a single crystal is cut to expose a specific facet, and the (111) facet for fcc crystals in the lowest energy facet whereby the atoms in the surface layer are the most coordinated, minimizing their surface free energy[1]. These crystals are also able to be cleaned to atomic level cleanliness allowing for such techniques such as scanning

tunnelling microscopy to correctly identify the geometric arrangement of the atoms and molecules on the surface. For TPD this low pressure ensures that the molecules adsorbed to the surface are the only molecules of interest being studied.

To maintain such a high degree of cleanliness, proper cleaning of the crystals between experiments must be conducted. Cleaning our crystals is a process of Ar^+ bombardment at energies between 1-1.5 keV, afterwards annealing the crystals short of their melting point at 700 K in the TPD chambers and 750 K in the STM chambers, is done to make the surface flat and remove unstable defects in the crystal.

2.2 Scanning Tunneling Microscopy

Scanning Tunneling Microscopy works by bringing an atomically sharp and conductive tip, brought within angstroms of a conductive surface[2–4]. The tip and surface are biased and according to classical mechanics, there should be no current flow between the tip and surface, but due to quantum tunneling, a small percentage of electrons will tunnel from tip to surface, or vice-versa depending on the bias. This flow of electrons is highly dependent on the tip-surface distance, which allows for an electronic topographical map to be made of the surface. The relationship between tip sample distance is as follows

$$I \propto \exp(-2kz) \quad \textbf{(2.1)}$$

Where k is defined by

$$k = \sqrt{\frac{2m}{h^2}}(eV_b - E) \quad \textbf{(2.2)}$$

In equation 2.3, m is the mass of an electron, E is the energy of the tunneling electron, h is the reduced Planck's constant, and eV is the barrier height of the tunneling gap. The STM can operate in two main modes, constant height mode and constant current mode.

Constant current mode is the more commonly used mode and involves a feedback loop that constantly adjusts the height of the STM tip to keep the current the same, generating an electronic z topography map of the surface.

2.3 TPD

Temperature Programmed Desorption(TPD) is a surface science technique that is performed under UHV conditions that obtains important kinetic parameters about desorption and reaction events on the surface[5]. All experiments were performed on well prepared single crystals cooled to cryogenic temperatures and exposed to gas molecules of interest. A quadruple mass spectrometer (QMS) is brought to close and reproducible proximity to the surface of the sample. A linear heating rate is applied to the sample, which breaks the surface adsorbate bonds, whereby the molecules are observed by the QMS, producing a graph of QMS intensities vs. sample temperature.

The desorption rate is directly related to the rise in pressure in the chamber due to adsorbates leaving the surface[6]. The desorption events can be described by the Arrhenius equation.

$$k_D = Ae^{(-\frac{E_d}{RT})} \quad \textbf{(2.3)}$$

where K_D s the desorption rate constant, A is the pre-exponential factor, E_d is the desorption barrier, R is the ideal gas constant, and T is temperature[7]. The desorption rate for molecules from a surface is described by the Polanyi-Wigner equation

$$-\frac{d\theta}{dT} = \frac{k_d}{\beta}\theta^m \quad \textbf{(2.4)}$$

Where θ is surface coverage of adsorbate of interest, β is heating rate, and m is the order of the reaction[8]. The shape of the TPD peak can be used to determine the reaction order since the desorption rate and order of reaction are related by equation 2.4

TPD experiments can be quantified by measuring the area under the signal and applying appropriate corrections relating to their cracking pattern, the specific quadrupole mass spectrometry (QMS) sensitivity, and an ionization cross section correction[9]. Once these corrections are applied to a specific m/z for a molecule, the corrected areas can be directly compared across different TPD experiments. The cracking pattern is related to the probability of the molecule of interest fragmenting into the m/z tracked and this probability can be found by using the NIST database. The specific QMS sensitivity is a correction applied to the QMS specifically, since they are more sensitive to lighter masses due to the way the quadruples function, and all of the QMS on the TPD chambers have been calibrated using inert gases. The ionization cross section is the probability of the molecule being ionized and the source for the information on the ionization cross section can again be found on NIST. For molecules that are larger than those found on the NIST database, combining smaller fragments can be done to obtain the larger molecules ionization probability. Through doing this TPD can quantify the amount of a specific molecule of interest desorbing for the surface, but to be able to make direct statements about the cause of the differences in desorption related to surface structure, other techniques are used. All of the TPDs presented in this thesis have been corrected using these correction factors. To relate the differences observed in TPD to surface structure, complimentary techniques such as XPS, STM, and RAIRs were used to learn about the alloys configurations on the surface of interest.

2.4 Reflection Absorption Infrared Spectroscopy (RAIRS)

Infrared spectroscopy (IR) can be used to measure characteristic vibrational modes of molecules. RAIRS is a specific type of IR whereby the IR light is reflected off the surface at a grazing incident before being collected by the detector. This light interacts with molecules on the surface and their vibrations can be detected following a series of selection rules. Linear molecules have 3N-5 degrees of vibrational modes and nonlinear molecules have 3N-6 degrees of vibrational modes[10]. In order for a vibrational mode to be IR active for RAIRS a net change in the dipole moment must occur perpendicular to the surface. This is due to the fact that surface generates an image dipole which mirrors the dipole of the molecule. This dipole causes a net cancellation of vibrations parallel to the surface, and amplifies vibrations perpendicular to the surface. An IR spectrometer broadband source emitting in the mid-IR (4000-400 cm^{-1}) was used in all experiments in this thesis.

In this thesis specifically the vibrations of CO will be examined to gain information about the sites available for binding on the surface. CO is known to vibrate at different wavenumbers depending on its binding orientation on the surface[11–14]. With dilute surface alloys, the binding sites available to CO can tell us information about the arrangement of the metal atoms on the surface. CO vibrotational modes are dependent on the site it is bound to, leading to different ranges for CO bound atop(~2000-2150 cm^{-1}), bridge(~1850-1950 cm^{-1}), and three fold(~1750-1850 cm^{-1})[14,15].

2.5 Ultrahigh Vacuum (UHV) Chambers

All the work presented in this thesis was performed in UHV chambers with various different analytical techniques accessible.

2.5.1 LT STM

All STM was collected on an Omnicron low-temperature STM. The STM has two chambers, a preparation chamber and an analysis chamber that are separated by a gate valve (VAT). The pressures are maintained in the preparation chamber by an ion pump (Varian), turbomolecular pump (Pfeiffer), and titanium sublimation pumps (Vacgen). The analysis chamber is equipped with titanium sublimation pumps and an ion pump to maintain pressures. The preparation chamber is equipped with both a hot filament style sputter gun (RBD instruments) and a cold cathode style (Omnicron Nanotechnology). The sample manipulator (Vacgen) allows the samples to be heated up to 1000 K, moved in x (20 mm), y (20 mm), z (600 mm), as well as rotated 180 degrees. Surface cleanliness was checked with the STM and the samples were clean when they had under 1 defect per 50 x 50 nm^2. The preparation chamber was also equipped with metal deposition sources (EFM3 Omnicron nanotechnology) and also has a load lock separated from the main chamber via a VAT valve for loading samples. The single crystals were mounted on Ta plates using Ta sheets to physically hold them on the sample plates.

The analysis chamber is capable of scanning under several different temperatures. It is equipped with two cryogenic dewars which are thermally connected to the scanning stage. The outer dewar is filled with Liquid N_2 (80 K) and the inner dewar can be filled with either LN_2 or Liquid Helium (5 K) depending on the desired scanning temperature. Annealing the samples can be performed by holding the sample in the wobblestick transfer arm for various different times to reach desired temperatures. Once the sample is

ready to be imaged it is loaded into the STM stage, the entire chamber is isolated from the ground through the use of high pressure air legs which lift the chamber off of the ground. Low noise (< 5 pm peak-to-peak) and atomically resolved images can be obtained from this system.

2.5.2 Temperature Programmed Desorption (TPD) Chambers

All TPD experiments were performed in two different TPD chambers, both holding a single crystal that was resistively heated by running wires through holes in the crystal. Current was supplied and a K-Type thermocouple was welded to the back of the crystal to monitor temperature. A feedback loop using a PID controller was used to maintain constant heating of the crystal throughout all experiments and all TPDs were collected with a heating rate between 1-2 Ks^{-1}. All TPD chambers in this thesis have an operating pressure below 2 x 10^{-10} mbar maintained by a turbomolecular pump (Pfeiffer) and titanium sublimation pumps (Vacgen). The sample is supported in the chamber and thermally connected to a dewar to allow for cooling of the sample with liquid nitrogen to reach cyrogenic temperatures (80 K). Dosing of gasses was performed using high precision leak valves and units of langmuirs were used (~ 1 x 10^{-6} mbar s^{-1}). The sample could be rotated 360 degrees using a rotatable, and -10 mm in both x and y. In z the crystal could be moved 50 mm. The quadrupole mass spectrometer (QMS) (Hiden HAL/3F 301), was mounted on a linear z drive and had a mass range of 0-300 amu. The filament for all spectra was done at an ionization energy of 70 eV (done to match the ionization current of the ion gauges for calibration purposes). The QMS has two different modes of detection, a faraday cup and a secondary electron multiplier (SEM). The SEM allows for the amplication of the desired m/z, but to maintain the lifetime of the SEM it

was not operated at pressures above 1 x 10^{-7} mbar. The TPD chambers are equipped with RBD hot filament and Omnicron nanotechnology cold cathode sputter guns for sample cleaning. Sample deposition was performed on TPD chambers using EFM3 e-beam evaporator sources, with the sample held at the required temperature for the alloy formation.

2.6 Preparation of Bimetallic Alloys

Bimetallic alloys were prepared the same way in all chambers studied in this thesis. Single crystals were cleaned by repeated sputter (1.5 KeV Ar^+, 10 μA or 2 μA) anneal (700-800 K) cycles. Pt (99.95% Goodfellow), Pd (99.95% Goodfellow), and Ni (99.99% Goodfellow) rods of 50 mm in length and 2 mm diameter were used as the evaporation source to prepare the bimetallic surfaces. Deposition took place using flux monitored e-beam evaporation sources, typically 10 nA fluxes, and the concentration was varied by changing the amount of time the single crystal was exposed to the evaporation source. Metal coverages in the TPD chambers was determined using CO titration. CO was dosed on the surface at 80 K, and the areas under the respective curves for CO binding to Pt and Cu were compared. On Cu(111) samples the coverage of the dopant metal can be determined using the following method because CO bind atop on single atoms of Pt in Cu[16].

$$\theta_{Pt} = \frac{A_{Pt}}{A_{Pt}+(A_{Cu}/0.52)} \quad \textbf{(2.5)}$$

For metals in Au, or Ag, two methods were deployed. A CO titration method using a monolayer of the deposited metal as the maximum surface coverage, and also a combination CO and ethanol titration method. For the ethanol monolayer method, an uptake was performed of ethanol on the single crystal, and since the packing density of

ethanol on Au is known[17]. The area of a specific CO peak was then corrected and ratioed to the area of the monolayer of corrected ethanol to determine a surface coverage of the respective dopant.

References

(1) V. A. Kondratenko; M. Baerns. Mechanistic Insights into the Formation of N2O and N2 in NO Reduction by NH3 over a Polycrystalline Platinum Catalyst. *Appl. Catal. B Environ.* **2007**, *70* (1–4), 111–118.

(2) Kurt W. Kolasinski. *Surface Science: Foundations of Catalysis and Nanoscience*, 3rd ed.; John Wiley {\&} Sons, 2012.

(3) G. Binnig; H. Rohrer. Scanning Tunneling Microscopy. *IBM J. Res. Dev.* **1986**, *30* (4), 355–369.

(4) G. Binnig; H. Rohrer; C. Gerber; E. Weibel. Tunneling through a Controllable Vacuum Gap. *Appl. Phys. Lett.* **1982**, *40* (2), 178–180.

(5) M. Bowker; R. J. Madix. XPS, UPS and Thermal Desorption Studies of Alcohol Adsorption on Cu(110). I. Methanol. *Surf. Sci.* **1980**, *95* (1), 190–206.

(6) D. A. King. Thermal Desorption from Metal Surfaces: A Review. *Surf. Sci.* **1975**, *47* (1), 384–402.

(7) J. Laidler, K. *Chemical Kinetics*, 3rd ed.; Prentice Hall, 1987.

(8) P. A. Redhead. Thermal Desorption of Gases. *Vacuum* **1962**, *12* (4), 203–211.

(9) M. A. Van Spronsen; K. Daunmu; C. R. O'Connor; T. Egle; H. Kersell; J. Oliver-Meseguer; M. B. Salmeron; R. J. Madix; P. Sautet; C. M. Friend. Dynamics of Surface Alloys: Rearrangement of Pd/Ag(111) Induced by CO and O2. *J. Phys. Chem. C* **2019**, *123* (13), 8312–8323.

(10) P. Larkin. *Infrared and Raman Spectroscopy: Principles and Spectral Interpretation*; Elsevier, 2017.

(11) W. X. Huang; J. M. White. Propene Adsorption on Ag(1 1 1): A TPD and RAIRS Study. *Surf. Sci.* **2002**, *513* (2), 399–404.

(12) D. A. Patel; R. T. Hannagan; P. L. Kress; A. C. Schilling; V. Çlnar; E. C. H. Sykes. Atomic-Scale Surface Structure and CO Tolerance of NiCu Single-Atom Alloys. *J. Phys. Chem. C* **2019**, *123* (46), 28142–28147.

(13) A. S. Hoffman; C. Y. Fang; B. C. Gates. Homogeneity of Surface Sites in Supported Single-Site Metal Catalysts: Assessment with Band Widths of Metal Carbonyl Infrared Spectra. *J. Phys. Chem. Lett.* **2016**, *7* (19), 3854–3860.

(14) F. Gao; Y. Wang; D. W. Goodman. CO Oxidation over AuPd(100) from Ultrahigh Vacuum to near-Atmospheric Pressures: CO Adsorption-Induced Surface Segregation and Reaction Kinetics. *J. Phys. Chem. C* **2009**, *113* (33), 14993–15000.

(15) C. C. Leon; Q. Liu; S. T. Ceyer. CO Adsorption on Gold Nickel Au-Ni(111) Surface Alloys. *J. Phys. Chem. C* **2019**, *123* (14), 9041–9058.

(16) F. R. Lucci; M. D. Marcinkowski; T. J. Lawton; E. C. H. Sykes. H2 Activation and Spillover on Catalytically Relevant Pt-Cu Single Atom Alloys. *J. Phys. Chem. C* **2015**, *119* (43), 24351–24357.

(17) A. E. Baber; T. J. Lawton; E. C. H. Sykes. Hydrogen-Bonded Networks in Surface-Bound Methanol. **2011**, 9157–9163.

Chapter 3: Mechanistic Insights in Carbon-carbon Coupling on NiAu and PdAu Single-Atom Alloys

This chapter was modified from an original paper published in 2021 by the same title, PL Kress et al. from the Journal of Chemical Physics Volume 154, Issue 20. DFT calculations were performed by Romain Réocreux and Michail Stamatakis from UCL. Theodore Thuening performed the Ni calibration, and Anibal Boscoinik assisted with the RAIRS

3.1 Introduction

Carbon-carbon coupling is an important step in the upgrading of light alkanes which are becoming more abundant due to higher shale gas production rates.[1] Performing selective sp^3-sp^3 carbon coupling is still very challenging despite its importance to many processes, for example in the production of pharmaceuticals.[2,3] Typically, sp^3-sp^3 (Würtz) carbon coupling reactions are carried out using homogeneous catalysts; however, a number of issues plague homogeneous catalysis, such as difficulties in product-catalyst separation and catalyst deactivation over time. Therefore, there is interest in employing heterogeneous catalytic methods instead. Typically, Pd complexes are used as homogeneous catalysts and recently, a heterogeneous Pd-atom based catalyst with superior performance to homogeneous systems has been reported for Suzuki Coupling.[4] Specific to this work, PdAu single-atom alloys (SAAs) investigated using a model single crystal approach, have been shown to perform selective sp^3-sp^3 carbon-carbon coupling when methyl iodide is used as the reactant.[5] While Pd is a commonly used metal for coupling reactions, Ni is an attractive alternative of interest, in part, due to its lower cost.

In this work, model NiAu surfaces were studied with a range of surface science techniques to understand their structure and reactivity towards methyl iodine, while also making comparisons to previously investigated PdAu systems for the same reaction. NiAu and PdAu single-atom alloys were then modelled theoretically in order to understand the mechanism of sp^3-sp^3 carbon-carbon coupling on the two systems and the effect of the iodine in terms of its competition with methyl groups for the active sites. This synergistic approach, combining surface science and modelling techniques, has already been proven successful in elucidating structure-function relationships and delivering an atomic-scale understanding of coupling reaction mechanisms.[6–11] Specifically, we combined Temperature Programmed Desorption (TPD), Reflection Absorption Infrared Spectroscopy (RAIRS), Scanning Tunneling Microscopy (STM), Density Functional Theory (DFT), and kinetic Monte Carlo (KMC) methods to first determine the model catalyst surface, then quantify the performance of the catalyst towards the coupling chemistry, and finally model these results with first-principles theory in order to get an atomic-scale picture of the reaction mechanism. Our results highlight the important role of iodine, which had previously been considered a bystander species, on the barrier for sp^3-sp^3 carbon coupling on PdAu SAA surfaces.

3.2 Methods

All experiments were performed in one of three ultra-high vacuum chambers with base pressures below 2×10^{-10} mbar. The Au(111) single crystals were cleaned by successive Ar^+ sputtering cycles (1.5 keV, 10 μA) followed by annealing to 725 K. Ni was deposited onto the Au(111) crystal held at 380 K using a Omicron Nanotechnology Focus EFM 3 electron beam evaporator and the Ni coverage was determined by XPS or CO TPD titration which has been previously reported.[12] Liquid methyl iodide (Sigma Aldrich 99.5%) was purified by freeze-pump-thaw cycles and was then dosed through a high-precision leak valve onto the crystal. TPD experiments were then performed in the UHV chamber using a Hiden quadruple mass spectrometer and a heating rate of 2 K s^{-1}. STM studies were performed using a low-temperature scanning tunneling microscope (Omicron Nanotechnology) at 5 K. Reflection absorption infrared spectroscopy (RAIRS) experiments were performed at the Center for Functional Nanomaterials (CFN) at Brookhaven National Laboratory in a UHV system with a connected preparation chamber and X-ray photoelectron spectroscopy (XPS) chamber for measurement of the Ni content and cleanliness of sample. The XPS data was obtained at room temperature using a SPECS PHOIBOS NAP 150 hemispherical analyser and a monochromatic Al Kα X-ray source (1486.6 eV, ~0.25 eV linewidth) focused on the sample to a spot size <0.3 mm (0.05 eV step, 0.1 s dwell time, 5 scans, 50 eV pass energy). The infrared data was collected using a Bruker 80 V spectrometer with a polarizer and an MCT detector (2000 scans, 4 cm^{-1} resolution) in a UHV chamber with KBr windows and a beam to surface angle ~8°. The IR spectra were taken while the chamber was filled to $1x10^{-6}$ mbar CO.

The periodic Density Functional Theory (DFT) calculations were performed using the Vienna *Ab initio* Simulation package (VASP) 5.4.4.[13–15] We used the nonlocal optB86b-vdW functional to describe the exchange-correlation potential.[16–19] The core electrons were treated using the Projected Augmented Wave (PAW) method.[20,21] The electronic density associated with the valence electrons was expanded on a plane wave basis set with an energy cut-off of 400 eV.

Two sets of slabs and Monkhorst-Pack[22] k-point meshes were used:

- A 4-layer p(4×4) Au(111) slab and a 7×7×1 k-point mesh were used to describe the reactivity of gold sites.
- A 4-layer p(3×1) Au(211) slab, where one of the step-edge Au atoms was substituted with Ni or Pd, and a 11×9×1 k-point mesh were used to describe the reactivity of the dopant atom at the elbow of the herringbone reconstruction.

The slabs were built after optimizing the bulk structure of Au (lattice constant of 4.127 Å). Further optimizations of the surface structures were carried out after fixing the positions of the atoms of the first two layers at their bulk positions. Transition states were optimized using a combination of algorithms (CI-NEB,[23,24] DIMER[24–26] and Quasi-Newton). Vibrational frequency calculations were performed for all species.

For a given elementary step the activation energy Ea is defined as the difference between the energy of the transition state E_{TS} and the energy of the reactant(s) E_R, while the reaction energy $\Delta_r E$ is the difference between the energy of the product(s) E_P and that of the reactant(s) E_R:

$Ea = E_{TS} - E_R$

$\Delta_r E = E_P - E_R$

The Temperature Programmed Desorption (TPD) experiments were simulated within the graph-theoretical kinetic Monte Carlo (KMC) approach as implemented in *Zacros* 2.0.[27,28] The kinetic constants were estimated within the approximations of harmonic Transition State Theory using parameters obtained from the DFT calculations (energies, frequencies and rotational constants). The simulations were run on periodic lattices comprising sites of four different types: top Au sites, top Pd (or Ni) sites, threefold Au sites, threefold PdAu (or NiAu) mixed sites.

The lattices were built ensuring a 3% surface loading in Pd (or Ni) sites, randomly seeded as single atoms. Simulations on PdAu without iodine were run on a 15,300-site lattice (10,200 threefold sites and 5,100 top sites) as reported in our previous work on PdAu. All other simulations were performed on a 105,336-site lattice (35,112 top sites and 70,224 threefold sites) to ensure good sampling even under the effect of dopant site poisoning by iodine, which decreases the number of available dopant sites, the only active sites considered here for the coupling reaction. Without lateral interactions, each dopant atom could stabilize up to 6 iodine atoms on their mixed threefold sites; however, such configurations are not realistic in view of steric hindrance effects, due to the large size of the iodine atom. Therefore, to prevent such configurations from appearing

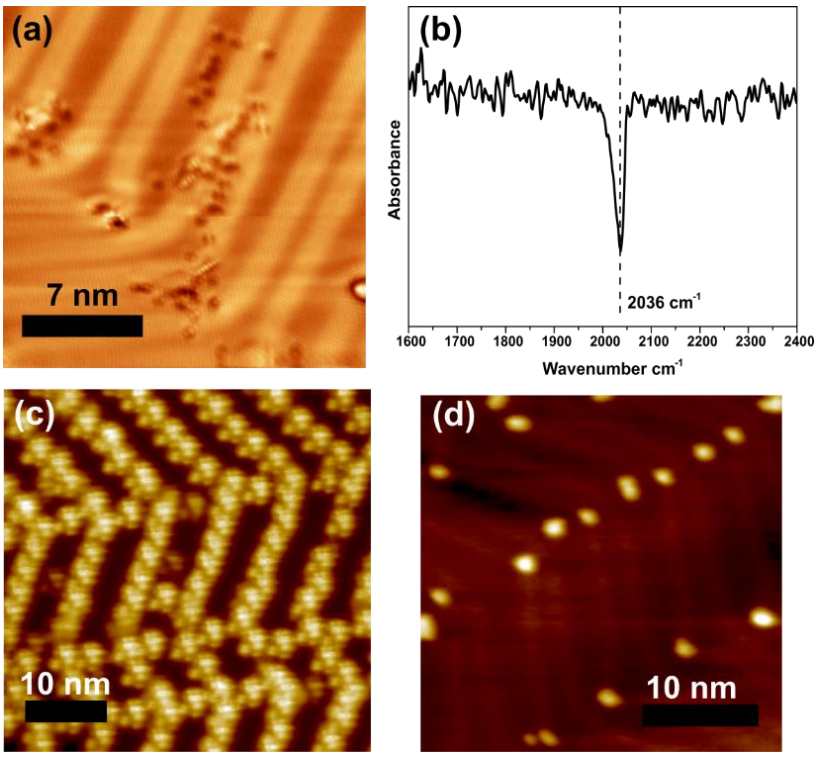

Figure 3.1: Characterization of the NiAu SAA surface and adsorption of the reactant methyl iodine **(a)** 80 K STM image of as prepared 0.02 ML NiAu SAA **(b)** CO RAIRs signal from 0.02 ML NiAu SAA **(c)** 5 K STM image of methyl iodide on a 0.02 ML NiAu SAA after a 100 K anneal to equilibrate the intact molecules **(d)** 5 K STM image of methyl iodide on 0.02

ML NiAu SAA surface after an anneal to 200 K that desorbs most of the molecules and cleaves the C-I bond of those with access to a Ni atom site.

in the KMC simulation, arbitrarily large lateral interactions were also added to the energetic model. In particular, we used an energy contribution of 1 eV for the interaction between two iodine atoms adsorbed on two of the six mixed threefold sites of the same dopant. Each TPD trace was obtained by averaging the TPD signals of 10 simulations in order the reduce the noise due to the stochastic nature of the simulations.

3.3 Results and Discussion

Figure 3.1a shows a representative STM image of the NiAu SAA surface formed by depositing 0.02 ML Ni on a Au(111) surface at 380 K and cooling to 80 K for imaging. As has been reported before, the Ni atoms are seen alloyed into the Au surface in the regions around the elbows of the Au(111) $22\times\sqrt{3}$ or "herringbone" reconstruction.[29] These regions contain an edge dislocation that provides an entry site for the diffusing Ni atom to incorporate into the Au surface.

In order to demonstrate that these Ni atom sites are isolated from one another in the Au surface we performed RAIRS of adsorbed CO as seen in Figure 3.1b. At low loadings (0.02 monolayer (ML) Ni), only one sharp feature was observed at 2036 cm^{-1} consistent with the presence of isolated Ni atom sites, as no lower frequency signal due to multi-fold binding to Ni is seen. Previous RAIRS studies of CO at atop sites on Ni(111) have reported

this feature at 2058 cm^{-1}. The difference between this and our NiAu SAA result is due to the intrinsic electronic difference between isolated Ni sites vs. extended Ni(111).[30–32] Further evidence for the lower frequency of the IR feature on the SAA comes from our DFT calculations that put this frequency at 1991 cm^{-1}, which is reasonably accurate when taking into consideration inherent errors in DFT calculations.

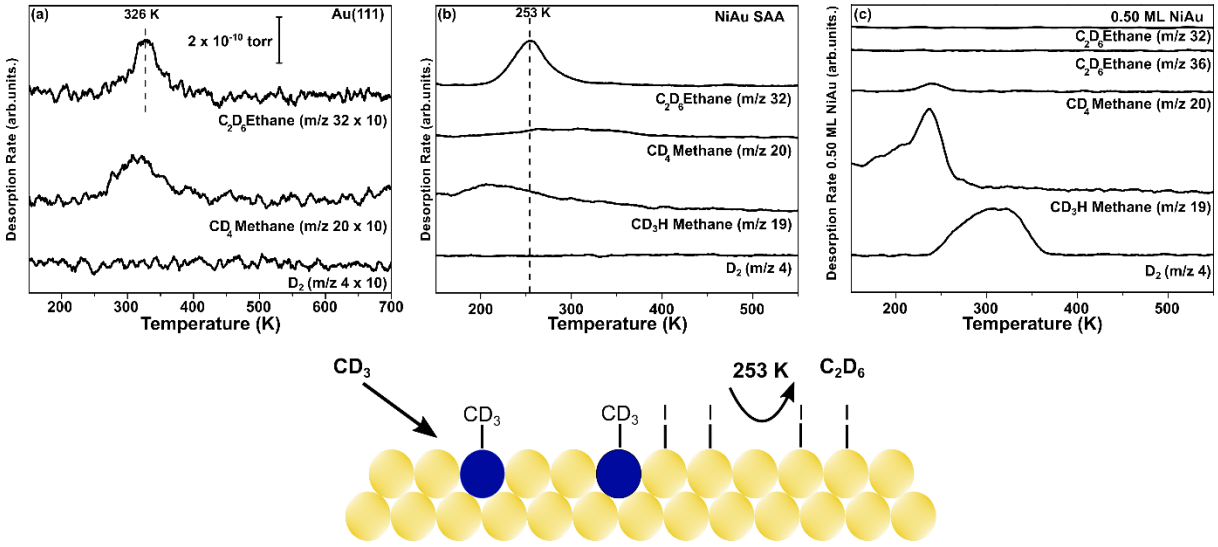

Figure 3.2: Reactivity of methyl iodine on Au(111) and NiAu model surfaces (a) TPD after deposition of 1 L (Langmuir) CD_3I on pure Au(111) demonstrating the relative inertness of the Au(111) surface. Note that TPD traces on bare Au(111) are multiplied by a factor of 10 to make the desorption peaks visible, and that the scale bar is the same for traces (b) and (c). (b) TPD after deposition of 1 L of CD_3I on 0.02 ML NiAu SAA showing ethane production and a small amount of methane produced from background hydrogenation of methyl groups. (c) TPD after deposition of 1 L of CD_3I showing that on a surface with a higher Ni loading (0.5 ML Ni) the extended Ni sites lead to methyl decomposition and that the coupling pathway that leads to the formation of ethane is not in effect at this higher Ni loading.

After characterizing the structure of the NiAu SAA model surface we used TPD to study the reactivity of methyl groups on the surface. Due to the lack of CH_4 reactivity in ultra-high vacuum experiments, we used methyl iodide to populate the NiAu SAA surface with methyl groups and study their coupling chemistry. STM measurements of methyl iodide molecules on the surface revealed that before the reaction, methyl iodide molecules are present at both the Au(111) herringbone reconstruction elbows where the Ni is present, as well as on the Au bare surface between these regions (Figure 3.1c). The linear ordering of methyl iodine molecules seen in this image is caused by the soliton walls of the herringbone reconstruction (seen in Figure 3.1a) that serve to corral the molecules between them.[33] However, after an anneal to 200 K that removes unreacted methyl iodide from the

surface, it can be seen that the only molecular species present on the surface are at the Ni sites (Figure 3.1d).

Figure 3.2 shows a series of TPD spectra that illustrate the reactivity of methyl iodide (MeI) on bare Au(111), a NiAu SAA surface, and higher coverage (0.5 ML) Ni on Au(111). On bare Au(111) the dissociation of the C-I bond is difficult as evidenced by the fact that most of the MeI desorbs intact from the surface around 170 K before the C-I bond can be cleaved. However, small amounts of defects like step edges inherent to the Au(111) surface are able to dissociate the C-I bond and the resulting methyl groups couple and desorb as ethane, as seen by the small ethane desorption peak at 326 K in Figure 3.2a.[34] Note that the reactivity of the Au(111) is so low that the desorption traces in Figure 3.2a have been multiplied by a factor of 10 for clarity. A small methane peak around 320 K was also observed due to methyl radical rejection and subsequent hydrogenation on the chamber walls, in agreement with previous studies.[34]

In contrast to Au(111), when 0.03 ML of Ni is added to the Au surface, a dramatic increase of reactivity is observed as shown in Figure 3.2b and larger amounts of ethane are seen desorbing at 253 K. At this temperature ethane desorption is limited by its formation on the surface and therefore its desorption temperature is representative of the activation barrier for ethane formation i.e. carbon-carbon coupling. Importantly, the much larger amounts of ethane evolved as compared to Au(111), and the fact that the ethane is formed around 80 K lower in temperature on the SAA compared to Au(111) reveal two important details. The first is that NiAu(111) SAAs facilitate low-temperature C-I cleavage that leads to a larger yield of ethane from the SAA vs. pure Au(111) from which most of the MeI

desorbs from the surface around 170 K before it can react. Secondly, C-C coupling that leads to the formation of ethane occurs at much lower temperature on the NiAu SAA (250 K vs. 320 K from Au(111)) meaning that Ni atom sites also catalyze the coupling step of the reaction. This carbon-carbon coupling on the NiAu SAA surface is selective and there is no evidence of decomposition products from our TPD measurements. The only other species observed, other than ethane, was methane desorbing from both the Au(111) surface as mentioned, and the NiAu SAA. The use of isotopic labelling experiments enabled us to further investigate the origin of this methane. Specifically, CD_3I was used to understand the role of background H_2 found in all ultra-high vacuum chambers. Figure 3.2 shows that fully deuterated ethane (C_2D_6) is the primary product desorbing from the NiAu SAA surface and that the methane produced is predominantly CD_3H. The production of CD_3H has been observed before and is observed because of background H_2 present in the chamber that is capable of hydrogenating adsorbed methyl groups.[12,35–40]

Furthermore, quantitative mass spectrometry was performed on the carbon species desorbing from the NiAu SAA surface and it was determined that there was a 1:1 relationship between Ni sites and carbon species desorbing as methane and ethane. This provides further evidence that the Ni atom sites are responsible for both C-I bond cleavage, as evidenced by the larger amounts of ethane formed on NiAu SAAs vs. pure Au(111), and the sp^3-sp^3 carbon-carbon coupling reaction step, as evidenced by ethane formation at a temperature ~ 75 K lower than pure Au(111).

In order to examine the reactivity of Ni ensembles in Au that are larger than one atom, we performed identical experiments on a 0.5 ML NiAu model surface as seen in

Figure 4.2. Interestingly, on this surface, which contains extended Ni ensembles, the methyl groups produced from the dissociation of CD_3I were not observed to undergo carbon-carbon coupling to produce ethane. Instead, they decomposed and underwent reaction with background hydrogen to produce deuterated methane CD_3H, as well as further decomposition that led to the desorption of D_2 above room temperature. Together, these TPD results demonstrate that individual, isolated Ni atoms in Au(111) serve as active sites for both C-I bond cleavage that initiates the reaction of methyl iodide, and for selective sp^3-sp^3 carbon-carbon coupling of surface-bound methyl groups to form ethane.

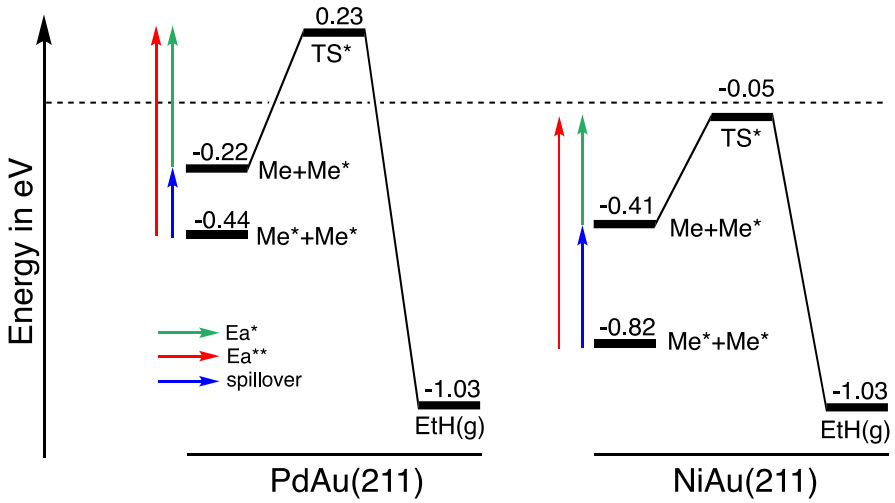

Figure 3.3. Energetics for the coupling of methyl groups on PdAu and NiAu SAA surfaces. In this energy diagram, the Pd and Ni single-atom sites are considered at the Au(211) facet and gold sites at the Au(111) facet. Me and Me* represent methyl adsorbed on a gold top site and a single-atom top site respectively. Energies are referenced with respect to clean surfaces and methyl groups on gold top sites (Me).

In order to further understand the experimental results and also compare the energetics of the reaction steps to previously reported PdAu SAAs, we performed DFT and KMC simulations. The main challenge when modelling the reactivity of gold-based single-atom alloys is to describe the active site properly. As previously mentioned, the transition metals used as surface dopants (Ni, Pd), tend to alloy into the Au surface at the elbows of the herringbone reconstruction where edge dislocations are present, which have Au sites with a coordination number lower than 9. We showed in our previous work on PdAu SAAs that, while the (111) surface provides a good model for Au sites, the (211) surface is necessary to describe the reactivity of Pd sites.[5] Similarly, we consider here that the Ni sites in the NiAu SAA are located at the (211) facet and that the Au sites are well described by the (111) surface. As with the PdAu SAA, the overall activation energy for the C-C coupling of methyl groups depends on the initial coverage and the associated representative initial state (see Figure 4.3 and 4a-c). For methyl group to dopant atom (Ni, Pd) ratios (denoted as σ) greater than 1, all the dopant top sites are occupied by methyl groups (referred to as Me*) and excess methyl groups are adsorbed on gold sites (referred to as Me) as represented in Figure 4.4b. For such coverages, the excess methyl groups at Au sites couple easily with dopant-bound Me* with a rather low activation energy Ea* of 0.36 eV on NiAu and 0.45 eV on PdAu (see barrier from Me+Me* in Figure 4.3). Now, for the case of $\sigma \leq 1$, all methyl species are adsorbed on dopant atom sites that are separated spatially from one another (as represented in Figure 4.4a) and the representative initial state for the coupling is Me*+Me* (instead of the previously described Me+Me*). For this situation, the two methyl groups (Me*) cannot react readily since they are physically distanced. In order for the reaction to occur, one of the two methyl groups must spill over

to gold (Me* → Me) and then couple with a dopant-bound Me*. This spillover of methyl from the dopant to Au is endothermic (see Table 4.1) and significantly raises the activation energy (denoted by Ea**) to 0.77 eV on NiAu and 0.67 eV on PdAu (compare red and green arrows in Figure 4.3).

Table 3.1. Reaction energies for the spillover of methyl and iodine species from the dopant atom sites to the host Au(111) metal surface and the exchange between iodine and methyl species adsorbed at the dopant sites on PdAu and NiAu SAA. Starred (*) adsorbates are bound to the dopant (which is considered at the step-edge of the (211) facet) and unstarred adsorbates are located on the Au(111) surface. The overall exchange process is the difference between the two elementary steps. Energies are given in eV.

	PdAu SAA	NiAu SAA
Spillover elementary steps		
Me* → Me	0.22	0.41
I* → I	0.36	0.62
Overall exchange process		
I* + Me → I + Me*	0.14	0.21

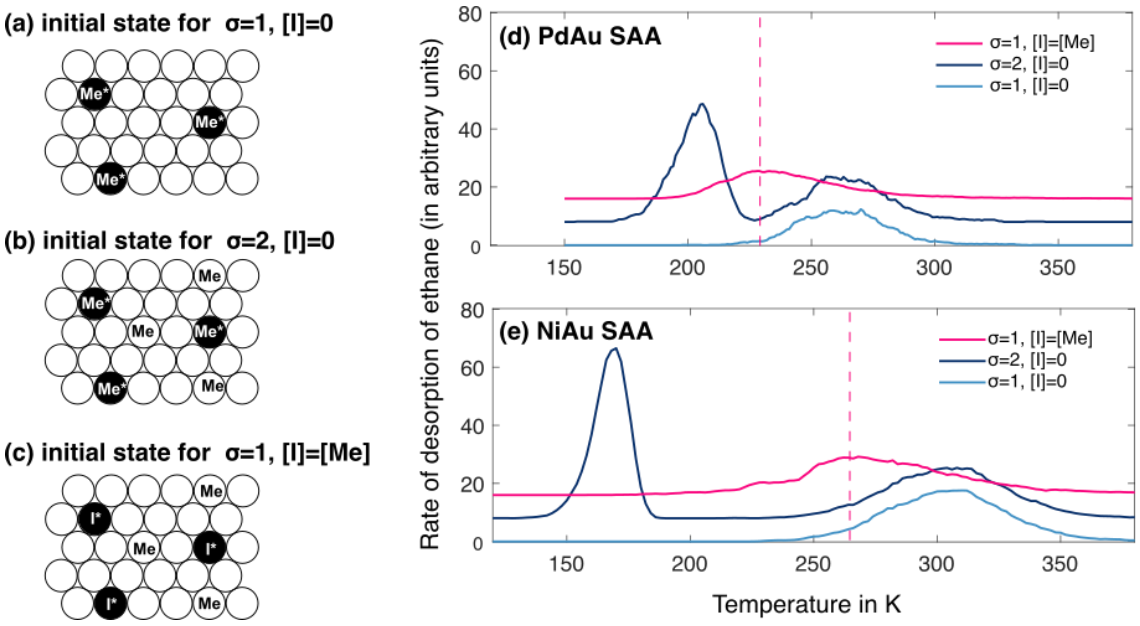

Figure 3.4. KMC-simulated TPD traces using the parameters computed at the DFT level. Different initial conditions were simulated (a-c). The traces correspond to the production of ethane on (d) PdAu SAA and (e) NiAu SAA. The dashed line indicates the position of the temperature peak when iodine is explicitly taken into account in the KMC simulations. The temperature ramps used in the simulations are as follows: 2 K/s for NiAu and 1 K/s for PdAu, consistent with experimental TPDs.

We then performed KMC simulations to directly compare the experimental TPDs with simulated TPDs based on the DFT calculations. We first discuss the case in which the effect of iodine is neglected. On both PdAu and NiAu SAAs, the KMC simulated TPDs show two ethane desorption peaks (dark blue traces in Figure 3.4d-e). The first one at low temperature (200 K for PdAu and 160 K for NiAu) is only seen for methyl group to dopant

atom ratios (σ) $>$ 1, and the second ethane desorption peak at higher temperature (255 K for PdAu and 310 K for NiAu) appears for values of σ above and below 1. This is in line with the coverage dependent activation energies (Ea* and Ea**) expected from our DFT calculations. Experimentally, $\sigma \sim 1$ and only one peak is seen around 250 K. This is why, in our previous work on the PdAu SAA, we had attributed this peak to the coupling of two methyls initially distanced on two different dopant sites (initial state Me*+Me*, see Figure 4.4a). In the case of NiAu SAA, this simulated peak shifts to 310 K, in poor agreement with experimental data (see Figure 3.2). This discrepancy between our experimental and theoretical results suggests that iodine, which is produced via the dissociated adsorption of methyl iodide and often thought to be a bystander, may actually play a role on the carbon-carbon coupling energetics.

Our DFT calculations indicate that the dopant sites stabilize iodine atoms to a larger extent than methyl groups as can been seen in Table 3.1. Therefore, when the systems are in a representative low-temperature initial state, all dopant sites should be occupied by iodine (I*) and all methyl groups should reside on gold sites (Me), as illustrated in Figure 3.4c. As the dopant is the active site for the coupling, the first step of the coupling reaction is the endothermic exchange of iodine with methyl (I* + Me $\rightarrow$ I + Me* in Table 4.1). From this state, transient dopant-bound Me* can couple with a methyl group bound to gold. This brings the overall activation energy for carbon-carbon coupling to 0.59 eV for PdAu and 0.57 eV for NiAu. When taking this exchange equilibrium into account in the KMC simulations, the TPD traces show a broad peak at 235 K for PdAu and 260 K for NiAu (pink traces in Figure 3.4), in close agreement with experimental data (see Figure 3.2).

In the absence of iodine, our simulations have evidenced two regimes for the C-C coupling (see Figures 3.4d-e). When there is an excess of methyl, the dopant sites act as very efficient active sites. Dopant-bound methyls couple with excess methyls on gold sites at very low temperatures. When the methyl to dopant ratio becomes stoichiometric or sub-stoichiometric, every methyl is stabilized on physically distanced dopant sites. Hence, they need to overcome the thermodynamic barrier to spill over to gold and become reactive. In this regime, where there are more active sites than reactants, the reactant itself hinders the coupling and the latter can only happen at higher temperatures. This widens the temperature range under which methyls are present on the surface and may open the possibility for other undesired reactions to happen. When iodine is added in stoichiometric proportion with respect to the dopant, it pushes methyl onto gold, where it does not undergo any reactions. Methyl and iodine can transiently exchange, giving rise to a configuration that is particularly reactive towards the coupling to ethane. Because iodine poisons the active site to some extent, the low-temperature regime coupling happens at a moderate temperature. But more importantly, methyls never get trapped on the dopant site where then can only couple at a higher temperature and potentially decompose.

While this situation of competitive binding of iodine atoms to the active sites for methyl group coupling complicates the mechanistic picture of how the coupling reaction occurs, it allows us to make an interesting comparison to common, and very well understood, homogenously catalyzed coupling reactions. Specifically, homogeneous catalysts are typically metal centers surrounded by ligands (L) as seen in Figure 3.5. In order for a coupling reaction to proceed, one or two ligands must detach from the metal center so that the reactants (blue circles) bind to the metal center. The reactants

subsequently couple and desorb from the metal complex and the ligands are replaced. This is essentially the same mechanism that we have discovered for heterogeneous carbon-carbon coupling on NiAu and PdAu SAAs as shown in Figure 3.5. In an analogous manner the iodine "ligand" bound to the metal atom dopant must be exchanged with a methyl group that can then couple with a second methyl group supplied by the Au surface, and after the coupling is complete and ethane desorbs the metal center is again occupied by iodine.

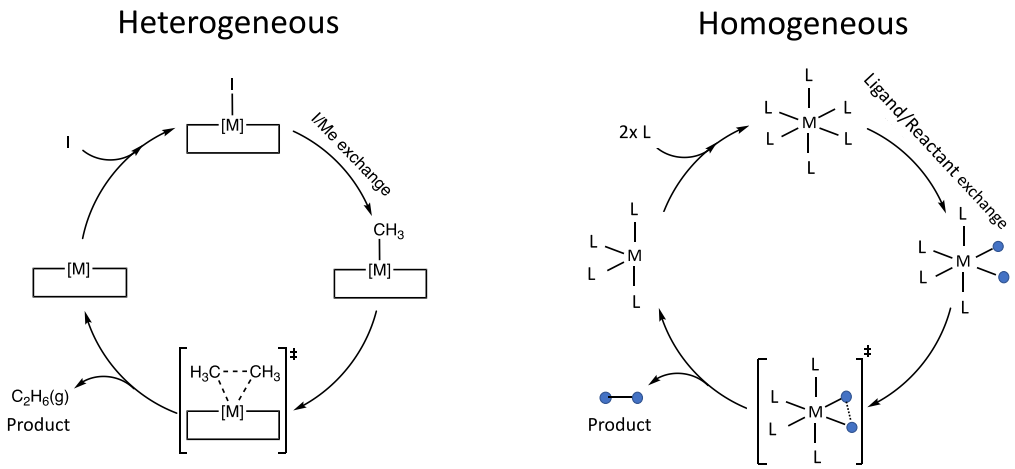

Figure 3.5. Comparing the mechanism of carbon-carbon coupling on SAA surfaces (heterogeneous) with a typical homogenously catalyzed coupling mechanism. In the heterogeneous catalytic cycle, adsorbates are exchanged between the active site M (Pd or Ni) and the non-reactive Au sites. In the homogeneous catalytic cycles, the species are exchanged between the active site M and the solvent.

3.4 Conclusions

Our experiments reveal that NiAu SAA surfaces, like PdAu SAAs, are able to catalyze sp^3-sp^3 carbon-carbon coupling of surface-bound methyl groups to form ethane. Unlike clusters of Ni or Pd (observed in alloys at higher dopant coverages) that are incapable of ethane formation and instead catalyze decomposition of the methyl groups, single Ni or Pd atoms catalyze both C-I cleavage in the reactant molecule and carbon-carbon coupling. The latter occurs at lower temperatures in the NiAu(111) SAA than on pure Au(111), providing evidence that the reaction indeed occurs at the Ni atom sites. While the iodine atom produced by C-I cleavage in methyl iodide is often thought to be a bystander in such coupling reactions, we treat it explicitly in our DFT calculations and find that surface-bound iodine atoms outcompete surface-bound methyl groups for binding to the Ni or Pd atom sites in Au. This effect is particularly pronounced for the NiAu SAA and we find that the energy to displace the iodine atom from the Ni active site must be considered in order to accurately model the experimental results and reproduce the correct desorption temperatures with KMC. This is analogous to the mechanism of coupling reactions on homogeneous catalysts in which ligands must detach from the active metal center in order for the reactants to be activated and the coupling product produced.

3.5 References

(1) Galadima, A.; Muraza, O. Revisiting the Oxidative Coupling of Methane to Ethylene in the Golden Period of Shale Gas: A Review. *J. Ind. Eng. Chem.* **2016**, *37*, 1–13. https://doi.org/10.1016/j.jiec.2016.03.027.

(2) Yin, L.; Liebscher, J. Carbon-Carbon Coupling Reactions Catalyzed by Heterogeneous Palladium Catalysts. *Chem. Rev.* **2007**, *107* (1), 133–173. https://doi.org/10.1021/cr0505674.

(3) Phan, N. T. S.; Van Der Sluys, M.; Jones, C. W. On the Nature of the Active Species in Palladium Catalyzed Mizoroki-Heck and Suzuki-Miyaura Couplings - Homogeneous or Heterogeneous Catalysis, a Critical Review. *Adv. Synth. Catal.* **2006**, *348* (6), 609–679. https://doi.org/10.1002/adsc.200505473.

(4) Chen, Z.; Vorobyeva, E.; Mitchell, S.; Fako, E.; Ortuño, M. A.; López, N.; Collins, S. M.; Midgley, P. A.; Richard, S.; Vilé, G.; Pérez-Ramírez, J. A Heterogeneous Single-Atom Palladium Catalyst Surpassing Homogeneous Systems for Suzuki Coupling. *Nat. Nanotechnol.* **2018**, *13* (August), 1–6. https://doi.org/10.1038/s41565-018-0167-2.

(5) Réocreux, R.; Uhlman, M.; Thuening, T.; Kress, P.; Hannagan, R.; Stamatakis, M.; Sykes, E. C. H. Efficient and Selective Carbon-Carbon Coupling on Coke-Resistant PdAu Single-Atom Alloys. *Chem. Commun.* **2019**, *55* (100), 15085–15088. https://doi.org/10.1039/c9cc07932g.

(6) Xi, M.; Bent, B. E. Mechanisms of the Ullmann Coupling Reaction in Adsorbed Monolayers. *J. Am. Chem. Soc.* **1993**, *115* (16), 7426–7433. https://doi.org/10.1021/ja00069a048.

(7) Fan, Q.; Gottfried, J. M.; Zhu, J. Surface-Catalyzed C-C Covalent Coupling Strategies toward the Synthesis of Low-Dimensional Carbon-Based

Nanostructures. *Acc. Chem. Res.* **2015**, *48* (8), 2484–2494. https://doi.org/10.1021/acs.accounts.5b00168.

(8) Fairbrother, D. H.; Peng, X. D.; Viswanathan, R.; Stair, P. C.; Trenary, M.; Fan, J. Carbon-Carbon Coupling of Methyl Groups on Pt(111). *Surf. Sci.* **1993**, *285* (1–2). https://doi.org/10.1016/0039-6028(93)90900-5.

(9) Kanuru, V. K.; Kyriakou, G.; Beaumont, S. K.; Papageorgiou, A. C.; Watson, D. J.; Lambert, R. M. Sonogashira Coupling on an Extended Gold Surface in Vacuo: Reaction of Phenylacetylene with Iodobenzene on Au(111). *J. Am. Chem. Soc.* **2010**, *132* (23), 8081–8086. https://doi.org/10.1021/ja1011542.

(10) Borkowski, T.; Trzeciak, A. M.; Bukowski, W.; Bukowska, A.; Tylus, W.; Kepiński, L. Palladium(0) Nanoparticles Formed in Situ in the Suzuki-Miyaura Reaction: The Effect of a Palladium(II) Precursor. *Appl. Catal. A Gen.* **2010**, *378* (1), 83–89. https://doi.org/10.1016/j.apcata.2010.02.004.

(11) Paul, A.; Michael, X.; Bent, B. E. Disproportionation and Coupling Reactions of Alkyl Iodides on a Au(111) Surface. **1993**.

(12) Lucci, F. R.; Darby, M. T.; Mattera, M. F. G.; Ivimey, C. J.; Therrien, A. J.; Michaelides, A.; Stamatakis, M.; Sykes, E. C. H. Controlling Hydrogen Activation, Spillover, and Desorption with Pd-Au Single-Atom Alloys. *J. Phys. Chem. Lett.* **2016**, *7* (3), 480–485. https://doi.org/10.1021/acs.jpclett.5b02400.

(13) Kresse, G.; Hafner, J. Ab Initio Molecular Dynamics for Liquid Metals. *Phys. Rev. B* **1993**, *47*, 558–561. https://doi.org/10.1103/PhysRevB.47.558.

(14) Kresse, G.; Furthmüller, J. Efficient Iterative Schemes for Ab Initio Total-Energy Calculations Using a Plane-Wave Basis Set. *Phys. Rev. B* **1996**, *54*, 11169–11186. https://doi.org/10.1103/PhysRevB.54.11169.

(15) Kresse, G.; Furthmüller, J. Efficiency of Ab-Initio Total Energy Calculations for Metals and Semiconductors Using a Plane-Wave Basis Set. *Comput. Mater. Sci.* **1996**, *6* (1), 15–50. https://doi.org/10.1016/0927-0256(96)00008-0.

(16) Dion, M.; Rydberg, H.; Schröder, E.; Langreth, D. C.; Lundqvist, B. I. Van Der Waals Density Functional for General Geometries. *Phys. Rev. Lett.* **2004**, *92*, 246401. https://doi.org/10.1103/PhysRevLett.92.246401.

(17) Klimeš, J.; Bowler, D. R.; Michaelides, A. Chemical Accuracy for the van Der Waals Density Functional. *J. Phys. Condens. Matter* **2010**, *22*, 022201. https://doi.org/10.1088/0953-8984/22/2/022201.

(18) Klimeš, J.; Bowler, D. R.; Michaelides, A. Van Der Waals Density Functionals Applied to Solids. *Phys. Rev. B - Condens. Matter Mater. Phys.* **2011**, *83* (19), 1–13. https://doi.org/10.1103/PhysRevB.83.195131.

(19) Klimeš, J.; Michaelides, A. Perspective: Advances and Challenges in Treating van Der Waals Dispersion Forces in Density Functional Theory. *J. Chem. Phys.* **2012**, *137*, 120901–120913. https://doi.org/10.1063/1.4754130.

(20) Blöchl, P. Projector Augmented-Wave Method. **1994**, *50*, 17953.

(21) Kresse, G.; Joubert, D. From Ultrasoft Pseudopotentials to the Projector

Augmented-Wave Method. *Phys. Rev. B* **1999**, *59*, 1758–1775. https://doi.org/10.1103/PhysRevB.59.1758.

(22) Monkhorst, H. J.; Pack, J. D. Special Points for Brillouin-Zone Integrations. *Phys. Rev. B* **1976**, *13*, 5188–5192. https://doi.org/10.1103/PhysRevB.13.5188.

(23) Sheppard, D.; Terrell, R.; Henkelman, G. Optimization Methods for Finding Minimum Energy Paths. *J. Chem. Phys.* **2008**, *128*, 134106. https://doi.org/10.1063/1.2841941.

(24) Henkelman, G.; Uberuaga, B. P.; Jónsson, H. A Climbing Image Nudged Elastic Band Method for Finding Saddle Points and Minimum Energy Paths. *J. Chem. Phys.* **2000**, *113*, 9901. https://doi.org/10.1063/1.1329672.

(25) Heyden, A.; Bell, A. T.; Keil, F. J. Efficient Methods for Finding Transition States in Chemical Reactions: Comparison of Improved Dimer Method and Partitioned Rational Function Optimization Method. *J. Chem. Phys.* **2005**, *123*, 224101. https://doi.org/10.1063/1.2104507.

(26) Henkelman, G.; Jónsson, H. A Dimer Method for Finding Saddle Points on High Dimensional Potential Surfaces Using Only First Derivatives. *J. Chem. Phys.* **1999**, *111*, 7010. https://doi.org/10.1063/1.480097.

(27) Stamatakis, M.; Vlachos, D. G. A Graph-Theoretical Kinetic Monte Carlo Framework for on-Lattice Chemical Kinetics. *J. Chem. Phys.* **2011**, *134* (21), 214115. https://doi.org/10.1063/1.3596751.

(28) Nielsen, J.; D'Avezac, M.; Hetherington, J.; Stamatakis, M. Parallel Kinetic Monte Carlo Simulation Framework Incorporating Accurate Models of Adsorbate Lateral Interactions. *J. Chem. Phys.* **2013**, *139* (22), 224706. https://doi.org/10.1063/1.4840395.

(29) Wang, Z.-T.; Darby, M. T.; Therrien, A. J.; El-Soda, M.; Michaelides, A.; Stamatakis, M.; Sykes, E. C. H. Preparation, Structure, and Surface Chemistry of Ni–Au Single Atom Alloys. *J. Phys. Chem. C* **2016**, *120* (25), 13574–13580. https://doi.org/10.1021/acs.jpcc.6b03473.

(30) Kruppe, C. M.; Krooswyk, J. D.; Trenary, M. Polarization-Dependent Infrared Spectroscopy of Adsorbed Carbon Monoxide to Probe the Surface of a Pd/Cu(111) Single-Atom Alloy. *J. Phys. Chem. C* **2017**, *121* (17), 9361–9369. https://doi.org/10.1021/acs.jpcc.7b01227.

(31) Patel, D. A.; Hannagan, R. T.; Kress, P. L.; Schilling, A. C.; Çlnar, V.; Sykes, E. C. H. Atomic-Scale Surface Structure and CO Tolerance of NiCu Single-Atom Alloys. *J. Phys. Chem. C* **2019**, *123* (46), 28142–28147. https://doi.org/10.1021/acs.jpcc.9b07513.

(32) Hannagan, R. T.; Patel, D. A.; Cramer, L. A.; Schilling, A. C.; Ryan, P. T. P.; Larson, A. M.; Çınar, V.; Wang, Y.; Balema, T. A.; Sykes, E. C. H. Combining STM, RAIRS and TPD to Decipher the Dispersion and Interactions Between Active Sites in RhCu Single-Atom Alloys. *ChemCatChem* **2020**, *12* (2), 488–493. https://doi.org/10.1002/cctc.201901488.

(33) Sykes, E. C. H.; Mantooth, B. A.; Han, P.; Donhauser, Z. J.; Weiss, P. S. Substrate-Mediated Intermolecular Interactions: A Quantitative Single Molecule Analysis. *J. Am. Chem. Soc.* **2005**, *127* (19), 7255–7260. https://doi.org/10.1021/ja0472331.

(34) Paul, Anumita; Bent, B. Alkyl Coupling on Copper, Silver, and Gold: Correlation between the Coupling Rate and the Metal-Alkyl Bond Strength. *J. Catal.* **1994**, 264–271.

(35) Darby, M. T.; Stamatakis, M.; Michaelides, A.; Sykes, E. C. H. Lonely Atoms with Special Gifts: Breaking Linear Scaling Relationships in Heterogeneous Catalysis with Single-Atom Alloys. *J. Phys. Chem. Lett.* **2018**, acs.jpclett.8b01888. https://doi.org/10.1021/acs.jpclett.8b01888.

(36) Lucci, F. R.; Marcinkowski, M. D.; Lawton, T. J.; Sykes, E. C. H. H2 Activation and Spillover on Catalytically Relevant Pt-Cu Single Atom Alloys. *J. Phys. Chem. C* **2015**, *119* (43), 24351–24357. https://doi.org/10.1021/acs.jpcc.5b05562.

(37) Aich, P.; Wei, H.; Basan, B.; Kropf, A. J.; Schweitzer, N. M.; Marshall, C. L.; Miller, J. T.; Meyer, R. Single-Atom Alloy Pd-Ag Catalyst for Selective Hydrogenation of Acrolein. *J. Phys. Chem. C* **2015**, *119* (32), 18140–18148. https://doi.org/10.1021/acs.jpcc.5b01357.

(38) Pei, G. X.; Liu, X. Y.; Wang, A.; Lee, A. F.; Isaacs, M. A.; Li, L.; Pan, X.; Yang, X.; Wang, X.; Tai, Z.; Wilson, K.; Zhang, T. Ag Alloyed Pd Single-Atom Catalysts for Efficient Selective Hydrogenation of Acetylene to Ethylene in Excess

Ethylene. *ACS Catal.* **2015**, *5* (6), 3717–3725. https://doi.org/10.1021/acscatal.5b00700.

(39) Marcinkowski, M. D.; Jewell, A. D.; Stamatakis, M.; Boucher, M. B.; Lewis, E. A.; Murphy, C. J.; Kyriakou, G.; Sykes, E. C. H. Controlling a Spillover Pathway with the Molecular Cork Effect. *Nat. Mater.* **2013**, *12* (6), 523–528. https://doi.org/10.1038/nmat3620.

(40) Kyriakou, G.; Boucher, M. B.; Jewell, A. D.; Lewis, E. A.; Lawton, T. J.; Baber, A. E.; Tierney, H. L.; Flytzani-Stephanopoulos, M.; Sykes, E. C. H. Isolated Metal Atom Geometries as a Strategy for Selective Heterogeneous Hydrogenations. *Science (80-.).* **2012**, *335* (6073), 1209–1212. https://doi.org/10.1126/science.1215864.

Chapter 4: Controlling Hydrocarbon (De)Hydrogenation Pathways with Bifunctional PtCu Single-Atom Alloys

This chapter was modified from an original paper published in 2021 by the same title, PL Kress et al. from the Journal of Physcial Chemistry Letters, Volume 11, Issue 20. DFT calculations were performed by Romain Réocreux and Michail Stamatakis from UCL.

4.1 Introduction

Single-atom alloys (SAAs) are an emerging class of heterogeneous catalysts in which a small amount of a more reactive dopant metal is atomically dispersed in the surface layer of a less reactive host metal.[1–3] Due to their ability to perform a range of efficient and selective chemistries, there has been growing interest in this class of single-site catalysts in recent years.[4–10] Specifically SAAs have been demonstrated to efficiently catalyze hydrogenation,[9,11] C-C coupling,[12,13] NO reduction,[14] oxygen reduction,[15] and coke-free C-H activation[16,17] among many other reactions.[1,18] Due to the well-defined nature of their active sites and the possibility for intermediates to spill over from dopant to host, these SAAs can break traditional linear scaling relationships that limit catalytic performance.[1,6,19,20] Furthermore, the weaker binding of most species to SAA surfaces vs. traditional catalytic metals like Pt, Pd and Ni offers solutions to common problems that plague these catalysts like CO poisoning and coking by carbonaceous species. Coking is of particular interest in the industrial hydrogenation and dehydrogenation of organic compounds (such as hydrocarbons and oxygenates), as strong binding of carbonaceous species leads to catalyst deactivation.

Surface bound alkyl groups are ubiquitous in many reaction pathways and the relative ease of their hydrogenation/dehydrogenation is critical to product selectivity.[21] Ethyl groups are prototypical intermediates that can be hydrogenated to ethane, dehydrogenated to ethylene via β-hydride elimination, or decomposed to CH_x fragments on the surface. β-hydride elimination is the most facile dehydrogenation step on most metal surfaces.[21–23] Therefore, driving a catalytic process involving alkyl groups towards the desired products (alkanes, olefins) is non-trivial and, as we show here, SAAs may be key to achieving greater control over the product selectivity. Herein, we take a surface science and theory approach to understanding and quantifying the energetics of these relevant reaction pathways on PtCu SAAs. Relevant to the present work, the hydrogenation and dehydrogenation of ethyl groups have been studied on both Cu and Pt surfaces. On Cu(111), ethyl only undergoes a β-elimination to yield hydrogen and ethylene, which desorbs at 247 K.[24] Studies show that while Cu(111) can enable H/D exchange reactions in adsorbed ethyl, it is incapable of hydrogenating ethyl groups to ethane.[25] This suggests the existence of a surface-bound ethyl group that will not fully hydrogenate to ethane, consistent with a DFT investigation by Xu *et al.*[26] showing that ethylene would rather desorb from copper than hydrogenate to ethane. In contrast, on Pt(111) the picture is much more complex. There is experimental and theoretical evidence of a large dehydrogenation reaction network that leads to various C_2H_x surface-bound intermediates such as vinyl (CH_2CH), vinylidene (CH_2C), and particularly stable ethylidyne (CH_3C).[27–29] Dehydrogenation steps via both α- and β-hydride elimination are particularly active on Pt. These unsaturated intermediates ultimately undergo C-C cleavage and decompose to coke

at high temperatures, producing large amounts of adsorbed hydrogen, which can either desorb as H_2 or hydrogenate C_1 and C_2 species to methane and ethane respectively. The carbon left behind on the Pt surface poisons the active sites, which is a common problem for hydrocarbon conversion on Pt catalysts.[30–32] For the selective interconversion of C-C and C=C bonds, the ideal catalyst should be able to hydrogenate unsaturated adsorbates (like Pt can do), and conversely, dehydrogenate alkyl groups to alkenes (like Cu and Pt) but without deactivation due to coking seen for pure Pt. PtCu alloys appear promising for this reaction, and in particular PtCu SAAs which are known to enable facile C-H activation and are coke resistant.[17] To gain insight into the reactivity and degree of bifunctionality of such alloys, we combined theory and experiments to understand the disproportionation of a model adsorbate, namely ethyl, to ethane and ethene on PtCu alloys. Results from our theoretical model enabled us to experimentally demonstrate that the selectivity of ethyl (de)hydrogenation can be controlled by adjusting the surface coverage of hydrogen.

4.2 Results and Discussion

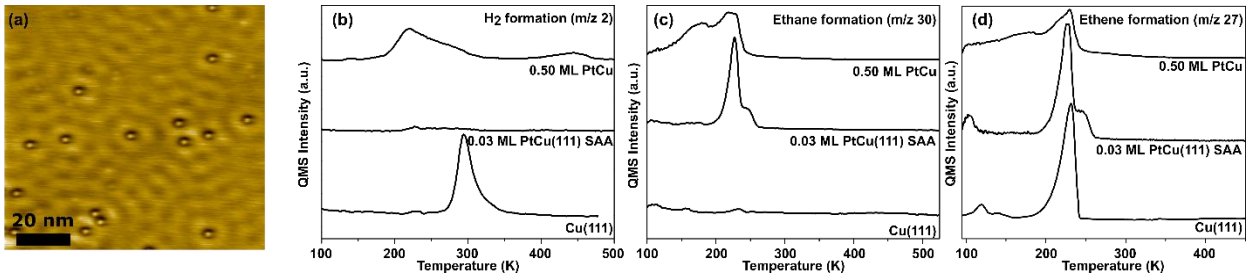

Figure 4.1. (a) STM image of PtCu(111) SAA. (b) TPD traces for hydrogen desorption from Cu(111), 0.03 ML PtCu SAA and 0.50 ML PtCu respectively after deposition of 6 L

of ethyl iodide. (c) Ethane and (d) ethene formation from the same three experiments showing that Pt is necessary for the hydrogenation of ethyl groups to ethane.

In order to probe β-hydride elimination reactivity which is central to the interconversion of molecules with C=C and C-C bonds, we performed Temperature Programmed Desorption (TPD) experiments to investigate the reaction pathways of ethyl groups generated in situ from ethyl iodide on PtCu alloys with different surface compositions. Ethyl iodide is known to react on Cu at low temperature (~140 K) to produce adsorbed Et groups and I atoms.[33] When a saturation dose of ethyl iodide (6L) is deposited on pure Cu(111), TPD experiments reveal that ethylene desorbs at 230 K and hydrogen at 300 K (Figure 4.1d and b), with no desorption of ethane (Figure 4.1c). The surface-bound hydrogen atoms resulting from the β-hydride elimination of surface-bound ethyl groups therefore act as spectators that do not participate to the production of ethane. In contrast, when the same experiments are carried out on 0.5 monolayer (ML) PtCu surface alloys, ethane is produced and desorbs at 150-250 K (Figure 4.1c), followed by the desorption of H_2 between 200-300 K (Figure 4.1b). Furthermore, the TPD spectra exhibit a second H_2 desorption feature at higher temperature (~ 450 K). Related to this, it is known that reaction of ethyl groups on pure Pt surfaces leads to very similar TPD spectra,[22] indicating that our 0.5 ML Pt surface alloys consist of extended Pt-islands with a reactivity comparable to that of pure Pt. C-H activation can occur at a low temperature on Pt, producing hydrogen that can either hydrogenate surface-bound ethyl groups or associatively desorb as H_2.[22,34] The second H_2 desorption peak at higher temperature results from further decomposition.[34] The complexity of the TPD traces from our 0.5 ML PtCu(111) alloys is representative of the many reaction pathways that occur on extended Pt surfaces.[34]

Moving to the single-atom limit, for 0.03 ML PtCu(111) SAA surfaces, we find that ethyl groups react to produce ethane and ethylene at 230 K as seen in Figure 4.1c and d, but no H_2 is produced, contrary to the behavior of pure Cu, pure Pt[35] and 0.5 ML PtCu. Scanning Tunneling microscopy (STM) imaging reveals that the 0.03 ML PtCu(111) alloy is indeed a SAA, as the surface Pt atoms are atomically dispersed in the surface of Cu (Figure 4.1a), in agreement with previous experimental and theoretical studies.[36–39] The hydrogenation of ethyl to ethane, which is not possible on pure Cu, is therefore catalyzed by individual, isolated Pt atoms in the surface layer of Cu(111). By comparing to our 0.5 ML PtCu data, we see that reducing the Pt site ensembles down to single-atoms prevents the adsorbates from fully dehydrogenating and decomposing to yield high temperature H_2. This indicates that the PtCu SAA is a bifunctional surface on which Cu performs the dehydrogenation step while the Pt sites facilitate the hydrogenation without decomposition. Our DFT results (see Scheme S1) support this hypothesis, and are in line with previously reported studies.[40,41] Briefly, while Pt(111) stabilizes most C_2H_x ($2 \leq x \leq 6$) species on the surface (with ethylidyne CH_3C being the most stable), PtCu(111) SAAs only stabilize ethane, ethyl and π-bonded[42] ethylene, greatly simplifying the reaction network found on Pt(111) and thereby only enabling desired C=C/C-C interconversion steps.

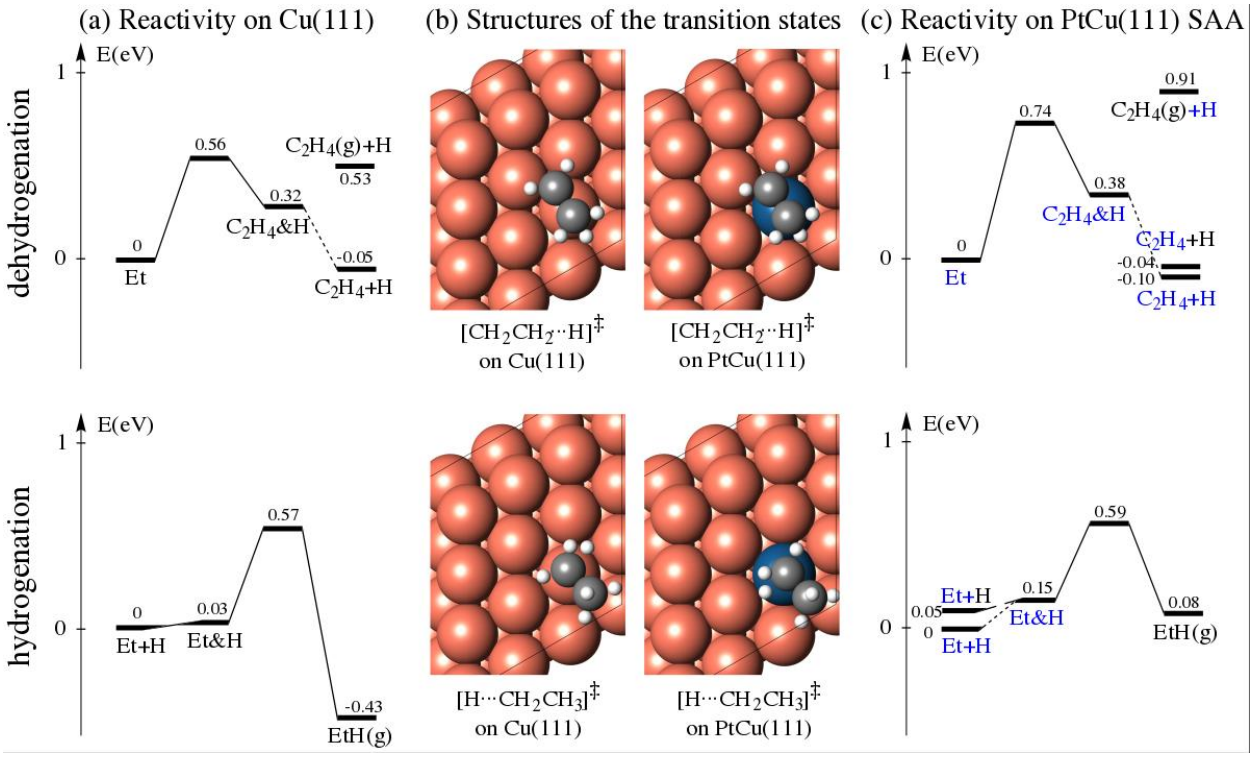

Figure 4.2. DFT-proposed mechanism for the hydrogenation and dehydrogenation of surface-bound ethyl (Et) groups. The energetics of the different reaction steps are given for (a) Cu(111) and (c) PtCu(111) SAA. The structures of the transition states are given in (b). A&B represents the co-adsorbed state of A and B while A+B represents the state of infinite separation on the surface. Adsorbates on Cu and PtCu mixed sites are reported in black and blue respectively. All species are surface-bound unless explicitly denoted as gas species by '(g)'.

In order to more fully elucidate the product selectivity observed in experiments, we performed DFT calculations to quantify the energetics of the different reaction steps, placing particular focus on the activation energies for both the hydrogenation and dehydrogenation of ethyl groups on Cu(111) and PtCu(111) SAA surfaces. In Figure 4.2a

(top panel) it can be seen that on Cu(111), the dehydrogenation of ethyl has an activation energy of 0.56 eV and is almost athermic. The hydrogenation step shows a similar activation energy, 0.57 eV (Figure 4.2b, bottom panel), which is surprising given that our experiments show that Cu cannot hydrogenate ethyl groups, and we will return to this point later in the paper. On the PtCu(111) SAA surface, the similar stabilization of both ethyl and ethylene on the Pt site (-0.42 eV for both adsorbates compared to Cu sites) keeps the dehydrogenation step athermic. Interestingly, the transition state on the SAA does not show the same extent of stabilization as the initial and final states. leading to a barrier of 0.74 eV, and this is in spite of the very similar geometries on both surfaces (Figure 4.2b). Pt sites are therefore unlikely to compete with Cu sites in the ethyl dehydrogenation step. However, the Pt single atom sites open a hydrogenation pathway with an overall activation energy of 0.54-0.59 eV (depending on whether hydrogen is adsorbed on either Cu or Pt sites).

Crucially, the activation energy just noted is very similar to that of the hydrogenation on Cu (0.57 eV), which might seem at odds with the experimental data, as this process is not observed on pure Cu by either ourselves or others.[43] One might argue that since ethyl and hydrogen bind more strongly on Pt, the latter site would be responsible for the hydrogenation. However, this could be counteracted by the (much) larger population of Cu sites relative to Pt. It is also interesting that even though hydrogenation and dehydrogenation have similar barriers on Cu, only the latter is observed experimentally. This could be attributed to the different reaction orders: the second-order hydrogenation step might not be able to compete with the first-order dehydrogenation step on Cu, unless hydrogen is present at sufficiently high surface coverages.

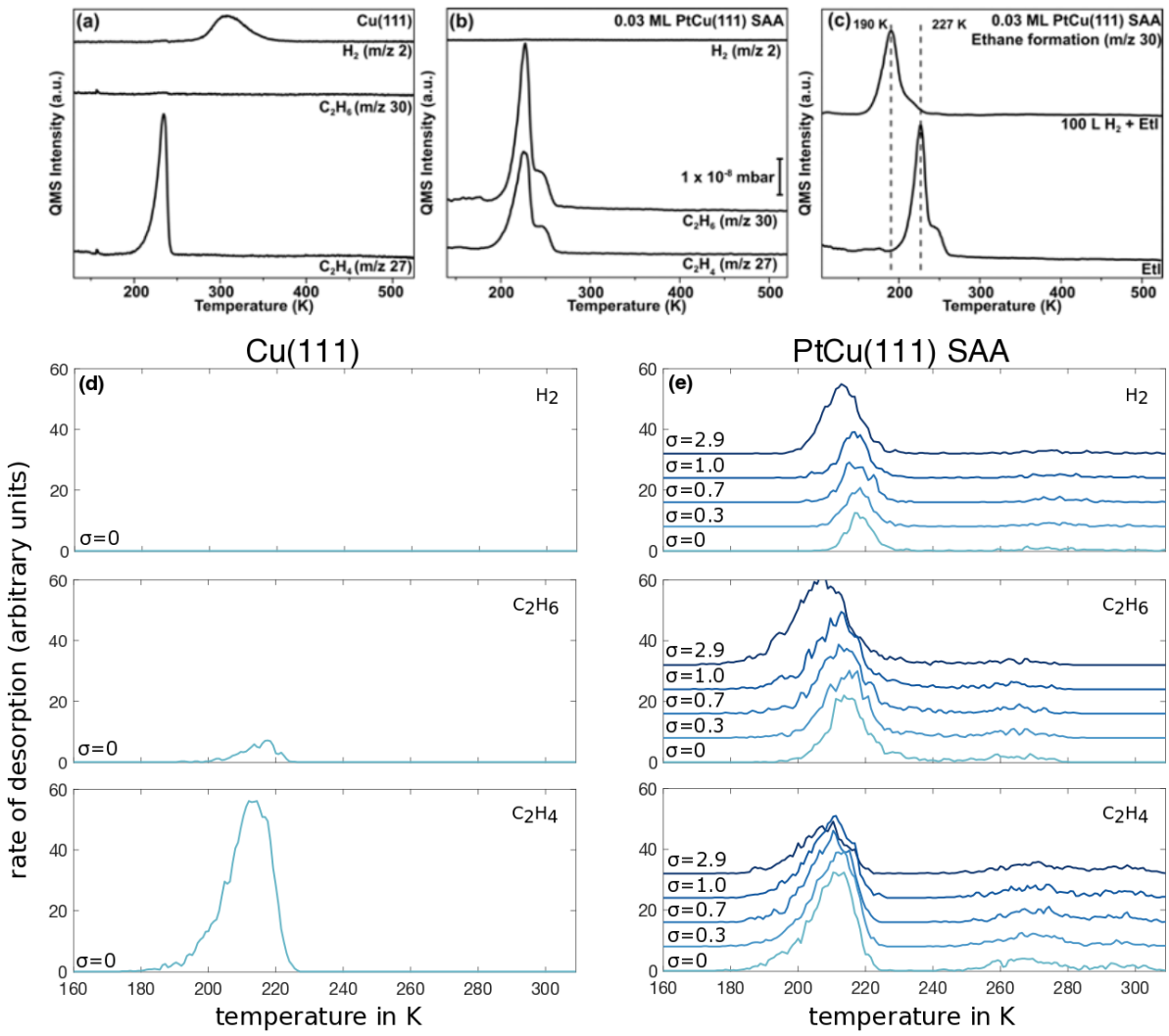

Figure 4.3. Experimental (a-c) and simulated (d-e) TPD spectra (hydrogen, ethane and ethylene) revealing the reactivity of ethyl groups on different surfaces. Experimental TPD Traces (after saturation with 6 L ethyl iodide exposure) on (a) pure Cu(111), (b) 0.03 ML PtCu(111) SAA, (c) 0.03 ML PtCu(111) SAA pre-covered with hydrogen. Simulated TPD spectra on (d) pure Cu(111) and (e) 0.03 ML PtCu(111) SAA with various amounts of pre-covered hydrogen, expressed as $\sigma=[H]_0:[Pt]$. Each simulated TPD signal is the average of 10 different simulations for a given initial coverage of H. The traces are shifted vertically for clarity.

To elucidate the complex interplay between these effects and identify the preferred reaction pathway(s) we adopted a kinetic modelling approach. We performed DFT-parametrized Kinetic Monte Carlo (kMC) simulations that could be directly compared with TPD experiments in order to obtain a much detailed mechanistic picture of these reaction steps. Experimentally, on both Cu(111) and the PtCu(111) SAA, ethylene is produced at around 230 K (see TPD spectra in Figure 4.3a-b). Simulations show that ethylene indeed desorbs at the same temperature on the different surfaces (see simulated TPD spectra in Figure 4.3d-e). The position of the simulated desorption peak temperature (215 K) agrees well with the experimental data. On pure Cu(111), a small fraction of ethyl ($\sim 7.1 \pm 0.2\%$) is hydrogenated by the endogenously produced hydrogen atoms. Importantly, almost equal amounts of ethane and ethylene are synchronously produced on PtCu(111) SAAs. Our kMC simulations show that the hydrogenation is more than one order of magnitude faster ($\sim$ 30 times) on single atom Pt sites than on Cu sites, and now competes with the dehydrogenation pathway on Cu sites. This confirms the bifunctional nature of the model catalyst whereby each metal performs one elementary step of the reaction. Moreover, hydrogen reaches lower coverages on PtCu compared to pure Cu due to the facile recombination of hydrogen and ethyl groups towards ethane on Pt sites. Since ethane desorbs rapidly, the net effect is hydrogen depletion from the PtCu surface via this pathway. Since the hydrogenation step can only occur when hydrogen atoms are produced from the competing dehydrogenation route, the kinetics are coupled. To decouple these pathways, and potentially promote the hydrogenation reaction, our simulations suggest that we would need to add hydrogen to the surface. PtCu SAAs readily activate H_2 and enable

H atom spillover to Cu(111), as demonstrated experimentally.[11,44] Therefore, we tested our prediction experimentally by pre-dosing the SAA surface with hydrogen before running the ethyl iodide experiment. The experimental data in Figure 4.3c show that the ethane desorption peak derived from the hydrogenation step is shifted to a lower temperature, demonstrating that hydrogenation is indeed faster than dehydrogenation when not limited by the production of surface hydrogen as our modeling indicates.

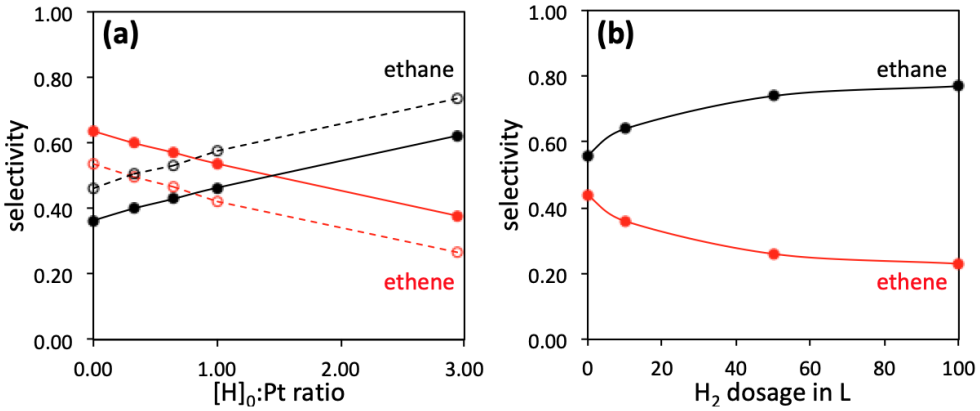

Figure 4.4. Effect adding surface hydrogen on the selectivity of ethyl disproportionation on 0.03 ML PtCu SAA. (a) Simulated selectivity as a function of the initial amount of H normalized by the number of Pt sites. The solid lines are for the full model. The dashed lines are for a model that does not allow for associative desorption of hydrogen. (b) Experimental selectivity to ethane vs. ethylene as a function of the amount of H_2 deposited.

Figure 4.4 shows good agreement between experiment and theory for the effect of pre-depositing H_2 on the surface and illustrates that by adjusting surface hydrogen coverage, the reaction selectivity can be controlled. Specifically, Figure 4.4 shows the simulated selectivity as a function of the initial coverage of hydrogen (Figure 4.4a) and the experimental selectivity as a function of the amount of H_2 deposited before the reaction (Figure 4.4b). At low hydrogen coverages, ethane and ethylene are produced in similar amounts. Adding hydrogen to the surface shifts the selectivity towards production of ethane as our model predicts. The fact that the experimental selectivity slightly favors ethane even when no H_2 is deposited suggests that, even when no hydrogen is added onto the surface, a small amount of background hydrogen from the UHV chamber is activated on the surface, as we have observed before.[11,44]

In summary, our theoretical and experimental investigation of the reactivity of ethyl species reveals that PtCu SAAs are bifunctional catalysts, with the dehydrogenation of ethyl occurring on the majority host Cu sites and the hydrogenation step catalyzed by the minority isolated Pt atom sites. These Pt atoms in the Cu(111) surface also act as an input channel for hydrogen atoms, the surface coverage of which is shown to control the selectivity of the ethyl disproportionation reaction. These low-temperature (de)hydrogenation reaction pathways are of general relevance for the heterogeneously catalyzed interconversion of C-C and C=C bonds and our findings indicate that the selectivity to alkanes vs. alkenes can be tuned by controlling the surface coverage of hydrogen.

4.3 Methods

Experiments. The surface science experiments were performed in an Omicron low-temperature STM and a separate TPD chamber. Quantitative mass spectrometry was performed on the TPD data to determine the amount of ethene and ethane evolution. The STM images were acquired at 5 K.

Simulations. The DFT calculations were performed using the optB86b-vdW functional[45,46] *as implemented in VASP 5.3.*[47–49] *The surface was modelled with a 4-layer p(4×4) slab. Within the approximations of harmonic Transition State Theory,*[50,51] *we evaluated the different rate constants to parameterize, without stiffness-scaling, a graph-theoretical kinetic Monte Carlo model (Zacros 2.0).*[52,53]

4.4 References

(1) M. T. Darby; M. Stamatakis; A. Michaelides; E. C. H. Sykes. Lonely Atoms with Special Gifts: Breaking Linear Scaling Relationships in Heterogeneous Catalysis with Single-Atom Alloys. *J. Phys. Chem. Lett.* **2018**, *9* (18), 5636–5646.

(2) G. Giannakakis; M. Flytzani-stephanopoulos; E. C. H. Sykes. Single-Atom Alloys as a Reductionist Approach to the Rational Design of Heterogeneous Catalysts. *Acc. Chem. Res.* **2018**, *52*, 237–247.

(3) G. Kyriakou; M. B. Boucher; A. D. Jewell; E. a Lewis; T. J. Lawton; A. E. Baber; H. L. Tierney; M. Flytzani-stephanopoulos; E. C. H. Sykes. Isolated Metal Atom

Geometries as a Strategy for Selective Heterogeneous Hydrogenations. *Science (80-.).* **2012**, *335* (March), 1209–1212.

(4) G. X. Pei; X. Y. Liu; X. Yang; L. Zhang; A. Wang; L. Li; H. Wang; X. Wang; T. Zhang. Performance of Cu-Alloyed Pd Single-Atom Catalyst for Semihydrogenation of Acetylene under Simulated Front-End Conditions. *ACS Catal.* **2017**, *7* (2), 1491–1500.

(5) X. Cui; W. Li; P. Ryabchuk; K. Junge; M. Beller. Bridging Homogeneous and Heterogeneous Catalysis by Heterogeneous Single-Metal-Site Catalysts. *Nat. Catal.* **2018**, *1* (6), 385–397.

(6) M. T. Darby; R. Réocreux; E. C. H. Sykes; A. Michaelides; M. Stamatakis. Elucidating the Stability and Reactivity of Surface Intermediates on Single-Atom Alloy Catalysts. *ACS Catal.* **2018**, *8* (6), 5038–5050.

(7) Z.-T. Wang; M. T. Darby; A. J. Therrien; M. El-Soda; A. Michaelides; M. Stamatakis; E. C. H. Sykes. Preparation, Structure, and Surface Chemistry of Ni–Au Single Atom Alloys. *J. Phys. Chem. C* **2016**, *120* (25), 13574–13580.

(8) M. D. Marcinkowski; J. Liu; C. J. Murphy; M. L. Liriano; N. A. Wasio; F. R. Lucci; M. Flytzani-Stephanopoulos; E. C. H. Sykes. Selective Formic Acid Dehydrogenation on Pt-Cu Single-Atom Alloys. *ACS Catal.* **2017**, *7* (1), 413–420.

(9) G. X. Pei; X. Y. Liu; A. Wang; A. F. Lee; M. A. Isaacs; L. Li; X. Pan; X. Yang; X. Wang; Z. Tai; et al. Ag Alloyed Pd Single-Atom Catalysts for Efficient Selective Hydrogenation of Acetylene to Ethylene in Excess Ethylene. *ACS Catal.* **2015**, *5*

(6), 3717–3725.

(10) A. Wang; J. Li; T. Zhang. Heterogeneous Single-Atom Catalysis. *Nat. Rev. Chem.* **2018**, *2* (6), 65–81.

(11) F. R. Lucci; J. Liu; M. D. Marcinkowski; M. Yang; L. F. Allard; M. Flytzani-Stephanopoulos; E. C. H. Sykes. Selective Hydrogenation of 1,3-Butadiene on Platinum–Copper Alloys at the Single-Atom Limit. *Nat. Commun.* **2015**, *6*, 8550.

(12) L. Zhang; A. Wang; J. T. Miller; X. Liu; X. Yang; W. Wang; L. Li; Y. Huang; C. Y. Mou; T. Zhang. Efficient and Durable Au Alloyed Pd Single-Atom Catalyst for the Ullmann Reaction of Aryl Chlorides in Water. *ACS Catal.* **2014**, *4* (5), 1546–1553.

(13) R. Réocreux; M. Uhlman; T. Thuening; P. Kress; R. Hannagan; M. Stamatakis; E. C. H. Sykes. Efficient and Selective Carbon–Carbon Coupling on Coke-Resistant PdAu Single-Atom Alloys. *Chem. Commun.* **2019**, *55* (100), 15085–15088.

(14) F. Zing; J. Jeon; T. Toyao; K. Shimizu; S. Furukawa. Cu–Pd Single-Atom Alloy Catalyst for Highly Efficient NO Reduction. *Chem. Sci.* **2019**.

(15) L. Zhang; H. Liu; S. Liu; M. N. Banis; J. Li; L. Yang; M. Markiewicz; Y. Zhao; R. Li; M. Zheng; et al. Pt / Pd Single Atom Alloys as Highly Active Electrochemical Catalysts and the Origin of Enhanced Activity Pt / Pd Single Atom Alloys as Highly Active Electrochemical Catalysts and the Origin of Enhanced Activity. *ACS Catal.* **2019**.

(16) G. Sun; Z.-J. Zhao; R. Mu; S. Zha; L. Li; S. Chen; K. Zang; J. Luo; Z. Li; S. C.

Purdy; et al. Breaking the Scaling Relationship via Thermally Stable Pt/Cu Single Atom Alloys for Catalytic Dehydrogenation. *Nat. Commun.* **2018**, *9* (1), 4454.

(17) M. D. Marcinkowski; M. Darby; J. Liu; J. Wimble; F. R. Lucci; S. Lee; A. Michaelides; Flytzani-Stephanopoulos; M. Stamatakis; E. C. H. Sykes. Pt/Cu Single-Atom Alloys as Coke Resistant Catalysts for Efficient C-H Activation. *Nat. Chem.* **2018**.

(18) R. T. Hannagan; G. Giannakakis; M. Flytzani-stephanopoulos; E. C. H. Sykes. Single-Atom Alloy Catalysis.

(19) M. T. Greiner; T. E. Jones; S. Beeg; L. Zwiener; M. Scherzer; F. Girgsdies; S. Piccinin; M. Armbrüster; A. Knop-Gericke; R. Schlögl. Free-Atom-like d States in Single-Atom Alloy Catalysts. *Nat. Chem.* **2018**, *10* (10), 1008–1015.

(20) A. Khorshidi; J. Violet; J. Hashemi; A. A. Peterson. How Strain Can Break the Scaling Relations of Catalysis. *Nat. Catal.* **2018**, *1* (4), 263–268.

(21) Z. Ma; F. Zaera. Organic Chemistry on Solid Surfaces. *Surf. Sci. Rep.* **2006**, *61* (5), 229–281.

(22) F. Zaera. Direct Observation of Beta-Hydride Elimination Reactions on Metal Surfaces. *J. Am. Chem. Soc.* **1989**, No. 10, 8744–8745.

(23) J. G. Forbes; A. J. Gellman. The Beta-Hydride Elimination Mechanism in Adsorbed Alkyl Groups. *J. Am. Chem. Soc.* **1993**, *115* (14), 6277–6283.

(24) D. Sung; A. J. Gellman. Ethyl Iodide Decomposition on Cu(111) and Cu(221).

Surf. Sci. **2004**, *551* (1–2), 59–68.

(25) M. Xi. Evidence for an Eley–Rideal Mechanism in the Addition of Hydrogen Atoms to Unsaturated Hydrocarbons on Cu(111). *J. Vac. Sci. Technol. B Microelectron. Nanom. Struct.* **1992**, *10* (6), 2440.

(26) L. Xu; E. E. Stangland; M. Mavrikakis. Ethylene versus Ethane: A DFT-Based Selectivity Descriptor for Efficient Catalyst Screening. *J. Catal.* **2018**, *362*, 18–24.

(27) H. A. Aleksandrov; L. V Moskaleva; Z.-J. Zhao; D. Basaran; Z.-X. Chen; D. Mei; N. Rösch. Ethylene Conversion to Ethylidyne on Pd(111) and Pt(111): A First-Principles-Based Kinetic Monte Carlo Study. *J. Catal.* **2012**, *285* (1), 187–195.

(28) Y. Chen; D. G. Vlachos. Hydrogenation of Ethylene and Dehydrogenation and Hydrogenolysis of Ethane on Pt(111) and Pt(211): A Density Functional Theory Study. *J. Phys. Chem. C* **2010**, *114* (11), 4973–4982.

(29) Z. J. Zhao; J. P. Greeley. Identification of Surface Intermediates during Ethylidyne Formation on Pt(111) by Calculation of Infrared Intensities and Deuterium Isotope Shifts. *Surf. Sci.* **2015**, *640*, 112–118.

(30) F. Zaera; D. Chrysostomou. Propylene on Pt(111) II. Hydrogenation, Dehydrogenation, and H-D Exchange. *Surf. Sci.* **2000**, *457* (1), 89–108.

(31) H. Hoffmann; P. R. Griffiths; F. Zaera. A RAIRS Study on the Surface Chemistry of Ethyl Iodide on Pt(111). *Surf. Sci.* **1992**, *262* (1–2), 141–150.

(32) F. Zaera. An Organometallic Guide to the Chemistry of Hydrocarbon Moieties on

Transition Metal Surfaces. *Chem. Rev.* **1995**, *95* (8), 2651–2693.

(33) B. E. Bent. Mimicking Aspects of Heterogeneous Catalysis: Generating, Isolating, and Reacting Proposed Surface Intermediates on Single Crystals in Vacuum. *Chem. Rev.* **1996**, *96* (4), 1361–1390.

(34) F. Zaera. Formation and Thermal Decomposition of Ethyl Groups on Transition Metal Surfaces: Ethyl Iodide on Pt(111). *Surf. Sci.* **1989**, *219*, 453–466.

(35) T. V. W. Janssens; F. Zaera. Chemistry of Ethylidene Moieties on Platinum Surfaces: 1,1-Diiodoethane on Pt(111). *J. Phys. Chem.* **1996**, *100* (33), 14118–14129.

(36) J. Liu; F. R. Lucci; M. Yang; S. Lee; M. D. Marcinkowski; A. J. Therrien; C. T. Williams; E. C. H. Sykes; M. Flytzani-Stephanopoulos. Tackling CO Poisoning with Single-Atom Alloy Catalysts. *J. Am. Chem. Soc.* **2016**, *138* (20), 6396–6399.

(37) M. D. Marcinkowski; M. T. Darby; J. Liu; J. M. Wimble; F. R. Lucci; S. Lee; A. Michaelides; M. Flytzani-Stephanopoulos; M. Stamatakis; E. C. H. Sykes; et al. Pt/Cu Single-Atom Alloys as Coke-Resistant Catalysts for Efficient C–H Activation. *Nat. Chem.* **2018**, No. January.

(38) M. T. Darby; E. C. H. Sykes; A. Michaelides; M. Stamatakis. Carbon Monoxide Poisoning Resistance and Structural Stability of Single Atom Alloys. *Top. Catal.* **2018**, *61* (5–6), 428–438.

(39) K. G. Papanikolaou; M. T. Darby; M. Stamatakis. Engineering the Surface Architecture of Highly Dilute Alloys: An Ab Initio Monte Carlo Approach. *ACS*

Catal. **2020**, *10* (2), 1224–1236.

(40) K. Yang; B. Yang. Surface Restructuring of Cu-Based Single-Atom Alloy Catalysts under Reaction Conditions: The Essential Role of Adsorbates. *Phys. Chem. Chem. Phys.* **2017**, *19* (27), 18010–18017.

(41) Z.-J. Zhao; L. V. Moskaleva; H. A. Aleksandrov; D. Basaran; N. Rösch. Ethylidyne Formation from Ethylene over Pt(111): A Mechanistic Study from First-Principle Calculations. *J. Phys. Chem. C* **2010**, *114* (28), 12190–12201.

(42) V. I. Avdeev; V. I. Kovalchuk; G. M. Zhidomirov; J. L. D'Itri. Ethylene Adsorption on the Pt-Cu Bimetallic Catalysts. Density Functional Theory Cluster Study. *Surf. Sci.* **2005**, *583* (1), 46–59.

(43) C. J. Jenks; B. E. Bent; F. Zaera. The Chemistry of Alkyl Iodides on Copper Surfaces. 2. Influence of Surface Structure on Reactivity. *J. Phys. Chem. B* **2000**, No. 100, 3017–3027.

(44) F. R. Lucci; M. D. Marcinkowski; T. J. Lawton; E. C. H. Sykes. H 2 Activation and Spillover on Catalytically Relevant Pt–Cu Single Atom Alloys. *J. Phys. Chem. C* **2015**, 24351–24357.

(45) J. Klimeš; D. R. Bowler; A. Michaelides. Chemical Accuracy for the van Der Waals Density Functional. *J. Phys. Condens. Matter* **2010**, *22*, 022201.

(46) J. Klimeš; D. R. Bowler; A. Michaelides. Van Der Waals Density Functionals Applied to Solids. *Phys. Rev. B - Condens. Matter Mater. Phys.* **2011**, *83* (19), 1–13.

(47) G. Kresse; J. Hafner. Ab Initio Molecular Dynamics for Liquid Metals. *Phys. Rev. B* **1993**, *47*, 558–561.

(48) G. Kresse; J. Furthmüller. Efficiency of Ab-Initio Total Energy Calculations for Metals and Semiconductors Using a Plane-Wave Basis Set. *Comput. Mater. Sci.* **1996**, *6* (1), 15–50.

(49) G. Kresse; J. Furthmüller. Efficient Iterative Schemes for Ab Initio Total-Energy Calculations Using a Plane-Wave Basis Set. *Phys. Rev. B* **1996**, *54*, 11169–11186.

(50) M. Stamatakis; D. G. Vlachos. Unraveling the Complexity of Catalytic Reactions via Kinetic Monte Carlo Simulation: Current Status and Frontiers. *ACS Catal.* **2012**, *2* (12), 2648–2663.

(51) R. Réocreux; C. Michel; P. Fleurat-Lessard; P. Sautet; S. N. Steinmann. Evaluating Thermal Corrections for Adsorption Processes at the Metal/Gas Interface. *J. Phys. Chem. C* **2019**, *123* (47), 28828–28835.

(52) M. Stamatakis; D. G. Vlachos. A Graph-Theoretical Kinetic Monte Carlo Framework for on-Lattice Chemical Kinetics. *J. Chem. Phys.* **2011**, *134* (21), 214115.

(53) J. Nielsen; M. D'Avezac; J. Hetherington; M. Stamatakis. Parallel Kinetic Monte Carlo Simulation Framework Incorporating Accurate Models of Adsorbate Lateral Interactions. *J. Chem. Phys.* **2013**, *139* (22), 224706.

Chapter 5: NiAu Single-Atom Alloys for Ethanol Dehydrogenation

This work was adapted from a submitted paper. Georgios Giannakakis performed all of the nanoparticle studies Kaining Duanmu from Phileppe Sautets' group performed the computational experiments.

5.1 Introduction

The focus of the current work, non-oxidative ethanol dehydrogenation (EDH), is of industrial interest owing to its potential to provide a route for hydrogen and acetaldehyde production[1]. Acetaldehyde is recognized as a key building block for the production of high-added value chemicals, such as acetic acid, 1-butanol, acetate esters, C-8 aromatics, and jet fuel. Alternatives have been sought to replace the inefficient industrially used oxidative process, including reactants and products over-oxidation, and challenges and costs associated with H_2O separation.[2] The non-oxidative route can ameliorate these issues, as the selectivity to the desirable acetaldehyde remains high and the main byproduct is H_2 that does not require a costly separation process[3,4]. Given the significance of the EDH reaction, the development of active, selective, and stable catalysts is an important goal.

EDH is typically performed on Cu based catalysts generally due to their activity and reactivity[5]. Au catalysts can be an appealing alternative, due to high selectivity, but suffer from generally poor activity[6,7]. This study will show that a NiAu SAA increases the activity of ethanol to acetaldehyde conversion while maintaining the beneficial selectivity of pure

Au. The practical catalyst reactor studies show this increase in activity, and the surface science experiments corroborate that larger Ni ensembles are necessary for decomposition.

5.2 Experimental

Computational details

The single-atom alloy surface was modeled by using a 3×3 unit cell. The PBE functional with dDsC dispersion correction, 400 eV cut-off energy and 7×7×1 K-points were used.[8,9] All the calculations were performed with *VASP*.[10,11] The reaction rate constant k_{TST} was calculated from the thermodynamic formulation of transition state theory (TST):

$$k_{\mathrm{TST}} = \frac{k_B \mathrm{T}}{h} \mathrm{e}^{-\frac{\Delta \mathrm{G}^{\neq}}{\mathrm{RT}}} \quad (1)$$

Where $\Delta G^{\neq}$ is the free energy difference between transition state and initial state ($G_{TS} - G_{IS}$).

Translational, rotational, and vibrational degrees of freedom were included in the free energy calculations for the gaseous species. Eq. (2) and Eq. (3) were used to obtain the free energy values for linear and non-linear gaseous molecules, respectively:

$$G = E_{DFT} + ZPE + 3.5k_BT + \sum \frac{\epsilon_i}{exp\left(\frac{\epsilon_i}{k_BT} - 1\right)} - T(S_{trans} + S_{rot} + S_{vib}) \quad (2)$$

$$G = E_{DFT} + ZPE + 4k_BT + \sum \frac{\epsilon_i}{exp\left(\frac{\epsilon_i}{k_BT} - 1\right)} - T(S_{trans} + S_{rot} + S_{vib}) \quad (3)$$

where E_{DFT} is the electronic energy given by DFT, ZPE is the zero-point energy, k_B is the Boltzmann constant, T is the temperature, ϵ_i is the harmonic energy and S is the entropy.

Surface species were assumed to have lost the translational and rotational degrees of freedom. Their free energies were hence calculated as follows:

$$G = E_{DFT} + ZPE + \sum \frac{\epsilon_i}{exp\left(\frac{\epsilon_i}{k_B T} - 1\right)} - TS_{vib} \qquad (4)$$

Single crystal studies

Temperature-programmed desorption (TPD) analysis was performed in a ultra-high vacuum chamber (base pressure <$1x10^{-10}$ mbar) using a Au(111) single crystal cleaned by cycles of sputtering Ar^+ (1.5 keV, 10 μA) followed by 720 K anneals.[12] Cleanliness was monitored *via* x-ray photoelectron spectroscopy. Ni was deposited onto the crystal held at 380 K using a physical vapor deposition source (EFM 3, Focus GmbH) at a flux of 0.04 ML/min as verified by CO titrations. The TPD traces were recorded using a heating rate of 2 K/s and the desorbing species monitored with a quadrupole mass spectrometer (HAL 301, Hiden Analytical).

Reflection absorption infrared spectroscopy (RAIRS) experiments were performed at the Center for Functional Nanomaterials (CFN) at Brookhaven National Laboratory in a UHV system with a connected preparation chamber and x-ray photoelectron spectroscopy (XPS) chamber for measurement of the Ni and cleanliness of sample. XPS data were obtained at room temperature using a SPECS PHOIBOS NAP 150 hemispherical analyzer and a monochromatic Al Kα x-ray source (1486.6 eV, ~0.25eV linewidth) focused on the sample to a spot size <300 μm (0.5 eV step, 0.1 s dwell time, 5 scans, 50 pass energy). Infrared data

were collected using a Bruker 80 V spectrometer with a polarizer and an MCT detector (2000 scans, 4 cm^{-1} resolution). The sample was placed in a UHV chamber with KBr windows and the surface set at ~8° to the beam. The RAIR spectra were taken at room temperature while the chamber was filled to 1 x 10^{-6} mbar with CO.

Catalyst synthesis

Synthesis of supported NiAu nanoparticles was achieved following a sequential reduction method as discussed previously.[13] Briefly, PVP-Au colloids were synthesized as described by Tedsree et al.[14] at a PVP:Au molar ratio of 35:1. More specifically, ~500 mg of gold precursor ($HAuCl_4$) dissolved in 10 mL ethylene glycol was added to a solution containing 50 mL ethylene glycol and 2 g of PVP (MW=58,000 g/mol). An inert gas atmosphere was obtained by flowing N_2 or He through the flask. $NaHCO_3$ was added, and the temperature was immediately increased to 90°C and held for 2 h before cooling to ambient temperature. The wine-red color of the suspension was indicative of Au NP formation. Nickel precursor ($NiCl_2$) dissolved in ethylene glycol was then added into the suspension to obtain the desired molar ratio of Ni and Au. Small amounts of hydrazine (1.6 mM) and an appropriate amount (10 μL/mL) of 1 M NaOH were added to promote Ni reduction[15] while the temperature was increased to 60°C and held for 1 h before the mixture was cooled to room temperature. The fumed silica support was first calcined in static air at 650°C for 5 h to remove organic impurities and then suspended in ethanol (1 g pre-calcined silica per 100 mL ethanol). The mixture was thoroughly mixed with 2 h of stirring and 1 h of sonication before the NiAu solution was added dropwise while the slurry remained under sonication. The resulting solution containing $NiAu/SiO_2$ was kept stirring overnight. After filtration and washing with ethanol and DI water, the final sample was dried under vacuum

overnight and calcined in air at 400°C for 5 h to remove the capping ligand (PVP) and improve the association of the metal and the support. The average particle size of these NiAu nanoparticles is 12 ± 2 nm, as has been shown previously with transmission electron microscopy. [13]

Synthesis of unsupported nanoporous NiAu samples was performed at the Lawrence Livermore National Laboratory, as described previously.[13] Briefly, a silver-gold alloy ($Ag_{70}Au_{30}$) was immersed in concentrated HNO_3 solution, which induced the leaching of silver from gold over a two-day period. Wet impregnation with nickel(II) nitrate hexahydrate solution ensured the filling of the pores with the Ni precursor, the solution was subsequently freeze dried and annealed at 500°C for 1 h under hydrogen in order to reduce the deposited Ni[16] and decompose the salt.[17]

Ambient pressure reactor studies

The ambient pressure reaction studies were performed in a fixed-bed continuous flow reactor in which the catalyst was diluted at a 1:5 ratio with pre-calcined sand and stabilized between two quartz wool plugs. The reactor was heated by a furnace equipped with a temperature controller connected to a K-type thermocouple positioned at the top of the catalyst bed. Prior to testing, all catalysts were reduced under a flow of H_2 (20% in He) with a flow rate of 10 mL/min at 400°C for 2 h to reduce NiO to metallic Ni[16,18]. The typical reaction gas composition was 2% ethanol (Sigma Aldrich, 200 proof) in He (99.999%, Airgas), achieved by feeding ethanol *via* a syringe pump into a flow of He controlled by a mass flow controller at a total flow rate of 20 mL/min unless otherwise stated. Kinetic isotope effect experiments were conducted using ethanol-OD (CH_3CH_2OD; Sigma Aldrich,

99% atom D), and ethanol-1,1-d_2 (CH_3CD_2OH; Sigma Aldrich, 98% atom D). Reactant and product concentrations were measured by gas chromatography (Agilent 7890B). A flame ionization detector was used for the detection of ethanol, acetaldehyde, and ethyl acetate, which were separated on an HP-PLOT Q capillary column. H_2, CO, and CO_2 were separated on a Carboxen-1000 packed column and detected using a thermal conductivity detector. Particular attention was paid to ensure operation away from equilibrium (~0.5% conversion) during the KIE experiments.

5.3 Results and Discussion

Significance of reactive atom dilution - Single-crystal and theoretical studies

As a first step in investigating structure-function relationships in NiAu alloys, UHV and theoretical studies of model NiAu(111) crystal surfaces were employed. Figure 5.1A shows temperature program desorption (TPD) profiles of hydrogen (m/z = 2) evolution after ethanol deposition on a NiAu(111) surface as a function of Ni coverage. At low Ni coverages (< 0.15 monolayer (ML)), two H_2 desorption peaks are observed, at 140 and 175 K. These desorption peaks are attributed to ethanol, which does not react with Au(111) under these UHV conditions (Fig. 1D) but rather desorbs below 200 K at low Ni coverages (Fig. 1B) and contributes intensity to the m/z = 2 mass spec signal. At higher Ni coverages (0.21 ML), two m/z = 2 peaks that we can attribute to H_2(g) appear at higher temperatures (280 and 356 K) and are associated with complete decomposition of ethanol. Importantly, no acetaldehyde was seen desorbing at any Ni coverage. To probe the nature of the Ni sites in the Au surface, and thus relate surface structure to chemical reactivity, CO RAIRS was performed on the

NiAu SAA and the 0.22 ML NiAu surface. The 0.22 ML NiAu surface contains Ni ensembles as evidenced by the appearance of bridge bound CO at 1911 cm^{-1}, while the 0.03 ML NiAu surface only had one IR peak corresponding to CO atop Ni atoms at 2034 cm^{-1} (Fig. 1C).[19,20] It should be noted that similar changes in the IR spectra were observed when comparing NiAu nanoparticles of varying Ni content that result in samples comprising solely Ni isolated atoms or a mixture of isolated Ni atoms and small ensembles Coupled with the TPD results, our observations reveal that under UHV conditions, single atoms of Ni in Au adsorb ethanol reversibly without activation. On the contrary, higher Ni coverages lead to the formation of small Ni ensembles which catalyze the unselective decomposition of ethanol as evidenced by the evolution of high temperature H_2 (Fig. 1D)[21,22].

This high sensitivity of the ethanol dehydrogenation reaction towards the decomposition pathway in the presence of Ni ensembles is further understood *via* DFT calculations of the acetaldehyde decomposition barrier (i.e., C-C bond cleavage) over Ni monomer, dimer, and trimer sites (Table 5.1). While the C-C bond decomposition barrier is 2.04 eV for the NiAu SAA surface (denoted as Ni_1Au in Table 5.1), a significant ~0.9 eV drop is observed for Ni dimers (Ni_2Au), and trimers (barrier of 1.16 and 0.97 eV respectively). This is consistent with the easy C-C bond cleavage which has been reported for Pt-group metals (PGM) that coordinate acetaldehyde in a η^2(C,O) conformation[23] facilitating the decomposition pathway. As a result, in the presence of even small ensembles of Ni, acetaldehyde decomposition towards CO_x, CH_4, and H_2 is observed[13]. On the other hand, isolation of the active Ni atoms in the Au lattice prevents this adsorption mode, and instead the acetaldehyde molecule is bound to the SAA surface *via* a η^1(O)-conformation (as

shown later in Fig. 3B), which leads to its reversible adsorption/desorption as observed in the TPD experiments.

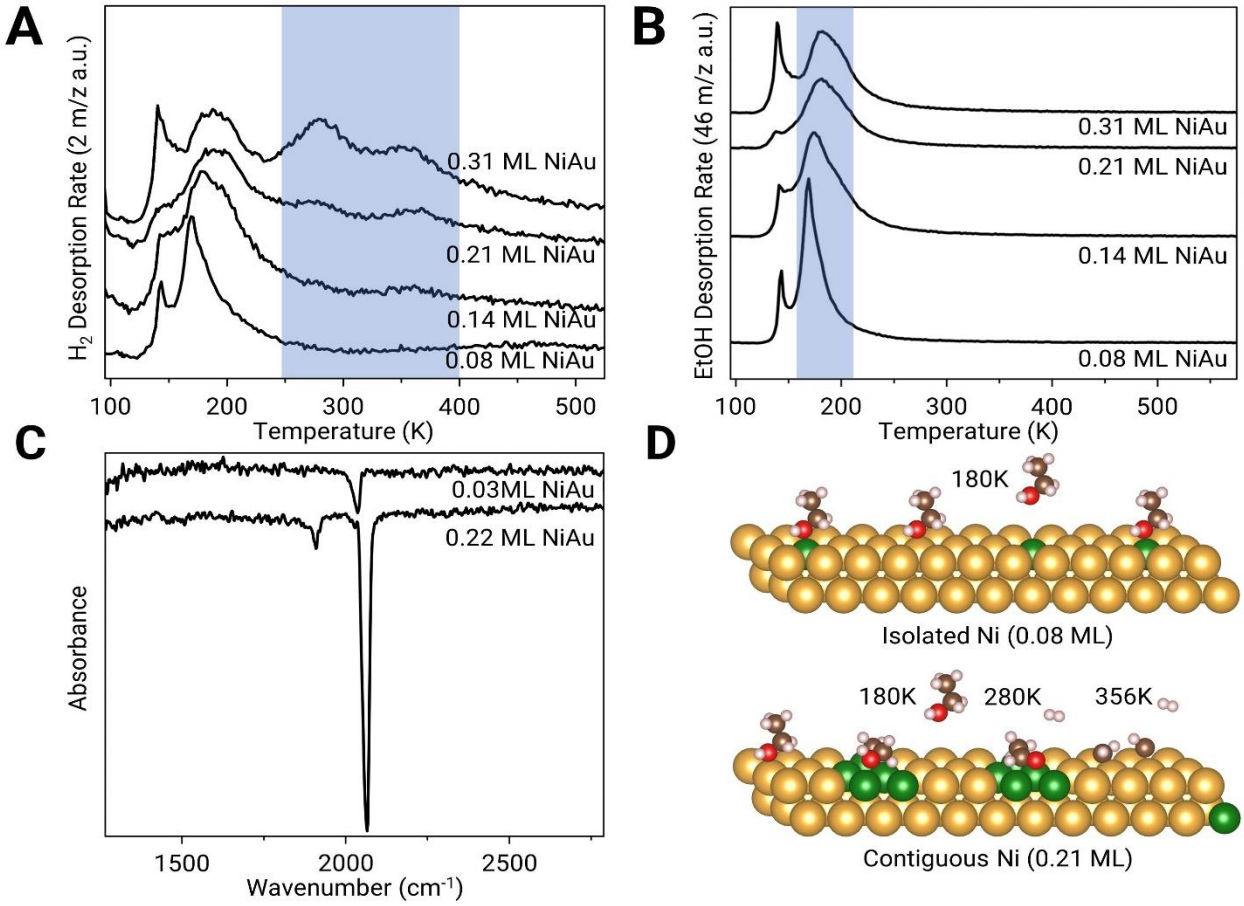

Figure 5.1. Temperature Programmed Desorption traces after ethanol exposure for **A)** H_2 (m/z = 2). The shaded rectangle highlights the temperature window over which H_2 desorption from ethanol decomposition occurs and **B)** Ethanol (m/z = 46) from NiAu(111) as a function of Ni coverage. The shaded rectangle highlights the temperature window over which the reversible desorption of ethanol occurs. **C)** CO-RAIRS of 0.03 ML and 0.22 ML Ni coverages **D)** Scheme of ethanol interaction with NiAu(111) surfaces presenting different Ni ensembles (upper: Isolated Ni atoms; lower: extended Ni surfaces)

Table 5.1. Calculated C-C bond scission barriers for Ni_x-Au(111) surfaces x=1,2,3

(111) surface	C-C bond scission, eV
Ni_1Au	2.04
Ni_2Au	1.16
Ni_3Au	0.97

Reaction Mechanism – Experimental studies

Surface science and DFT indicate that once past the ensembles of single isolated Ni atoms that C-C bond cleavage can occur. This is in good agreement with previous studies of group 10 metals in group 11[24]. It indicates that the ideal alloy for the conversion of ethanol to acetaldehyde which will only have 1 CO IR vibrational mode observed in the range of typical atop CO vibrations (2000-2100 cm^{-1}), and that once bridge bound signals below 2000 cm^{-1} are observable that ensembles exist which ultimately can lead to the undesired decomposition of ethanol.

Operando ethanol DRIFTS investigations were first employed to deduce the reaction mechanism, as has been previously performed on Ag- and Cu- based catalysts.[25,26] Comparison of the ethanol DRIFT spectra between Au/SiO_2 and $NiAu/SiO_2$ shows clear evidence for the beneficial effect of Ni atom doping on the reactivity, as acetaldehyde was found to be formed on the surface of NiAu at temperatures below 150℃ (Fig. 2B), while signs of acetaldehyde formation on Au/SiO_2 were not observed until 200℃ (Fig. 2A). Formation of acetaldehyde either bound on the surface or present in the gas phase can be

verified by the peaks observed at 1730 and 1760 cm^{-1}, respectively.[27] These results are in line with our previous reactor tests in which we compared NiAu to pure Au nanoparticle catalysts and find that Ni atoms make Au active at lower temperatures while maintaining 100% selectivity to acetaldehyde. Specifically, a considerable drop in the apparent activation energy was measured (96±5 kJ/mol for Au vs 61±2 kJ/mol for NiAu), while NiAu catalysts demonstrated 100% selectivity at 27% conversion at 250℃ for more than 50 hours on stream.[13] Unfortunately, DRIFTS studies were inconclusive towards determining the reaction mechanism for the supported NiAu/SiO_2 catalysts of this study, as spectator ethoxy species adsorbed on the silica interfere with interpretation of the intermediates.

In KIE studies of silica supported Au NPs and NiAu SAAs, the catalytic activity of non-deuterated ethanol was compared to isotopically labeled ethanol, deuterated in either the α C-H or O-H position. First, the activity of non-deuterated ethanol over an Au/SiO_2 catalyst was followed under steady state at 220℃ at conditions away from equilibrium. The acetaldehyde formation rate was measured as 8.7 μmol/mol_{Au}·s (Fig 2C). Following that, deuterated ethanol (CH_3CD_2OH) was introduced to the flow reactor and a two-fold decrease in catalytic activity was observed. Experiments over silica supported NiAu SAAs conducted at 150℃ (Fig. 2D) showed a similar drop in the reactivity (k_H/k_D= 1.9), signifying the presence of a KIE linked with the C-H bond cleavage elementary step.[28–30] This is in line with the existing literature on alcohol activation over various bimetallic systems.[26] However, further investigation on the role of the O-H dissociation step in the reaction mechanism is required. To that end, deuterated ethanol was used, where the hydrogen atom in the O-H is replaced by a deuterium atom (CH_3CH_2OD). A drop in reactivity is observed for both NiAu SAAs and Au NPs (~ 1.5 in both cases, Fig, 2C, D) when switching between the regular

(OH) and deuterated (OD) ethanol in the feed, indicating that the O-H bond cleavage step also plays a kinetically relevant role in the reaction mechanism. This is also consistent with previous work in which the kinetic significance of both C-H and O-H bond scission steps has been discussed for the non-oxidative activation of ethanol and 2-octanol over Cu and Ni catalysts supported on acidic or basic supports.[31,32]

Related to these results, Suskevich et al. obtained similar data from their spectroscopic and isotopic experiments for the EDH reaction over Ag/SiO_2 catalysts (k_H/k_D=1.9 and 1.8 for C-H and O-H respectively).[25] Their analysis suggested the existence of a concerted mechanism in which O-H activation takes place on the support and C-H activation occurs on the Ag surface, and they concluded that the two sites must be in close proximity. As mentioned above, ethoxy species formed on the support are in fact spectator species in the reaction and do not react further. However, while there is a possibility for a concerted, two-site mechanism over supported monometallic Au, it is unlikely that this mechanism also holds for the case of NiAu SAAs. First, migration of the ethoxy species from the support to NiAu domains is unlikely and second, as the Ni atoms are present in very low concentration, it is not expected that sufficient exist in close enough proximity to SiO_2 to activate ethanol. However, while this analysis is challenging for supported NiAu SAA nanoparticles we also studied unsupported nanoporous NiAu SAAs in order to deconvolute the role of the SAA from that of the support. Our KIE investigations of the unsupported catalysts yielded similar values (Fig. S4) to the supported catalysts (k_H/k_D=1.7 and 1.5 for C-H and O-H respectively), suggesting that the reaction mechanism is the same in both silica supported and unsupported nanoporous catalysts. This claim can be further supported by the similar apparent activation energy measured on nanoporous (np-) NiAu and $NiAu/SiO_2$, as shown previously.[13] These

results allow us to rule out that the aforementioned concerted EDH reaction, involving sites on both the support and the NiAu SAA nanoparticles, is the primary mechanism.

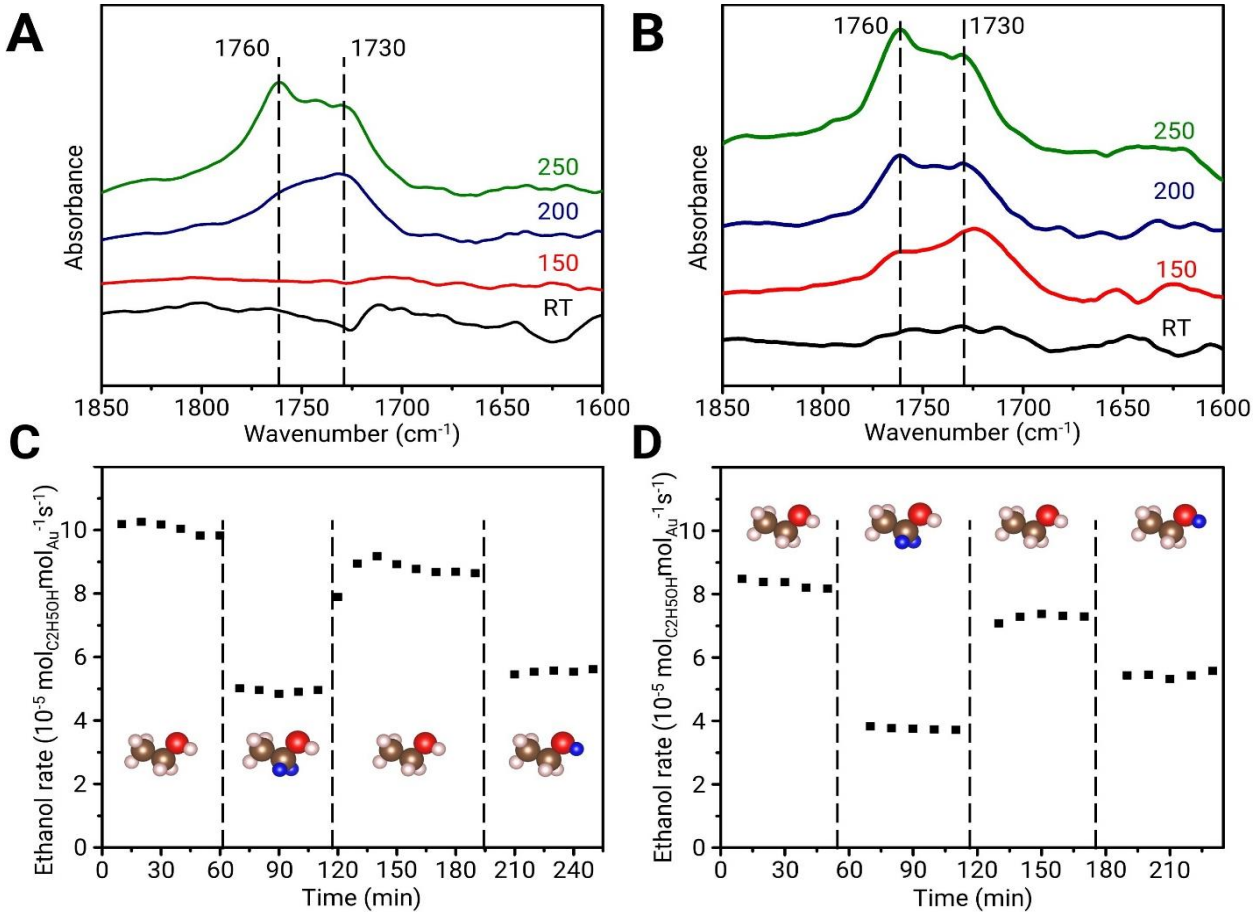

Figure 5.2. Ethanol DRIFTS using **A)** Au/SiO_2 and **B)** $Ni_{0.005}Au/SiO_2$ focusing on the C-O regime (1850-1600 cm^{-1}). KIE studies using **C)** Au/SiO_2 (2 kPa EtOH in He, 10 cc/min, 150 mg catalyst, 220℃), ethanol injected: i) pure ethanol, ii) CH_3CH_2OD, iii) pure ethanol, iv) CH_3CD_2OH and **D)** $NiAu/SiO_2$ (2 kPa EtOH in He, 20c c/min, 150 mg catalyst, 180 ℃), ethanol injected: i) pure ethanol ii) CH_3CD_2OH, iii) pure ethanol iv) CH_3CH_2OD

Reaction mechanism - Theoretical studies

The KIE results provide insights into the kinetic significance of the C-H and O-H cleavage steps, and we further this understanding through DFT simulations of the reaction mechanism. H_2 partial pressures equal to those measured at the reactor outlet (0.0003 bar) at the temperature examined in kinetic tests (150°C) were used for the calculations and the pressure of aldehyde was set to the same value for stoichiometric reasons. The internal adsorption energy of ethanol on Ni is significant (-0.66 eV), but at high temperature and low pressure, the entropy of gas phase ethanol is large, which makes the initial adsorption state endergonic. The free energy profile for the dehydrogenation of CH_3CH_2OH on a NiAu(111) SAA surface is shown in Figure 5.3A, and two possible reaction pathways are calculated: α C-H dissociation followed by O-H dissociation (blue pathway) and O-H dissociation followed by α C-H dissociation (red pathway), as shown in Fig. 3B. After the first dehydrogenation step (TS1), the dehydrogenated H atoms are able to desorb from the alloy surface (IM1 to IM2) because the gas phase H_2 is thermodynamically more stable than surface bound H and the barriers for the translation and recombination of H atoms and desorption of H_2 from the alloy surface are quite low. Based on the overall barriers, it is evident that the pathway initiated by the C-H dissociation (blue) is the more favorable one. While there is a general consensus in literature studies of supported catalysts that O-H bond activation is the first step, followed by C-H bond scission, here we observe a different pathway in line with DFT and microkinetic modelling studies of EDH on Pd(111) and Pt(111).[33,34] This reaction pathway was also suggested for unsupported NiCu alloys[35], however on pure Ni(111), O-H activation has been identified as the first step.[22]

On the blue pathway, the effective free energy activation barrier, also called energetic span,[36] is between the initial gas state of ethanol (0 eV) and the OH bond cleavage transition state (TS2, 1.17 eV). This effective free energy barrier, which controls the rate of the dehydrogenation reaction, can be viewed as the sum of the reaction free energy of the first C-H cleavage step, from gas phase to the IM2 intermediate, and the free energy barrier of the second O-H cleavage step. The corresponding enthalpy barrier is 0.73 eV, in good agreement with the experimental value (0.59 eV).

Our DFT simulation of the EDH reaction on Au(111) (Fig. S10) shows that the first dehydrogenation step (TS1) is the rate determining step and the blue reaction pathway still has a lower overall barrier (1.84 eV) than the red reaction pathway (2.05 eV), which means that the reaction is very slow, as opposed to NiAu(111) SAA, and the optimal reaction pathway occurs *via* α C-H dissociation followed by O-H dissociation on Au. The DFT calculations also demonstrate that the reaction barriers for EDH are much higher on pure Au (Fig. S11) than on NiAu SAA (enthalpic barrier of 0.94 eV for Au vs. 0.73 eV for NiAu), in qualitative agreement with experimental enthalpy barriers (0.96 eV vs 0.59 eV).[13] Most importantly, the NiAu SAA does not over bind ethanol, as is the case for pure Ni, and therefore regardless of whether the O-H or C-H bond is broken first, the reaction mechanisms on the SAA are selective to the preferred acetaldehyde and hydrogen products.

Selective poisoning supports the Ni atom active site model – single crystal and reactor studies

Our combined spectroscopic, kinetic, and theoretical investigations have shed light on the preferred EDH reaction pathways on both Au and NiAu SAAs. We also demonstrated

with DFT (Fig. 3A) that both kinetically relevant reaction steps (C-H and O-H cleavage) take place over the Ni atom, pointing at isolated Ni atom sites in Au being the active site of the catalyst. Related to this, it is noteworthy that active site identification on the same SAA catalyst in oxidative coupling reactions show $[Au\text{-}O_x]^-$ species as the active site.[37] Therefore, to further solidify our hypothesis that individual, isolated Ni atoms are the active sites for the non-oxidative EDH reaction, reactor tests with a poison that selectively blocks only the Ni sites were employed. Specifically, CO is known to bind strongly to group 10 metals but not to coinage metals. DFT calculations by Darby et al. put the CO desorption temperature from the NiAu (111) SAA surface at 340 K.[38] In contrast, DFT and experimental measurements indicate that CO desorbs from Au(111) below 100 K.[39] CO TPD from single crystal NiAu(111) surfaces of various Ni coverages were studied under UHV (Fig. 3C). Desorption of CO from low concentrations of Ni was observed at 325 K, in close agreement with the theoretical calculations. For Ni coverages >0.2 ML a secondary desorption feature at lower temperature is observed in the CO TPD spectra (highlighted in red in Fig. 3C), consistent with the formation of Ni aggregate/Au interfaces.[12] Comparing the desorption temperature of CO and ethanol (Fig. 1B), it is clear that desorption of CO takes place at considerably higher temperatures than ethanol (325 vs 190 K), indicating that CO should outcompete ethanol for binding to the Ni atom sites.[40,41] Guided by these surface science and theoretical results, ambient pressure reactor tests were performed on supported NiAu SAAs where the Ni site was poisoned with CO (Fig 3D). First, ethanol was introduced into the reactor and the ethanol consumption rate measured, followed by co-flowing carbon monoxide and ethanol through the reactor. A considerable drop (~70%) in the catalytic activity was noticed in the presence of CO, due to the CO binding to Ni more strongly than

ethanol essentially poisoning Ni sites, as was predicted from the surface science results. As a result, the only active sites available to ethanol are Au sites. Importantly, the ~4-fold lower ethanol consumption rate on CO-poisoned NiAu SAAs matches the ethanol consumption rate on pure Au NPs at those conditions (Fig. 2D). This provides definitive evidence that the isolated Ni atom sites are involved in the active site for the EDH reaction. Furthermore, once the flow of CO is halted, the NiAu SAA catalyst activity returns to previously measured levels, consistent with the reversible adsorption/desorption of CO observed in the single crystal measurements.

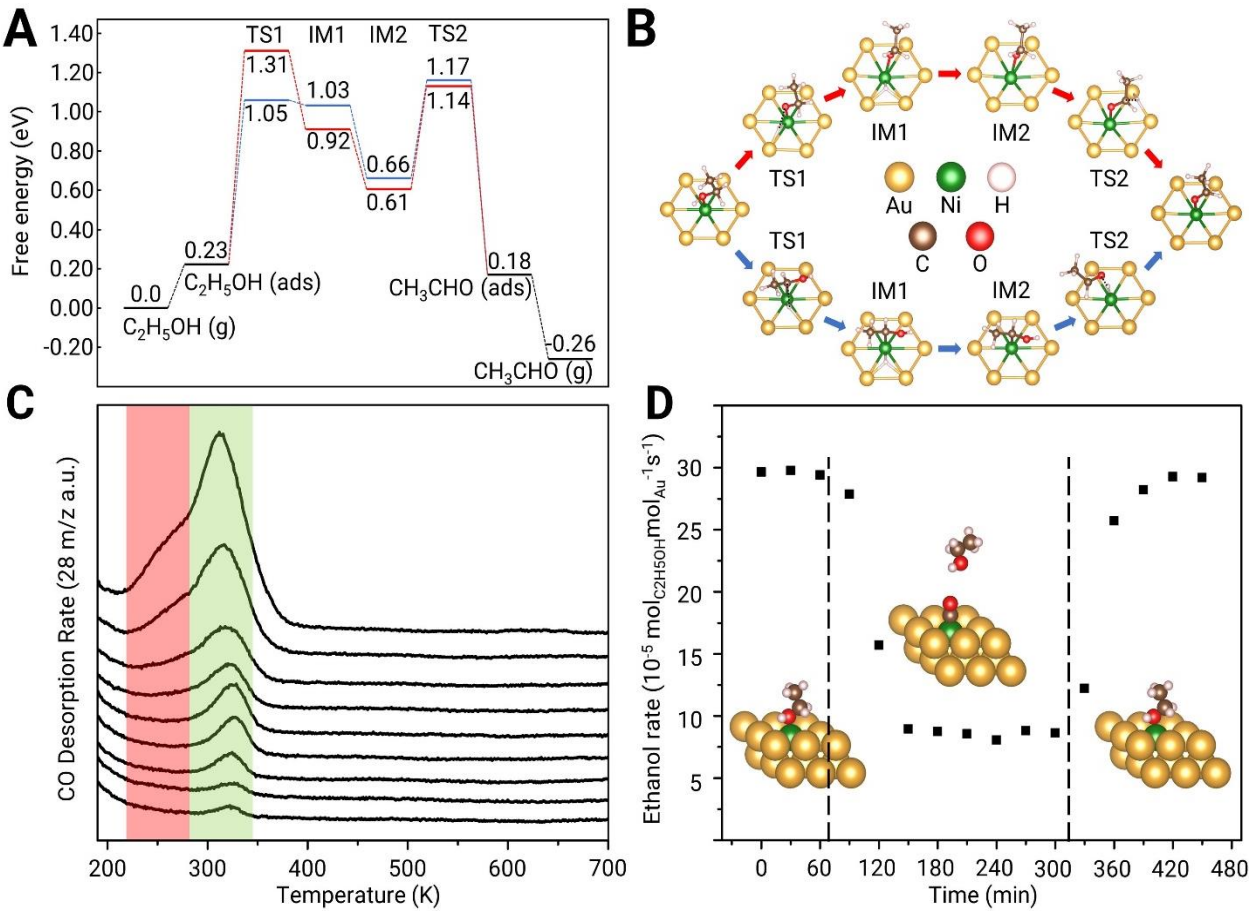

Figure 5.3. A) Free energy diagram of ethanol dehydrogenation on the NiAu(111) SAA surface. The conditions used for the construction are: $P(H_2)$ = 0.0003bar, $P(C_2H_5OH)$ = 0.02

bar, P(CH_3CHO) = 0.0003bar, and T = 423.15K. **B)** Adsorption configurations, visualized using VESTA.[42] **C)** Temperature Programmed Desorption profile for CO desorption from NiAu(111) at various Ni coverages (0.01 ML to 0.61 ML). **D)** Ethanol dehydrogenation tests at 473 K under i) 2kPa ethanol, ii) 2kPa ethanol & 2kPa CO and iii) 2kPa ethanol balanced in He.

To further support the claims about the effect of CO on reactivity, DFT simulations in which a CO molecule was bound to the Ni atom were performed and the reaction pathway computed Expectedly, the energetics of the pathway match that of the bare Au(111) surface, and only the Au atoms neighboring the Ni atom exhibit very small shift in their d-band center. It should be noted however that according to our DFT results, the ethanol molecule binds more favorably to the next available Au atom, possibly due to steric repulsion from the CO molecule. The above theoretical results, when coupled with the reactor tests that were guided by the single crystal experiments, constitute solid evidence that the individual, isolated Ni atoms are the active sites for the EDH reaction.

Taken together, the combined theoretical, single-crystal, and nanoparticles studies were critical in obtaining a deep understanding of the NiAu SAA system and showcasing how it can be used for the design of new catalysts. The single-crystal and theoretical studies are in full agreement with previous NiAu/SiO_2 SAA CO IR data[13] in terms of the importance of maintaining very high levels of dilution, such that the Ni atoms are always isolated from one another in the host matrix. This result demonstrates how ethanol can be used as a probe molecule for the characterization of active site ensemble sizes in bimetallic catalytic

surfaces. Alloy particles with high dispersion of the reactive metal atoms should only yield acetaldehyde and hydrogen under EDH reaction conditions. On the contrary, evidence of undesirable product formation from the decomposition pathway indicates formation of reactive metal aggregates in the surface of the inert host. Similar experimental and theoretical reports for NiCu and PdAu dilute alloys bolster this argument.[43–45] Therefore, the EDH reaction has the potential to serve as a probe reaction for the surface characterization of dilute alloys and complement other characterization techniques as is the case for ethylene hydrogenation which has been shown to be a probe of the metallic surface area of Pt-based catalysts.[46]

Furthermore, the three-pronged approach was shown to be capable of outlining the reaction mechanism and identifying the active sites for the reaction. This is especially highlighted by the KIE studies, supported by DFT calculations, as well as the active site identification by controlled poisoning of the Ni sites. These examples underline the powerful complementary nature of single atom alloys, which allows for their accurate modelling towards understanding their properties and designing new catalysts based on theoretical insights.[47] Furthermore, SAA catalysts can be promising candidates for facilitating industrially the non-oxidative ethanol dehydrogenation process, as they combine high reactivity, while maintaining the host-like selectivity (~100%).

5.4 Conclusions

Here we have used surface science, practical catalysis, and theory to characterize the active sites and reaction mechanism of a NiAu SAA for ethanol dehydrogenation. Isolated

Ni atoms were shown in nanoparticle studies to be active and 100% selective for low temperature conversion of ethanol to acetaldehyde and hydrogen. KIE experiments were performed that showed C-H cleavage followed by O-H bond cleavage which was in good agreement with theory. Surface science experiments elucidated that isolated Ni atoms in the surface are unable to decompose ethanol into undesirable side products, but that larger ensembles were capable of unselective decomposition. This was also observed in the nanoparticle studies. CO was shown in surface science experiments to bind strongly to Ni sites, and under practical catalytic conditions it was shown that CO was able to inhibit the conversion of ethanol to acetaldehyde to the same levels of pure Au. It is beneficial to show that it was possible to increase the more efficient non-oxidative conversion of ethanol to acetaldehyde as the industrial process is done oxidatively and thus necessitates the extraction of water from the acetaldehyde which is costly.

5.5 References

(1) Sun, J.; Wang, Y. Recent Advances in Catalytic Conversion of Ethanol to Chemicals. *ACS Catal.* **2014**, *4* (4), 1078–1090. https://doi.org/10.1021/cs4011343.

(2) Mitsudome, T.; Mikami, Y.; Funai, H.; Mizugaki, T.; Jitsukawa, K.; Kaneda, K. Oxidant-Free Alcohol Dehydrogenation Using a Reusable Hydrotalcite-Supported Silver Nanoparticle Catalyst. *Angew. Chemie* **2008**, *120* (1), 144–147. https://doi.org/10.1002/ange.200703161.

(3) Eagan, N. M.; Kumbhalkar, M. D.; Buchanan, J. S.; Dumesic, J. A.; Huber, G. W.

Chemistries and Processes for the Conversion of Ethanol into Middle-Distillate Fuels. *Nat. Rev. Chem.* **2019**, *3* (4), 223–249. https://doi.org/10.1038/s41570-019-0084-4.

(4) Eckert, M.; Fleischmann, G.; Jira, R.; Bolt, H. M.; Golka, K. Acetaldehyde. In *Ullmann's Encyclopedia of Industrial Chemistry*; 2011. https://doi.org/10.1002/14356007.a01.

(5) Tu, Y.; Chen, Y. Effects of Alkaline-Earth Oxide Additives on Silica-Supported Copper Catalysts in Ethanol Dehydrogenation. **1998**, *5885* (1), 2618–2622.

(6) Guan, Y.; Hensen, E. J. M. Ethanol Dehydrogenation by Gold Catalysts: The Effect of the Gold Particle Size and the Presence of Oxygen. *Appl. Catal. A Gen.* **2009**, *361* (1–2), 49–56. https://doi.org/10.1016/j.apcata.2009.03.033.

(7) Gazsi, A.; Koós, A.; Bánsági, T.; Solymosi, F. Adsorption and Decomposition of Ethanol on Supported Au Catalysts. *Catal. Today* **2011**, *160* (1), 70–78. https://doi.org/10.1016/j.cattod.2010.05.007.

(8) Steinmann, S. N.; Corminboeuf, C. Comprehensive Benchmarking of a Density-Dependent Dispersion Correction. *J. Chem. Theory Comput.* **2011**, *7* (11), 3567–3577. https://doi.org/10.1021/ct200602x.

(9) Perdew, J. P.; Burke, K.; Ernzerhof, M. Generalized Gradient Approximation Made Simple. *Phys. Rev. Lett.* **1996**, *77* (18), 3865–3868. https://doi.org/10.1103/PhysRevLett.77.3865.

(10) Kresse, G.; Hafner, J. Ab Initio Molecular-Dynamics Simulation of the Liquid-

Metalamorphous- Semiconductor Transition in Germanium. *Phys. Rev. B* **1994**, *49* (20), 14251–14269. https://doi.org/10.1103/PhysRevB.49.14251.

(11) Kresse, G.; Hafner, J. Ab Initio Molecular Dynamics for Liquid Metals. *Phys. Rev. B* **1993**, *47*, 558–561. https://doi.org/10.1103/PhysRevB.47.558.

(12) Wang, Z.-T.; Darby, M. T.; Therrien, A. J.; El-Soda, M.; Michaelides, A.; Stamatakis, M.; Sykes, E. C. H. Preparation, Structure, and Surface Chemistry of Ni–Au Single Atom Alloys. *J. Phys. Chem. C* **2016**, *120* (25), 13574–13580. https://doi.org/10.1021/acs.jpcc.6b03473.

(13) Giannakakis, G.; Trimpalis, A.; Shan, J.; Qi, Z.; Cao, S.; Liu, J.; Ye, J. NiAu Single Atom Alloys for the Non-Oxidative Dehydrogenation of Ethanol to Acetaldehyde and Hydrogen. *Top. Catal.* **2018**, *61* (5), 475–486. https://doi.org/10.1007/s11244-017-0883-0.

(14) Tedsree, K.; Li, T.; Jones, S.; Chan, C. W. A.; Yu, K. M. K.; Bagot, P. A. J.; Marquis, E. A.; Smith, G. D. W.; Tsang, S. C. E. Hydrogen Production from Formic Acid Decomposition at Room Temperature Using a Ag–Pd Core–Shell Nanocatalyst. *Nat. Nanotechnol.* **2011**, *6* (5), 302–307. https://doi.org/10.1038/nnano.2011.42.

(15) Wu, S. H.; Chen, D. H. Synthesis and Characterization of Nickel Nanoparticles by Hydrazine Reduction in Ethylene Glycol. *J. Colloid Interface Sci.* **2003**, *259* (2), 282–286. https://doi.org/10.1016/S0021-9797(02)00135-2.

(16) Rodriguez, J. A.; Hanson, J. C.; Frenkel, A. I.; Kim, J. Y.; Pérez, M. Experimental

and Theoretical Studies on the Reaction of H_2 with NiO: Role of O Vacancies and Mechanism for Oxide Reduction. *J. Am. Chem. Soc.* **2002**, *124* (2), 346–354. https://doi.org/10.1021/ja0121080.

(17) Elmasry, M. A. A.; Gaber, A.; Khater, E. M. H. Thermal Decomposition of Ni(II) and Fe(III) Nitrates and Their Mixture. *Journal of Thermal Analysis and Calorimetry*. 1998, pp 489–495. https://doi.org/10.1023/A:1010155203247.

(18) Ma, L.; Jia, I.; Guo, X.; Xiang, L. High Performance of Pd Catalysts on Bimodal Mesopore for the Silica Catalytic Oxidation of Toluene. *Chinese J. Catal.* **2014**, *35* (0), 108–119. https://doi.org/10.1016/S1872.

(19) Xu, C.; Koel, B. E. Influence of Alloyed Sn Atoms on the Chemisorption Properties of Ni(111) as Probed by RAIRS and TPD Studies of CO Adsorption. *Surf. Sci.* **1995**, *327* (1–2), 38–46. https://doi.org/10.1016/0039-6028(94)00816-7.

(20) Vasquez, N.; Muscat, A.; Madix, R. J. The Effect of Site Distribution on Desorption Kinetics: Carbon Monoxide from Ni(100). *Surf. Sci.* **1994**, *301* (1–3), 83–88. https://doi.org/10.1016/0039-6028(94)91289-0.

(21) Kratochwil, T.; Wittmann, M.; Küppers, J. Adsorption of Ethanol on Ni(100) Surfaces. *J. Electron Spectros. Relat. Phenomena* **1993**, *64–65* (C), 609–617. https://doi.org/10.1016/0368-2048(93)80128-9.

(22) Gates, S. M.; Russell, J. N.; Yates, J. T. Bond Activation Sequence Observed in the Chemisorption and Surface Reaction of Ethanol on Ni(111). *Surf. Sci.* **1986**, *171* (1), 111–134. https://doi.org/10.1016/0039-6028(86)90565-0.

(23) Mavrikakis, M.; Barteau, M. A. Oxygenate Reaction Pathways on Transition Metal Surfaces. *J. Mol. Catal. A Chem.* **1998**, *131* (1–3), 135–147. https://doi.org/10.1016/S1381-1169(97)00261-6.

(24) Chen, M.; Kumar, D.; Yi, C. W.; Goodman, D. W. The Promotional Effect of Gold in Catalysis by Palladium-Gold. *Science (80-.).* **2005**, *310* (5746), 291–293. https://doi.org/10.1126/science.1115800.

(25) Sushkevich, V. L.; Ivanova, I. I.; Taarning, E. Mechanistic Study of Ethanol Dehydrogenation over Silica-Supported Silver. *ChemCatChem* **2013**, *5* (8), 2367–2373. https://doi.org/10.1002/cctc.201300033.

(26) Shan, J.; Liu, J.; Li, M.; Lustig, S.; Lee, S.; Flytzani-Stephanopoulos, M. NiCu Single Atom Alloys Catalyze the C H Bond Activation in the Selective Non-Oxidative Ethanol Dehydrogenation Reaction. *Appl. Catal. B Environ.* **2017**. https://doi.org/10.1016/j.apcatb.2017.12.059.

(27) Demri, D.; Hindermann, J.; Diagne, C.; Kiennemann, A. Oxygenates on Rhodium-Containing Catalysts during CO + H_2 Reactions. *J. Chem. Soc. - Faraday Trans.* **1994**, *90* (3), 501–506.

(28) Campbell, C. T. Finding the Rate-Determining Step in a Mechanism: Comparing DeDonder Relations with the "Degree of Rate Control." *J. Catal.* **2001**, *204* (2), 520–524. https://doi.org/10.1006/jcat.2001.3396.

(29) Campbell, C. T. Future Directions and Industrial Perspectives Micro- and Macro-Kinetics: Their Relationship in Heterogeneous Catalysis. *Top. Catal.* **1994**, *1* (3–4),

353–366. https://doi.org/10.1007/BF01492288.

(30) Chen, K.; Iglesia, E.; Bell, A. T. Kinetic Isotopic Effects in Oxidative Dehydrogenation of Propane on Vanadium Oxide Catalysts. *J. Catal.* **2000**, *192* (1), 197–203. https://doi.org/10.1006/jcat.2000.2832.

(31) Chen, H.; He, S.; Xu, M.; Wei, M.; Evans, D. G.; Duan, X. Promoted Synergic Catalysis between Metal Ni and Acid-Base Sites toward Oxidant-Free Dehydrogenation of Alcohols. *ACS Catal.* **2017**, *7* (4), 2735–2743. https://doi.org/10.1021/acscatal.6b03494.

(32) Hanukovich, S.; Dang, A.; Christopher, P. Influence of Metal Oxide Support Acid Sites on Cu-Catalyzed Nonoxidative Dehydrogenation of Ethanol to Acetaldehyde. *ACS Catal.* **2019**, *9* (4), 3537–3550. https://doi.org/10.1021/acscatal.8b05075.

(33) Li, M.; Guo, W.; Jiangs, R.; Zhao, L.; Shan, H. Decomposition of Ethanol on Pd(111): A Density Functional Theory Stutdy. *Langmuir* **2010**, *26* (3), 1879–1888. https://doi.org/10.1021/la902641t.

(34) Sutton, J. E.; Panagiotopoulou, P.; Verykios, X. E.; Vlachos, D. G. Combined DFT, Microkinetic, and Experimental Study of Ethanol Steam Reforming on Pt. *J. Phys. Chem. C* **2013**, *117* (9), 4691–4706. https://doi.org/10.1021/jp312593u.

(35) Kumar, A.; Ashok, A.; Bhosale, R. R.; Saleh, M. A. H.; Almomani, F. A.; Al-Marri, M.; Khader, M. M.; Tarlochan, F. In Situ DRIFTS Studies on Cu, Ni and CuNi Catalysts for Ethanol Decomposition Reaction. *Catal. Letters* **2016**, *146* (4), 778–787. https://doi.org/10.1007/s10562-016-1706-9.

(36) Kozuch, S.; Shaik, S. How to Conceptualize Catalytic Cycles? The Energetic Span Model. *Acc. Chem. Res.* **2011**, *44* (2), 101–110. https://doi.org/10.1021/ar1000956.

(37) Trimpalis, A.; Giannakakis, G.; Cao, S.; Flytzani-Stephanopoulos, M. NiAu Single Atom Alloys for the Selective Oxidation of Methacrolein with Methanol to Methyl Methacrylate. *Catal. Today* **2020**, *355* (April), 804–814. https://doi.org/10.1016/j.cattod.2019.04.021.

(38) Darby, M. T.; Sykes, E. C. H.; Michaelides, A.; Stamatakis, M. Carbon Monoxide Poisoning Resistance and Structural Stability of Single Atom Alloys. *Top. Catal.* **2018**, *61* (5–6), 428–438. https://doi.org/10.1007/s11244-017-0882-1.

(39) Outka, D. A.; Madix, R. J. The Oxidation of Carbon Monoxide on the Au(110) Surface. *Surf. Sci.* **1987**, *179* (2–3), 351–360. https://doi.org/10.1016/0039-6028(87)90062-8.

(40) Marcinkowski, M. D.; Jewell, A. D.; Stamatakis, M.; Boucher, M. B.; Lewis, E. A.; Murphy, C. J.; Kyriakou, G.; Sykes, E. C. H. Controlling a Spillover Pathway with the Molecular Cork Effect. *Nat. Mater.* **2013**, *12* (6), 523–528. https://doi.org/10.1038/nmat3620.

(41) Lucci, F. R.; Darby, M. T.; Mattera, M. F. G.; Ivimey, C. J.; Therrien, A. J.; Michaelides, A.; Stamatakis, M.; Sykes, E. C. H. Controlling Hydrogen Activation, Spillover, and Desorption with Pd-Au Single-Atom Alloys. *J. Phys. Chem. Lett.* **2016**, *7* (3), 480–485. https://doi.org/10.1021/acs.jpclett.5b02400.

(42) Momma, K.; Izumi, F. VESTA 3 for Three-Dimensional Visualization of Crystal,

Volumetric and Morphology Data. *J. Appl. Crystallogr.* **2011**, *44* (6), 1272–1276. https://doi.org/10.1107/S0021889811038970.

(43) Shan, J.; Janvelyan, N.; Li, H.; Liu, J.; Egle, T. M.; Ye, J.; Biener, M. M.; Biener, J.; Friend, C. M.; Flytzani-Stephanopoulos, M. Selective Non-Oxidative Dehydrogenation of Ethanol to Acetaldehyde and Hydrogen on Highly Dilute NiCu Alloys. *Appl. Catal. B Environ.* **2017**, *205*, 541–550. https://doi.org/10.1016/j.apcatb.2016.12.045.

(44) Ouyang, M.; Papanikolaou, K. G.; Boubnov, A.; Hoffman, A. S.; Giannakakis, G.; Bare, S. R.; Stamatakis, M.; Flytzani-Stephanopoulos, M.; Sykes, E. C. H. Directing Reaction Pathways via in Situ Control of Active Site Geometries in PdAu Single-Atom Alloy Catalysts. *Nat. Commun.* **2021**, *12* (1), 1–11. https://doi.org/10.1038/s41467-021-21555-z.

(45) Li, H.; Evans, E. J.; Mullins, C. B.; Henkelman, G. Ethanol Decomposition on Pd-Au Alloy Catalysts. *J. Phys. Chem. C* **2018**, *122* (38), 22024–22032. https://doi.org/10.1021/acs.jpcc.8b08150.

(46) Kuhn, J. N.; Tsung, C. K.; Huang, W.; Somorjai, G. A. Effect of Organic Capping Layers over Monodisperse Platinum Nanoparticles upon Activity for Ethylene Hydrogenation and Carbon Monoxide Oxidation. *J. Catal.* **2009**, *265* (2), 209–215. https://doi.org/10.1016/j.jcat.2009.05.001.

(47) Hannagan, R. T.; Giannakakis, G.; Réocreux, R.; Schumann, J.; Finzel, J.; Wang, Y.; Michaelides, A.; Deshlahra, P.; Christopher, P.; Flytzani-Stephanopoulos, M.; Stamatakis, M.; Sykes, E. C. H. First-Principles Design of a Single-Atom–Alloy

Propane Dehydrogenation Catalyst. *Science*.. **2021**, *372* (6549), 1444–1447.

Chapter 6: High-Pressure RAIRS investigations of Single-Atom Alloys

6.1 Introduction

Monometallic catalysts can be beneficial for many reactions, but sometimes they are not optimal. Bimetallic catalysts often exhibit superior performance to their monometallic counterparts and are the active nanoparticles in many industrial reactions[1–5]. While the activity of bimetallic catalysts is empirically known, understanding the active sites on the surface of a bimetallic catalyst in-situ is a challenge. This is due to several competing factors, all related to structural complexity. One factor is surface free energy, wherein one of the bimetallic elements is more thermodynamically stable at the surface[6]. This effect causes one metal to preferentially reside on the bimetallic nanoparticle surface when the catalyst is heated to a sufficient temperature in the absence of adsorbates. In the presence of adsorbates this preference can change: if one metal has a strong binding strength to an adsorbate this interaction can overcome the difference in the surface free energy and cause that metal to remain in the surface layer at a temperature where it would otherwise not be stable at the surface[7–9]. The interplay between adsorbate binding strength and surface free energy is not well characterized in bimetallic catalysts. It is common for groups to study bimetallic catalysts under conditions were the bimetallic catalysts switch oxidation states such as CO oxidation, or NO oxidation/reduction[10–12]. One challenge in studying oxidation reactions is that the surface free energies for purely metallic and oxidized systems are different, and oftentimes the preference for one metal to remain in the surface over another in an oxidized state is the opposite of the metallic state[6]. Thus, studying these reactions under conditions where the bimetallic system remains metallic or oxidized is vital in understanding the role of adsorbate binding energy in overcoming the thermodynamic driving force of the surface free energies of the pure metals.

Single-atom alloys are well positioned as a system for studying the effects of adsorbate binding on surface structure because they are bimetallic systems exhibiting well-defined structures with minimized complexity. For all single-atom alloys, where one group 10 or 9 element is substituted into a group 11 metal host[13], the surface free energy thermodynamics favor the group 11 element at the surface at high temperatures due to their lower surface free energies. However, many molecules such as CO have a stronger interaction with the group 10 or 9 metal dopant atom than the group 11 metal host and CO exposure results in the group 10 or 9 metal remaining at the surface of the catalyst at temperatures where it otherwise would not. This makes single-atom alloys ideal systems to understand the delicate interplay between binding strength and surface free energy.

UHV conditions are commonly used to probe the structure-activity relationships of catalytically relevant single crystal surfaces. This allows the experiment to be conducted with a high degree of focus on specific atomic interactions void of many other variables present in more complex environments such as those at atmospheric pressures. However, in UHV conditions the surface is not always in the same state that it exists during reaction because adsorbates such as CO at higher pressures are known to change the atomistic structure and therefore UHV studies are not always representative of industrial reactive conditions[10,11,14]. To better understand the effect CO has on alloys and its ability to cause changes in the metal-metal bonds that dictate surface structure we need to go beyond UHV studies and examine systems at elevated pressures.

One approach that has been used to do this is coupling UHV surface science techniques with high pressure cells for x-ray photoelectron spectroscopy (XPS) and reflection adsorption infrared spectroscopy (RAIRS). These instruments can probe changes in the surface structure of alloys as a function of CO pressure and temperature.

These tools allow for a better and dynamic understanding of the active sites of catalytic materials in a variety of environments that more closely resemble the conditions of industrial catalysis. In this study several NiAu and PdAu dilute alloys were prepared and their change in structure with respect to CO and temperature was examined using polarization dependent reflection adsorption infrared spectroscopy (PD-RAIRS).

NiAu SAAs have been shown to be active for the selective cross coupling reaction of methacrolein and methanol[15], C-C coupling[16] and dehydrogenation of ethanol[8,17]. Sykes et al. have studied PdAu SAAs and their activity towards hydrogen activation and selective hydrogenation reactions[18–21]. Understanding the nature of the active site in these reactions is crucial in elucidating the relationship between atomistic structure and activity. Spectroscopic information on the stability of these alloys under more catalytically relevant conditions of CO is necessary for understanding the changes that can occur to the active isolated Ni or Pd atoms. Higher platinum group loadings on these systems have been investigated with these high pressure techniques,[11,22] but understanding the most stable adsorption site for CO adsorption on these dilute alloys and how it differs from pure Pd or pure Ni systems requires more in-depth studies[23].

6.2 Experimental

These experiments were performed at Brookhaven National Laboratories. The NiAu SAA was prepared by using an e-beam style evaporator, a flux of 10nA, and depositing the Ni onto the Au crystal held at 380 K[16]. The coverage was determined using the XPS, applying the appropriate corrections to the peaks assuming a monoatomic overlayer[7]. PdAu was prepared using a similar procedure of depositing Pd with a flux of 10nA, with the crystal held at 110^{o}C and applying the same corrections and measuring the area in the XPS with the same monoatomic surface layer growth assumption.

6.3 Results

In figure 6.1, the study of NiAu and PdAu SAAs are compared under constant

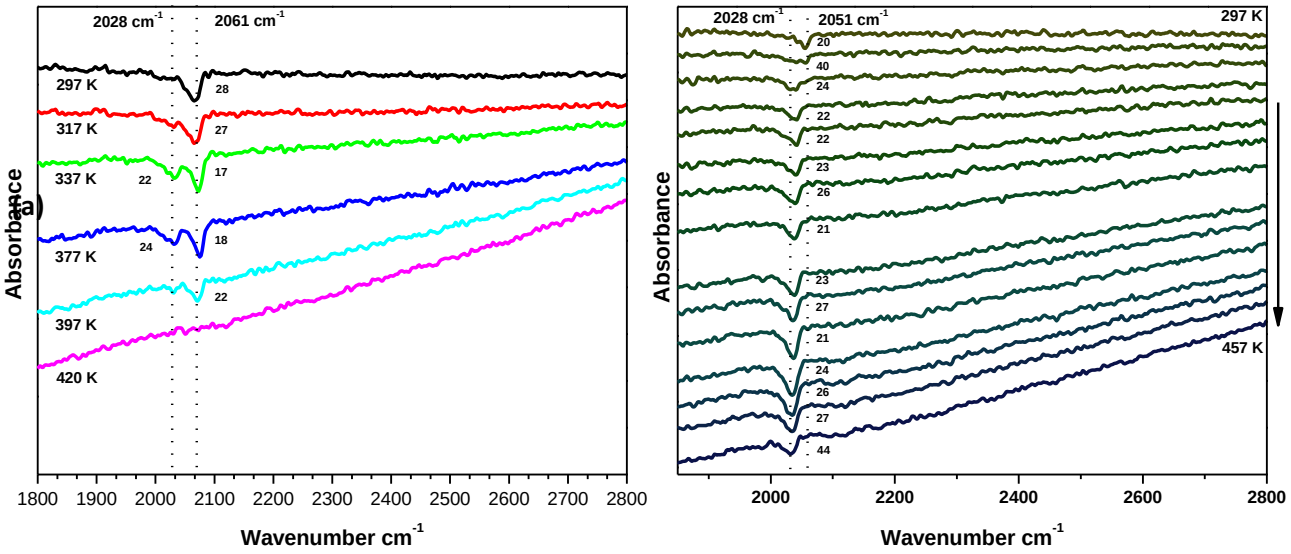

Figure 6.1: (a) 1mbar CO on a 0.03ML PdAu sample at increasing temperatures shows two absorbance bands centered at 2028 cm^{-1} and 2061 cm^{-1} which are both assigned to atop binding CO. The 2061 cm^{-1} peak is assigned to isolated single atoms of atop CO, the 2028 cm^{-1} peak is assigned to atop CO, but the exact nature of the site is unknown and discussed later **(b)** 1mbar CO on a 0.02 ML NiAu SAA showing two absorbance bands centered at 2051 cm^{-1} and 2028 cm^{-1} respectively. The 2051 cm^{-1} peak is assigned to atop CO on Ni single atoms, the 2028 cm^{-1} is assigned to atop CO, but the nature of the site is unknown and discussed below

elevated pressures of CO. The NiAu SAA exhibits one IR peak centered at 2051 cm^{-1} in agreement with other studies of this alloy for atop binding CO[24,25]. This peak persists at 1mbar CO, which can be seen in figure 6.1b. However, when increasing temperature while maintaining a constant pressure of CO, a second lower wavenumber peak centered around 2028 cm^{-1} appears, which is assigned to atop CO. This peak indicates a greater dispersion of Ni sites and higher isolation of CO on the surface. This peak could also be related to dicarbonyl formation where the Ni site is able to bind 2 different CO species. As the surface is heated it is possible that the dicarbonyl decomposes and only 1 CO is left binding on the surface. With increasing temperature, the CO peak decreases in intensity approaching 457 K, indicating either the loss of Ni to the bulk or the inability of

CO to bind to isolated Ni atoms at this pressure of CO and temperature. At 457 K this peak is broader, which suggests decreasing homogeneity of the surface sites. Further studies of the NiAu SAA with Ambient Pressure(AP-XPS) at these pressures and temperatures would help elucidate the nature of this loss of IR signal and differentiate between the two possible hypotheses: that Ni is diffusing into the Au(111) bulk, or that CO is unable to stick to Ni sites at this temperature. If possible one could examine the higher binding enery edge of the Ambient pressure XPS peak and be able to determine if the Ni is binding CO at various different temperatures. This technique of examining and measuring the shakeup feature of CO on dilute alloys has been previously applied to SAA systems to gain information about their stability under elevated pressures[26]. The CO pressure was decreased to examine the effect of pressure on the frequency of the IR shift, and at a standing pressure of 1e-6 mbar the frequency was 2051 cm^{-1}, which is in good agreement with atop CO on Ni(111)[27].

The PdAu SAA has a similar trend to the NiAu SAA at 1mbar CO. At low temperature only a singular peak at 2061 cm^{-1} is observed and then a second peak appears at 2028cm^{-1} as a function of heating, displayed in figure 6.1b. There is also a similar trend where one peak is more stable relative to the other, but in this case the higher wavenumber peak is more stable than the lower wavenumber peak as evidenced by the decrease in the low wavenumber peak intensity at 397 K. There are no absorbance peaks in the spectra at 420 K, which indicates that either the CO is unable to bind to the Pd at this temperature or that the Pd has undergone bulk diffusion and is no longer at the surface. This is in good agreement with the differences observed in UHV CO binding studies, whereby CO binds to NiAu SAA[16] roughly 65 K higher than PdAu[20] Further

studies of these dilute alloys at elevated pressures with AP-XPS would help determine the mechanism by which the CO signal is lost in the IR spectrum.

A 0.22ML NiAu sample was prepared and studied at 1mbar CO while changing the temperature, as displayed in figure 6.2. With a higher Ni coverage than previously studied, it was expected that CO may bind to this alloy at both atop sites and also bridge sites, which was not previously observed. Indeed, this sample had a peak in a different

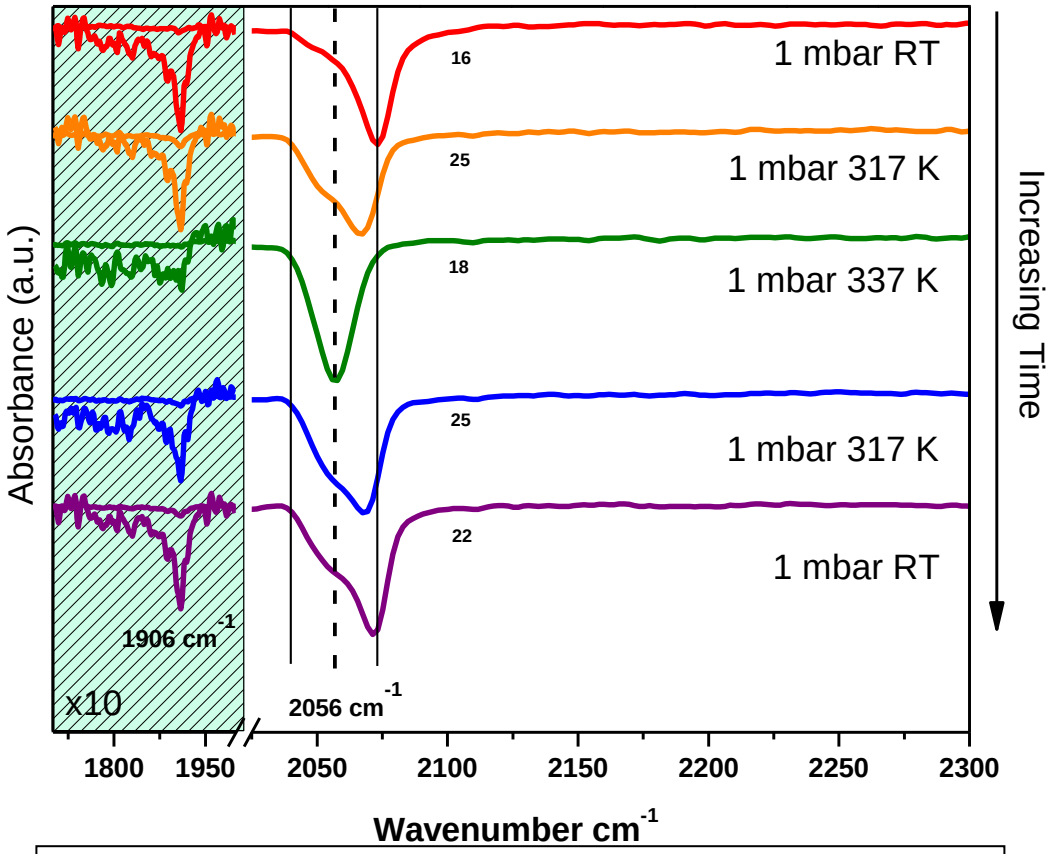

Figure 6.2: PD-RAIRs at 1mbar CO while changing temperature of a 0.22 ML NiAu alloy showing the disappearance of a bridge feature and reappearance as temperature is changed

region of the spectra at 1911 cm^{-1}, which indicates the presence of bridge bound species on the sample. As the sample was heated the peak in the atop region shifted down in wavenumber consistent with less CO-CO interactions which typically blue-shift IR

peaks, and at 337 K the bridge bound species is no longer apparent. Just as previously hypothesized, this could be either because CO can no longer stick at these pressures, or that the Ni that was binding CO in this region is no longer in the surface layer. The peaks in the atop region also appear to shift to lower wavenumbers and there again appears to be two peaks with shifting intensities relative to each other, with the higher wavenumber peak decreasing in wavenumber with increasing temperature. These peaks are assigned to atop CO, CO on isolated sites and CO on ensembles Ni in the Au surface. This is in good agreement with previous literature that has atop CO binding to atop ensembles[17,23] Evidence from catalytic studies indicate that ensemble atop CO peaks appear at a lower frequency than isolated sites[17]. In the nanoparticle study this atop peak assigned to ensembles is also more stable as it remains visible for a longer time post He exposure than the peak assigned to atop CO on NiAu. From this peak shift we can conclude that the lower wavenumber peak is more stable than the higher wavenumber feature in the 2000 cm^{-1} to 2100 cm^{-1} range, and that atop CO on dilute NiAu alloys is more stable than bridge bound species. This is consistent with the NiAu SAA surface and with previous studies[24,25].

Dilute Ni and Pd alloys in Au were examined using CO IR stretching frequencies to better understand the surface structures of the alloys under higher CO pressures. Dilute amounts of Ni interact more strongly with CO and are more thermally stable than dilute amounts of Pd as evidenced by the IR signal present at higher temperatures. The stretching frequencies of single-atom alloys CO atop sites both dilute alloys are shifted lower in wavenumber relative to their bulk frequencies which could be caused by greater dispersion of the CO on the surface leading to reduced CO-CO interactions. A higher coverage NiAu alloy was investigated and it was found that CO interacts more strongly with atop Ni sites than bridge sites, as indicated by the atop CO-IR peaks, located at 2056

cm^{-1}, stability at elevated temperature over the 1911 cm^{-1} bridge peak. This is in agreement with previous studies of Ni and Pd dilute alloys and especially interesting in that CO preferred binding sites differ between SAAs and their respective bulk systems[11,25,27,28]. This study indicates that isolated rather than agglomerated metal atoms are the most stable surface structure at elevated pressures of CO. Therefore SAAs may be the optimized structure for dilute alloys under elevated pressures of CO.

Further AP- XPS investigations of these systems would lead to a clearer understanding of the mechanism that causes a loss of CO signal in the IR spectra at elevated temperature which could elucidate key mechanisms of geometric and structural changes of dilute bimetallic alloy systems. Further infrared spectroscopy studies could also be conducted at elevated pressures to study the effect of CO on its ability to segregate single atoms to the surface. To properly investigate this, one could heat the SAA under a steady pressure of CO and collect frequent IR spectra until the atop signal is lost. The sample could then be cooled down(under UHV pressures), CO exposed again to the surface at UHV pressures to check that the reason for the loss of signal is due to the dopant not being in the surface layer. The experimental chamber could then be brought to higher pressures and infrared spectra taken periodically to check for the presence of single atoms in the surface layer. Comparing the differences between the pressures needed to bring atoms to the surface layer and by varying the temperature at these elevated pressures of CO, the kinetic and thermodynamic processes that bring these single atoms to the surface in the presence of adsorbates could be better understood. Relationships between the binding strengths of CO to these single atom alloys in UHV and under more realistic conditions would be useful, and AP-XPS and CO-IR are techniques that bridge this gap. Finally, using an adsorbate other than CO to hold an atom on the surface would be useful to correlate the binding strengths other adsorbates to the

ability of atoms to overcome the thermodynamic driving force of dissolving the dopant atom into the bulk at higher temperatures.

6.4 References

(1) M. D. Argyle; C. H. Bartholomew. Heterogeneous Catalyst Deactivation and Regeneration: A Review. *Catalysts* **2015**, *5* (1), 145–269.

(2) G. Sun; Z.-J. Zhao; R. Mu; S. Zha; L. Li; S. Chen; K. Zang; J. Luo; Z. Li; S. C. Purdy; et al. Breaking the Scaling Relationship via Thermally Stable Pt/Cu Single Atom Alloys for Catalytic Dehydrogenation. *Nat. Commun.* **2018**, *9* (1), 4454.

(3) Z.-J. Zhao; C. Chiu; J. Gong. Molecular Understandings on the Activation of Light Hydrocarbons over Heterogeneous Catalysts. *Chem. Sci.* **2015**, *6* (8), 4403–4425.

(4) P. Forzatti; L. Lietti; I. Nova; E. Tronconi. Diesel NOx Aftertreatment Catalytic Technologies: Analogies in LNT and SCR Catalytic Chemistry. *Catal. Today* **2010**, *151* (3–4), 202–211.

(5) F. Gao; D. W. Goodman. Pd-Au Bimetallic Catalysts: Understanding Alloy Effects from Planar Models and (Supported) Nanoparticles. *Chem. Soc. Rev.* **2012**, *41* (24), 8009–8020.

(6) F. Aqra; A. Ayyad. Surface Free Energy of Alkali and Transition Metal Nanoparticles. *Appl. Surf. Sci.* **2014**, *314*, 308–313.

(7) M. A. Van Spronsen; K. Daunmu; C. R. O'Connor; T. Egle; H. Kersell; J. Oliver-Meseguer; M. B. Salmeron; R. J. Madix; P. Sautet; C. M. Friend. Dynamics of Surface Alloys: Rearrangement of Pd/Ag(111) Induced by CO and O2. *J. Phys. Chem. C* **2019**, *123* (13), 8312–8323.

(8) G. Giannakakis; A. Trimpalis; J. Shan; Z. Qi; S. Cao; J. Liu; J. Ye. NiAu Single Atom Alloys for the Non-Oxidative Dehydrogenation of Ethanol to Acetaldehyde and Hydrogen. *Top. Catal.* **2018**, *61* (5), 475–486.

(9) A. Bukhtiyarov; I. Prosvirin; A. A. Saraev; A. Y. Klyushin; A. Knop-Gericke; V. Bukhtiyarov. In Situ Formation of the Active Sites in Pd-Au Bimetallic Nanocatalysts for CO Oxidation: NAP (near Ambient Pressure) XPS and MS Study. *Faraday Discuss.* **2018**.

(10) F. Tao; M. E. Grass; Y. Zhang; D. R. Butcher; J. R. Renzas; Z. Liu; J. Y. Chung; B. S. Mun; M. Salmeron; G. A. Somorjai. Reaction-Driven Restructuring of Rh-Pd and Pt-Pd Core-Shell Nanoparticles. *Science (80-.).* **2008**, *322* (November), 932–935.

(11) F. Gao; Y. Wang; D. W. Goodman. CO Oxidation over AuPd(100) from Ultrahigh Vacuum to near-Atmospheric Pressures: CO Adsorption-Induced Surface Segregation and Reaction Kinetics. *J. Phys. Chem. C* **2009**, *113* (33), 14993–15000.

(12) S. Alayoglu; F. Tao; V. Altoe; C. Specht; Z. Zhu; F. Aksoy; D. R. Butcher; R. J. Renzas; Z. Liu; G. A. Somorjai. Surface Composition and Catalytic Evolution of Au x Pd 1-x (x = 0.25, 0.50 and 0.75) Nanoparticles under CO/O2 Reaction in Torr Pressure Regime and at 200 °c. *Catal. Letters* **2011**, *141* (5), 633–640.

(13) R. T. Hannagan; G. Giannakakis; M. Flytzani-Stephanopoulos; E. C. H. Sykes. Single-Atom Alloy Catalysis. *Chem. Rev.* **2020**, *120*, 12044–12088.

(14) B. Eren; D. Zherebetskyy; L. L. Patera; C. H. Wu; H. Bluhm; C. Africh; L.-W. Wang; G. A. Somorjai; M. Salmeron. Activation of Cu(111) Surface by Decomposition into Nanoclusters Driven by CO Adsorption. *Science (80-.).* **2016**, *351* (6272).

(15) A. Trimpalis; G. Giannakakis; S. Cao; M. Flytzani-stephanopoulos. NiAu Single Atom Alloys for the Selective Oxidation of Methacrolein with Methanol to Methyl Methacrylate. *Catal. Today* **2019**, No. December 2018, 0–1.

(16) P. Kress; R. Réocreux; R. Hannagan; T. Thuening; J. A. Boscoboinik; M. Stamatakis; E. C. H. Sykes. Mechanistic Insights into Carbon-Carbon Coupling on NiAu and PdAu Single-Atom Alloys. *J. Chem. Phys.* **2021**, *154* (20).

(17) G. Giannakakis; A. Trimpalis; J. Shan; Z. Qi; S. Cao; J. Liu; J. Ye; J. Biener; M. Flytzani-Stephanopoulos. NiAu Single Atom Alloys for the Non-Oxidative Dehydrogenation of Ethanol to Acetaldehyde and Hydrogen. *Top. Catal.* **2017**, *77030* (0), 1–23.

(18) A. E. Baber; H. L. Tierney; E. C. H. Sykes. Atomic-Scale Geometry and Electronic Structure of

Catalytically Important Pd/Au Alloys. *ACS Nano* **2010**, *4* (3), 1637–1645.

(19) A. E. Baber; H. L. Tierney; T. J. Lawton; E. C. H. Sykes. An Atomic-Scale View of Palladium Alloys and Their Ability to Dissociate Molecular Hydrogen. **2011**, *02155*, 607–614.

(20) F. R. Lucci; M. T. Darby; M. F. G. Mattera; C. J. Ivimey; A. J. Therrien; A. Michaelides; M. Stamatakis; E. C. H. Sykes. Controlling Hydrogen Activation, Spillover, and Desorption with Pd-Au Single-Atom Alloys. *J. Phys. Chem. Lett.* **2016**, *7* (3), 480–485.

(21) J. Liu; J. Shan; F. R. Lucci; S. Cao; E. C. Sykes; M. Flytzani-Stephanopoulos. Palladium-Gold Single Atom Alloy Catalysts for Liquid Phase Selective Hydrogenation of 1-Hexyne. *Catal. Sci. Technol.* **2017**, *7*, 4276–4284.

(22) C. M. Kruppe; J. D. Krooswyk; M. Trenary. Polarization-Dependent Infrared Spectroscopy of Adsorbed Carbon Monoxide to Probe the Surface of a Pd/Cu(111) Single-Atom Alloy. *J. Phys. Chem. C* **2017**, *121* (17), 9361–9369.

(23) C. C. Leon; Q. Liu; S. T. Ceyer. CO Adsorption on Gold Nickel Au-Ni(111) Surface Alloys. *J. Phys. Chem. C* **2019**, *123* (14), 9041–9058.

(24) J. I. Cohen; R. G. Tobin; J. I. Cohen; R. G. Tobin. CO Adsorption on Nanoislands : Ni on Au (111) CO Adsorption on Nanoislands : Ni on Au (111). **2018**, *224702* (111).

(25) F. Yang; Y. Yao; Z. Yan; H. Min; D. W. Goodman. Applied Surface Science Preparation and Characterization of Planar Ni – Au Bimetallic Model Catalysts. *Appl. Surf. Sci.* **2013**, *283*, 263–268.

(26) J. P. Simonovis; A. Hunt; R. M. Palomino; S. D. Senanayake; I. Waluyo. Enhanced Stability of Pt-Cu Single-Atom Alloy Catalysts: In Situ Characterization of the Pt/Cu(111) Surface in an Ambient Pressure of CO. *J. Phys. Chem. C* **2018**, *122* (8), 4488–4495.

(27) J. C. Camputano; R. G. Greenler. The Adsorption Sites of CO on Ni(111) as Determined by Infrared Reflection-Absorption Spectroscopy. *Surf. Sci.* **1979**, *83*, 301–312.

(28) T. Hager; H. Rauscher; R. J. Behm. Interaction of CO with PdCu Surface Alloys Supported on

Ru(0001). *Surf. Sci.* **2004**, *558*, 181–194.

Chapter 7: PtCrAg Trimetallic Alloy for selective non-oxidative Ethanol Dehydrogenation

7.1 Introduction

SAAs (SAAs) have proven to be effective catalysts for many reactions[1–6], and provide a host of fundamental benefits. These materials feature well-defined active sites that are relatively easy to model[7]. The controlled ensemble size also provides catalytic benefits, such as allowing spillover and causing deviations from linear relationships between energies[2,8–10]. advantages of SAAs stem from the small active ensemble embedded in an inert host. However, a single-atom active site may not be able to effectively stabilize larger intermediates or transition states, and relying on the chemical properties of just a single active atom can limit control over reactivity[11,12].

To address these limitations of SAAs, it would be useful to combine two active atoms with different chemical reactivity into a localized active site. This larger active site could be critical for catalyzing certain reaction steps with larger transition states, but it is difficult to create dimer sites of the same atom without also creating many larger islands. Further, a dimer site with two metals would allow improved control over the reactivity beyond SAAs. For example, breaking a C-O or O-H bond may be facilitated when one surface atom attracts the O atom and another surface atom attracts the H or C atom. Embedding this active site in a more inert host may still inhibit overdecomposition of intermediates and poisoning of the surface.

Dual atom catalysts supported on oxides or other materials have recently been shown to be effective catalysts for some reactions[13–16]. Because of the similarities between SAAs and single-atom catalysts[17–19], trimetallic dual-atom alloys may also have desirable catalytic properties. Further, supported dual atom catalysts are structurally complex, making them more difficult to design, synthesize, and characterize, while the active site is much easier to elucidate on dual atom alloys. The metal host for dual-atom alloys could also allow some of the desirable properties of single atom alloys, such as spillover.

Here, we computationally design and experimentally synthesize and test a catalytic surface site consisting of a heterometallic dimer embedded in an inert host. This site, Pt_1Cr_1-Ag, can dehydrogenate ethanol, while both Pt_1-Ag nor Cr_1-Ag are unreactive towards this reaction. Adjacent Pt and Cr atoms are necessary to kinetically and thermodynamically facilitate the reaction. This work demonstrates the possibility and utility of expanding beyond SAAs into localized mixed-metal dimers, expanding the design space of active sites in heterogeneous catalysis.

7.2 Experimental

The surface science experiments were performed on an Omnicron low-temperature STM and a separate TPD chamber. Both chambers have a base pressure of 1×10^{-10} mbar. The deposition and formation of the PtAg alloy was performed following a previously reported procedure[20]. The $Cr(CO)_6$ was deposited using the vapor pressure above a solid of $Cr(CO)_6$ which came from Sigma aldrich (98% purity). The solid compound was placed into a dosing tube and connected to a leak valve, during deposition the Ag(111) crystal was held at 330 K, and the pressure in the chamber was 1×10^{-6} mbar during the deposition. The baseline pressure in the dosing line was $<1 \times 10^{-4}$, and once exposed to the tube of carbonyl the pressure rose to 5×10^{-1} mbar. For all surfaces studied in STM, the Pt was deposited

first, and then the carbonyl. The TPD experiments were collected with a heating rate of 1.5 K/s. Quantitative mass spectrometry was used to determine the amounts of dopant on the surface using CO TPDs following a previous procedure[21], and referenced to monolayer ethanol exposures.

Clean Cu(111) (99.999%, Princeton Scientific) was prepared via Ar^+ sputtering followed by 750 K and 1000 K in the TPD and STM chambers respectively. Liquid ethanol- D_6 (Sigma Aldrich 99.5%) was purified via freeze-pump thaw cycles prior to exposure to the chamber. Doses are given in Langmuirs (1 L = 1 x 10^{-6} mbar s^{-1}) Deposition of Pt was performed using an Omnicron EFM 3 electron-beam evaporator, while the crystal was held at 380 K, coverages were calibrated using CO titration and quantitatively comparing it to saturated ethanol exposures. $Cr(CO)_6$ was dosed for various times at 1 x 10^{-6} mbar with the crystal held at 330 K, and the coverage was determined using CO calibration described elsewhere[21].

7.2 Results and Discussion

To discover synthesizable dimer pairs, we computationally screened PtM-Ag(111) and PdM-Ag(111) for stability to discover cases where the heterometallic dimer is stable and is favored over the homometallic dimers. We calculated the heterometallic dimer formation energy, which must be negative to drive formation of this dimer, as well as the homometallic dimer formation energy, which should be less negative than the heterometallic dimer (and ideally positive). Many dimers are predicted to be synthesizable.

To find dimers with desirable chemical reactivity towards C-O and O-H bonds, we searched for stable pairs where one metal is likely to attract O and the other is likely to attract H. Based on our previous work[22], Cr is relatively oxophilic, while Pt is relatively carbophilic[23] DFT calculations of H and

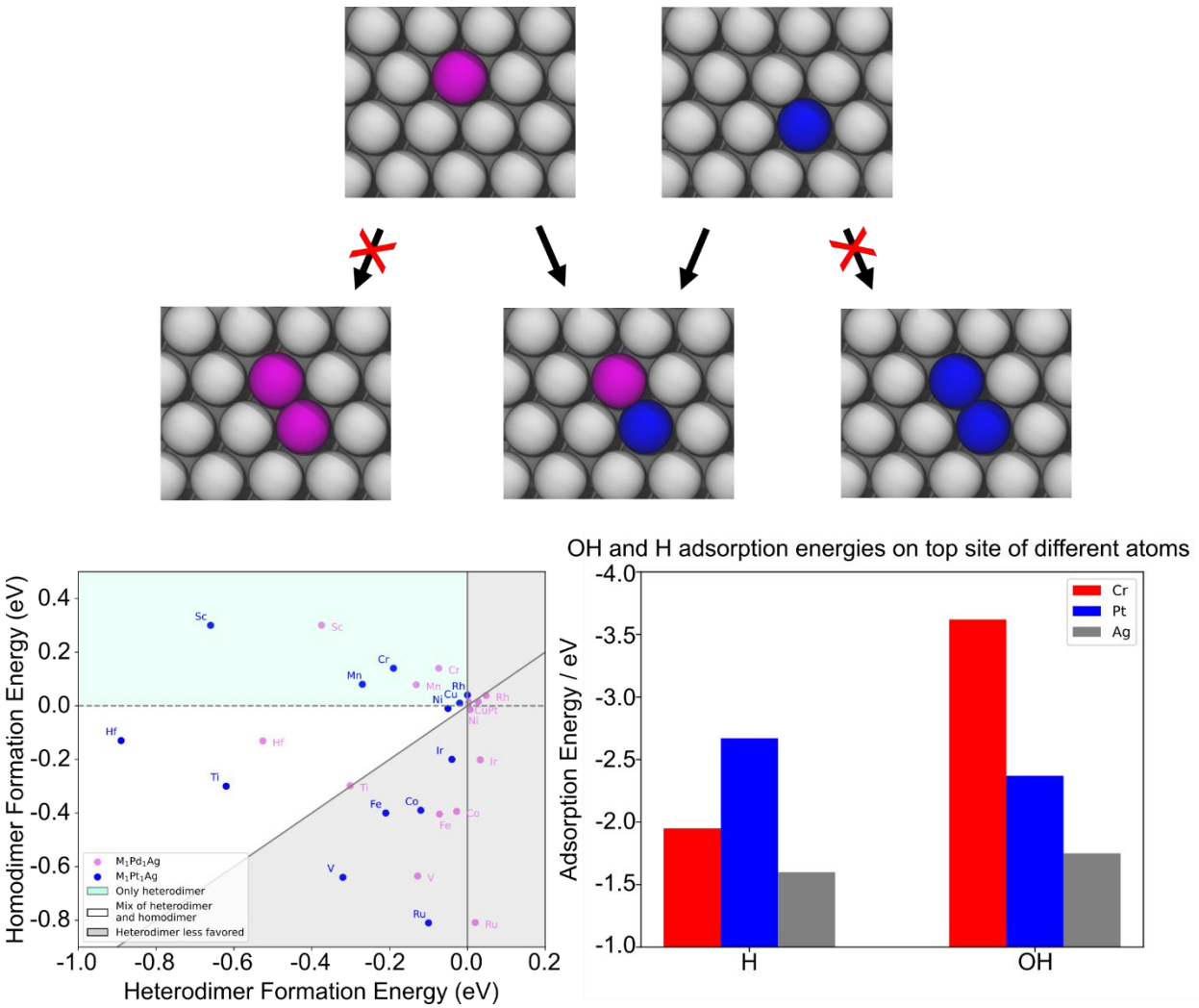

Figure 7.1: a) Screening was performed to find systems that will form heterometallic dimers instead of homometallic dimers. b) Computational screening of the stability of various dimers based on Pt_1Ag and Pd_1Ag SAAs as hosts. The homodimer and heterodimer formation energies are shown. c) DFT-calculated top-site H and OH adsorption energies in PtCr-Ag, showing the different chemical reactivity of Pt and Cr in the dimer.

OH on the top sites of PtCr-Ag confirm that Pt strongly binds H and Cr strongly binds OH. Hence, PtCr-Ag is predicted to be both synthesizable and reactive towards O-H bonds.

Based on the computational screening, we therefore synthesized PtCr-Ag by taking an Ag(111) crystal, evaporating Pt from a rod, and then depositing gas phase Cr-CO_6. The goal was to selectively deposit Cr near Pt sites, as the Cr carbonyl may be more likely to react at Pt sites than at Ag sites, and the Pt-Cr bond is stronger than the Cr-Ag, or Pt-Ag bond.

The PtAg SAA alloy has been previously characterized and formed under UHV conditions[20].

The results of the synthesis of the PtCrAg alloy can be clearly seen in figure 7.2. The STM images are all compared to simulated STM images. In (a) and (b) CrAg with and without CO is examined and most of the Cr studied has CO on it due to the way it was deposited. The Cr does not protrude much out of plane of the surface indicating that much of the Cr is alloyed into the surface layer of the Ag(111). In (e) and (f) Pt in Ag(111) can be seen without and with CO adsorbed, along with the corresponding simulated images in (g) and (h). It can be seen from these images that Pt and Cr largely exist as isolated species in the surface of Ag(111), there were some larger clusters of Cr that were observed. In (i) and (j) the trimetallic surface is shown both at a larger scale and at a smaller scale. When observing the trimetallic surface, the Cr usually had CO adsorbed on it, which made it distinguishable from the Pt sites due to the Cr species interacting strongly with the STM tip and causing disturbances in the imaging. In (j) a close up a dimer site can be seen, and (k) and (l) are the corresponding dimer sites without CO and with CO. The PtAg surface was also characterized with CO RAIRs as seen in figure 7.3. A 0.02 PtAg sample was prepared and CO RAIRS was acquired at RT under a standing pressure of 1×10^{-6} mbar.

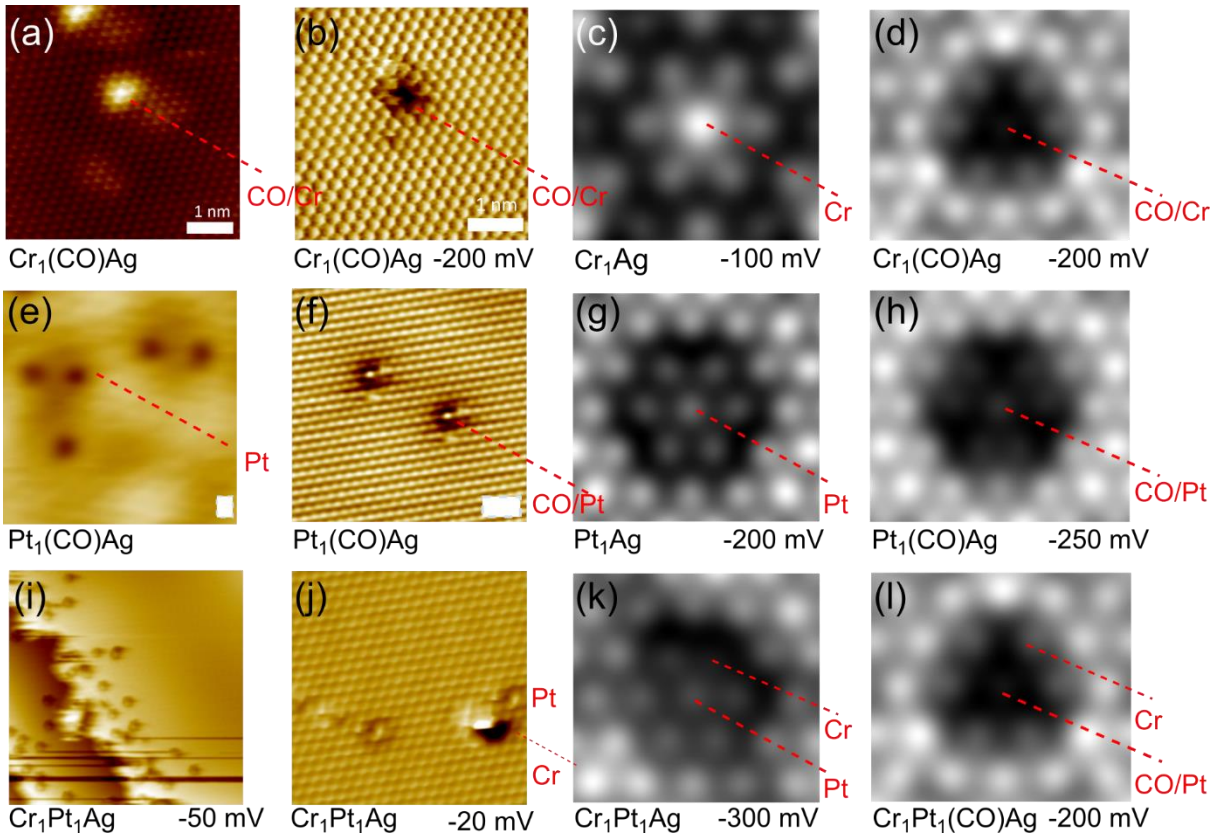

Figure 7.2: STM images of various different PtCrAg alloys. (a) STM image of Cr without CO. (b) STM image of a $Cr(CO)_6$ complex. (c) Simulated STM image of Cr without CO, (d) simulated STM image with CO. (E) PtAg STM image without CO, (f) PtAg STM image with CO adsorbed). (g) Simulated PtAg STM image without CO adsorbed, (h) simulated STM image with CO adsorbed. (i) CrPtAg larger scale STM image. (j) close up of PtCrAg dimer STM image. (k) simulated PtCrAg STM image without CO, and with CO (l). All of the scale bars are 1nm

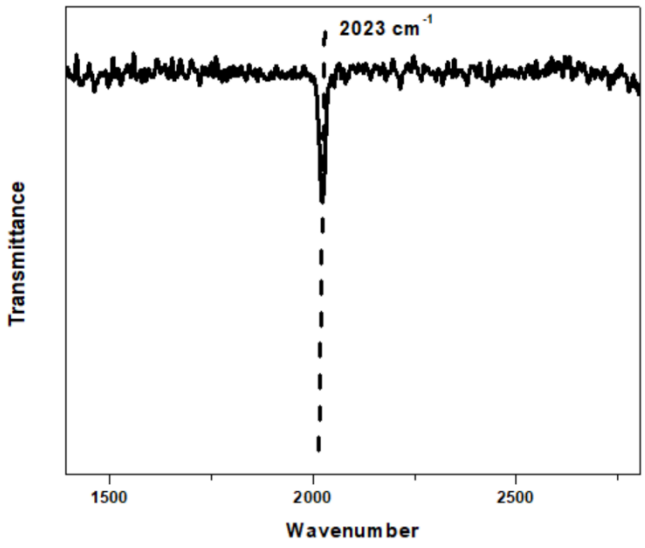

Figure 7.3: CO RAIRS of 0.03 PtAg SAA acquired at room temperature

We then tested the catalytic activity of PtCr-Ag towards ethanol dehydrogenation to acetaldehyde with TPD experiments. This reaction was chosen as a simple example where O-H bond breaking is critical, but complete decomposition is not desired[24–28]. We exposed the surface to deuterated ethanol and detected acetaldehyde and D_2 as products as seen in figure 7.4. In contrast, Pt-Ag and Cr-Ag do not dehydrogenate ethanol even at higher loadings than present in the trimetallic experiments. It is evident that there is a unique situation that occurs when both Pt and Cr are present together in the surface that does not occur when either one is in only a bimetallic state.

DFT calculations show that the mixed reactivity of the PtCr site is crucial for its activity in breaking the O-H bond in ethanol. Pt-Ag stabilizes H, but ethoxy is forced to an Ag site where it is relatively unstable. Conversely, ethoxy is quite stable on Cr-Ag, but H is forced to an Ag site where it is relatively unstable. Hence, on both of the SAAs ethoxy+H is less stable than ethanol, such that there is no thermodynamic driving force to break the O-H bond. In the mixed dimer site, Cr can stabilize ethoxy while Pt stabilizes

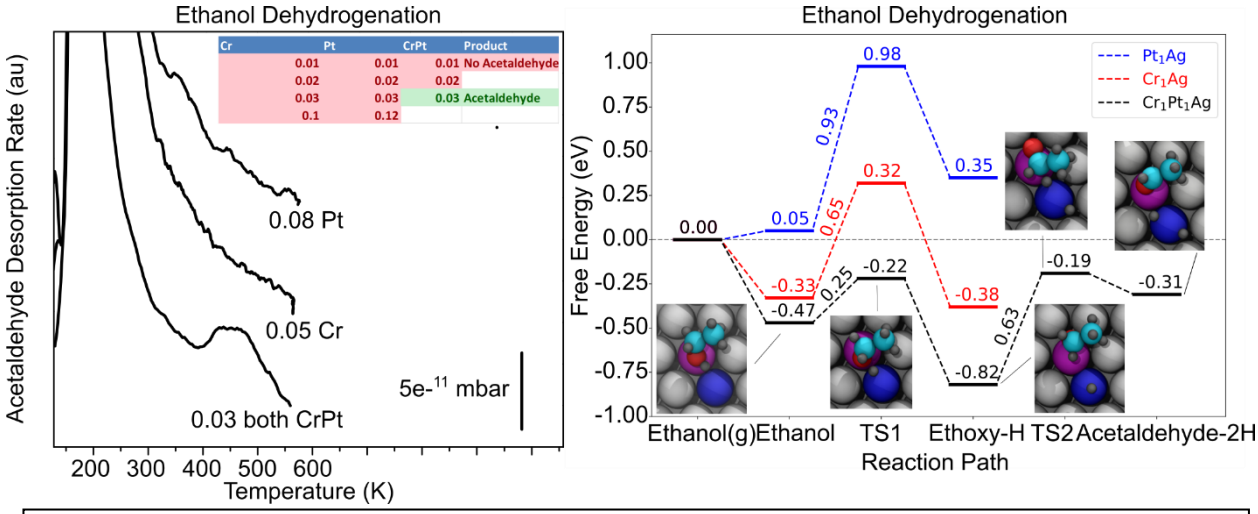

Figure 7.4: (a) TPD spectra showing D_2 and H_2 desorption from PtAg, CrAg, and PtCrAg, after Ethanol exposure showing that only the trimetallic surface produces D_2. Correspondingly the trimetallic surface is the only surface that generates acetaldehyde. **(b)** The DFT energetic pathway of ethanol to acetaldehyde in which it is shown that the dimer site is the lowest energy pathway.

H, driving this reaction step forwards. Further, Pt and Cr need to be adjacent to each to stabilize the transition state. On the SAAs, desorption of ethanol is kinetically favored over breaking the O-H bond, but on the PtCr mixed site the transition state is lower in energy than gas-phase ethanol. Therefore, Cr and Pt must be adjacent to each for the O-H bond breaking to be thermodynamically and kinetically favorable.

7.3 Conclusion

We have computationally designed and experimentally tested a new kind of catalytic active site, where a dimer of two reactive atoms (Pt,Cr) is imbedded in a more inert host (Ag). DFT calculations suggest that many materials with this structure are synthesizable. STM confirms the presence of Pt-Cr sites. TPD shows that these sites are active for ethanol dehydrogenation, while the PtAg and CrAg SAAs are not. DFT calculations show that the PtCr mixed site is needed for O-H bond breaking to be thermodynamically and kinetically favorable.

This work opens up a new class of catalytic materials that can be computationally designed using the method we developed here. This class of materials provides an extension to SAAs with a larger active site and high tunability through proper choice of all three metals, as well as the metal-metal interaction. The opening of design space to include another active metal allows for reactions to be more tailored to the specific intermediates and lowering the barriers for specific molecular activations. We have identified other compositions that are predicted to be stable.

(1) R. T. Hannagan; G. Giannakakis; R. Réocreux; J. Schumann; J. Finzel; Y. Wang; A. Michaelides; P. Deshlahra; P. Christopher; M. Flytzani-Stephanopoulos; et al. First-Principles Design of a Single-Atom–Alloy Propane Dehydrogenation Catalyst. *Science (80-.).* **2021**, *372* (6549), 1444–1447.

(2) R. T. Hannagan; G. Giannakakis; M. Flytzani-Stephanopoulos; E. C. H. Sykes. Single-Atom Alloy Catalysis. *Chem. Rev.* **2020**, *120*, 12044–12088.

(3) F. R. Lucci; J. Liu; M. D. Marcinkowski; M. Yang; L. F. Allard; M. Flytzani-Stephanopoulos; E. C. H. Sykes. Selective Hydrogenation of 1,3-Butadiene on Platinum–Copper Alloys at the Single-Atom Limit. *Nat. Commun.* **2015**, *6*, 8550.

(4) M. D. Marcinkowski; M. Darby; J. Liu; J. Wimble; F. R. Lucci; S. Lee; A. Michaelides; Flytzani-Stephanopoulos; M. Stamatakis; E. C. H. Sykes. Pt/Cu Single-Atom Alloys as Coke Resistant Catalysts for Efficient C-H Activation. *Nat. Chem.* **2018**.

(5) S. Zha; G. Sun; T. Wu; J. Zhao; Z.-J. Zhao; J. Gong. Identification of Pt-Based Catalysts for Propane Dehydrogenation *via* a Probability Analysis. *Chem. Sci.* **2018**, *00*, 1–7.

(6) J. Liu; M. B. Uhlman; M. M. Montemore; A. Trimpalis; G. Giannakakis; J. Shan; S. Cao; R. T. Hannagan; E. C. H. Sykes; M. Flytzani-Stephanopoulos. Integrated Catalysis-Surface Science-Theory Approach to Understand Selectivity in the Hydrogenation of 1-Hexyne to 1-Hexene on PdAu Single-Atom Alloy Catalysts. *ACS Catal.* **2019**, *9* (9), 8757–8765.

(7) M. T. Darby; R. Réocreux; E. C. H. Sykes; A. Michaelides; M. Stamatakis. Elucidating the Stability and Reactivity of Surface Intermediates on Single-Atom Alloy Catalysts. *ACS Catal.* **2018**, *8* (6), 5038–5050.

(8) M. T. Darby; M. Stamatakis; A. Michaelides; E. C. H. Sykes. Lonely Atoms with Special Gifts: Breaking Linear Scaling Relationships in Heterogeneous Catalysis with Single-Atom Alloys. *J. Phys. Chem. Lett.* **2018**, *9* (18), 5636–5646.

(9) G. Giannakakis; M. Flytzani-stephanopoulos; E. C. H. Sykes. Single-Atom Alloys as a Reductionist Approach to the Rational Design of Heterogeneous Catalysts. *Acc. Chem. Res.* **2018**, *52*, 237–247.

(10) R. T. Hannagan; G. Giannakakis; R. Reocreux; J. Schumann; J. Finzel; S. Cao; Y. Wang; T. Balema; A. Michaelides; P. Deshlahra; et al. First Principles Guided Design of a Propane Dehydrogenation Catalyst. **2020**.

(11) M. Chen; D. Kumar; C. W. Yi; D. W. Goodman. The Promotional Effect of Gold in Catalysis by Palladium-Gold. *Science (80-.).* **2005**, *310* (5746), 291–293.

(12) S. Han; C. B. Mullins. Surface Alloy Composition Controlled O2 Activation on Pd–Au Bimetallic Model Catalysts. *ACS Catal.* **2018**, acscatal.8b00140.

(13) X. Guo; J. Gu; S. Lin; S. Zhang; Z. Chen; S. Huang. Tackling the Activity and Selectivity Challenges of Electrocatalysts toward the Nitrogen Reduction Reaction via Atomically Dispersed

Biatom Catalysts. *J. Am. Chem. Soc.* **2020**, *142* (12), 5709–5721.

(14) Y. Li; Q. Zhang; C. Li; H. N. Fan; W. Bin Luo; H. K. Liu; S. X. Dou. Atomically Dispersed Metal Dimer Species with Selective Catalytic Activity for Nitrogen Electrochemical Reduction. *J. Mater. Chem. A* **2019**, *7* (39), 22242–22247.

(15) L. Zhang; R. Si; H. Liu; N. Chen; Q. Wang; K. Adair; Z. Wang; J. Chen; Z. Song; J. Li; et al. Atomic Layer Deposited Pt-Ru Dual-Metal Dimers and Identifying Their Active Sites for Hydrogen Evolution Reaction. *Nat. Commun.* **2019**, *10* (1), 1–11.

(16) J. Fu; J. Dong; R. Si; K. Sun; J. Zhang; M. Li; N. Yu; B. Zhang; M. G. Humphrey; Q. Fu; et al. Synergistic Effects for Enhanced Catalysis in a Dual Single-Atom Catalyst. *ACS Catal.* **2021**, *11* (4), 1952–1961.

(17) X. Li; X. Yang; Y. Huang; T. Zhang; B. Liu. Supported Noble-Metal Single Atoms for Heterogeneous Catalysis. *Adv. Mater.* **2019**, *31*, 1902031.

(18) L. Liu; A. Corma. Metal Catalysts for Heterogeneous Catalysis: From Single Atoms to Nanoclusters and Nanoparticles. *Chem. Rev.* **2018**, acs.chemrev.7b00776.

(19) G. Giannakakis; M. Flytzani-Stephanopoulos; E. C. H. Sykes. Single-Atom Alloys as a Reductionist Approach to the Rational Design of Heterogeneous Catalysts. *Acc. Chem. Res.* **2019**, *52* (1), 237–247.

(20) D. A. Patel; P. L. Kress; L. A. Cramer; A. M. Larson; E. C. H. Sykes. Elucidating the Composition of PtAg Surface Alloys with Atomic-Scale Imaging and Spectroscopy. *J. Chem. Phys.* **2019**, *151* (16).

(21) F. R. Lucci; M. T. Darby; M. F. G. Mattera; C. J. Ivimey; A. J. Therrien; A. Michaelides; M. Stamatakis; E. C. H. Sykes. Controlling Hydrogen Activation, Spillover, and Desorption with Pd-

Au Single-Atom Alloys. *J. Phys. Chem. Lett.* **2016**, *7* (3), 480–485.

(22) G. O. Kayode; M. M. Montemore. Factors Controlling Oxophilicity and Carbophilicity of Transition Metals and Main Group Metals. *J. Mater. Chem. A* **2021**, *9* (39), 22325–22333.

(23) A. Fürstner; P. W. Davies. *Synthetic Methods Catalytic Carbophilic Activation : Catalysis by Platinum and Gold p Acids Angewandte*; 2007.

(24) Z. T. Wang; Y. Xu; M. El-Soda; F. R. Lucci; R. J. Madix; C. M. Friend; E. C. H. Sykes. Surface Structure Dependence of the Dry Dehydrogenation of Alcohols on Cu(111) and Cu(110). *J. Phys. Chem. C* **2017**, *121* (23), 12800–12806.

(25) J. Shan; J. Liu; M. Li; S. Lustig; S. Lee; M. Flytzani-Stephanopoulos. NiCu Single Atom Alloys Catalyze the C–H Bond Activation in the Selective Non- Oxidative Ethanol Dehydrogenation Reaction. *Appl. Catal. B Environ.* **2018**, *226* (June 2017), 534–543.

(26) E. J. Evans; H. Li; W. Y. Yu; G. M. Mullen; G. Henkelman; C. B. Mullins. Mechanistic Insights on Ethanol Dehydrogenation on Pd-Au Model Catalysts: A Combined Experimental and DFT Study. *Phys. Chem. Chem. Phys.* **2017**, *19* (45), 30578–30589.

(27) X. Liu; B. Xu; J. Haubrich; R. J. Madix; C. M. Friend. Surface-Mediated Self-Coupling of Ethanol on Gold. *J. Am. Chem. Soc.* **2009**, *131* (16), 5757–5759.

(28) E. Santacesaria; G. Carotenuto; R. Tesser; M. Di Serio. Ethanol Dehydrogenation to Ethyl Acetate by Using Copper and Copper Chromite Catalysts. *Chem. Eng. J.* **2012**, *179*, 209–220.

Chapter 8:Summary and Future Directions

8.1 Summary

The aim of this thesis was to form structure reactivity relationships on dilute alloy catalysts. This was done on Cu, Ag, and Au based alloys and spanned from single crystal model studies to nanoparticles studies which proves the usefulness of this approach for real world applications and understanding. Chapter 3 examined the ability of single isolated Ni atoms in Au and their ability to break C-I bonds in methyl iodide and then couple the methyl species on the surface to form only ethane[1]. Theory was used to better understand the system and make it more analogous to homogenous catalysis.

Chapter 4 examined the conversion of adsorbed ethyl groups on Cu(111) and a PtCu SAA[2]. It was demonstrated that the single Pt sites on the surface changed the selectivity of the Cu surface from dehydrogenating the ethyl groups only to also being able to hydrogenate the ethyl species. This hydrogenation of ethyl species was able to be controlled by controlling the amount of adsorbed hydrogen on the surface prior to reaction. Again theory was able to be used to better understand the mechanism of the hydrogenation and dehydrogenation reaction to understand at which site the reactions were taking place.

Chapter 5 examined a NiAu SAA for its ability to dehydrogenate ethanol. It was shown conclusively in nanoparticle studies that single Ni atoms were active for the selective conversion of ethanol to acetaldehyde. In single crystal studies, the decomposition of ethanol to undesired hydrocarbons was observed for Ni ensembles which were seen in the IR spectra. A comparison of IR spectra between nanoparticle and single crystal studies were in agreement that the appearance of CO vibrational signals

that are not correlated with atop CO lead to undesirable reaction pathways, likely due to the ability of larger Ni ensembles to break C-C bonds. Theory was again used to describe the mechanism and understand the catalytic cycle in more detail.

Chapter 6 examined used elevated pressures of CO and used vibrational studies to better understand the relationship between binding strength to dilute alloys at elevated pressures. It was shown that at elevated pressures CO will bind to these alloys at temperatures not seen under UHV conditions. It has been shown by Ouyang *et al*[3] that dilute alloys ensemble can be controlled by varying the pressure of an adsorbate such as CO. In Chapter 6, this changing of sites was not observed, but the relative intensity change of sites did show that isolated sites on Ni in Au were favorable since the atop signal was observed at higher temperatures where the bridge bound peak had disappeared. The HP-RAIRs setup is a powerful tool to be able to examine the effects of elevated pressures on binding to dilute alloys. In the future these effects should be examined to correlate the binding strength of adsorbates under UHV conditions to those at elevated pressures. This technique is able to bridge the pressure gap[4] between single crystal studies and elevated pressure studies. The effects of other adsorbates to bring the dilute elements to the surface is another promising aspect of this technique that should be further examined in the future since there are limited studies on the ability of adsorbates that are not CO or H_2 in changing the surface composition of alloys[5–7].

Chapter 7 examined a novel type of alloy in PtCrAg for its catalytic ability to convert ethanol to acetaldehyde. This work was based off of original characterization work on the PtAg SAA[8]. The choice of other elements was driven by theory that led to

the choice of an alloy that favors heterodimer formation, over homodimer formation. It was shown experimentally that the dimer was necessary for the conversion of ethanol to acetaldehyde, which was confirmed by DFT. The DFT showed the necessity of one dopant to accept the ethoxy species on the surface, while the other component preferentially binds the hydrogen formed after the O-H bond breakage. This chapter shows that the design principles that have guided SAAs is applicable to other different dilute alloys and that trimetallic alloys open up the possibility of being able to new reactions that SAAs are uncapable of activating.

The approach taken in this thesis have shown the ability to rationally design catalysts. It has shown that through a combined theory, surface science, and practical catalysis approach can find new catalysts for challenging reactions

8.2 References

(1) Kress, P.; Réocreux, R.; Hannagan, R.; Thuening, T.; Boscoboinik, J. A.; Stamatakis, M.; Sykes, E. C. H. Mechanistic Insights into Carbon-Carbon Coupling on NiAu and PdAu Single-Atom Alloys. *J. Chem. Phys.* **2021**, *154* (20). https://doi.org/10.1063/5.0048977.

(2) Réocreux, R.; Kress, P. L.; Hannagan, R. T.; Çınar, V.; Stamatakis, M.; Sykes, E. C. H. Controlling Hydrocarbon (De)Hydrogenation Pathways with Bifunctional PtCu Single-Atom Alloys. *J. Phys. Chem. Lett.* **2020**, *11* (20), 8751–8757. https://doi.org/10.1021/acs.jpclett.0c02455.

(3) Ouyang, M.; Papanikolaou, K. G.; Boubnov, A.; Hoffman, A. S.; Giannakakis, G.; Bare, S. R.; Stamatakis, M.; Flytzani-Stephanopoulos, M.; Sykes, E. C. H. Directing Reaction Pathways via in Situ Control of Active Site Geometries in PdAu Single-Atom Alloy Catalysts. *Nat. Commun.* **2021**, *12* (1), 1–11. https://doi.org/10.1038/s41467-021-21555-z.

(4) Rupprechter, G.; Weilach, C. Spectroscopic Studies of Surface-Gas Interactions and Catalyst Restructuring at Ambient Pressure: Mind the Gap! *J. Phys. Condens. Matter* **2008**, *20* (18). https://doi.org/10.1088/0953-8984/20/18/184019.

(5) Giannakakis, G.; Trimpalis, A.; Shan, J.; Qi, Z.; Cao, S.; Liu, J.; Ye, J. NiAu Single Atom Alloys for the Non-Oxidative Dehydrogenation of Ethanol to Acetaldehyde and Hydrogen. *Top. Catal.* **2018**, *61* (5), 475–486. https://doi.org/10.1007/s11244-017-0883-0.

(6) Van Spronsen, M. A.; Daunmu, K.; O'Connor, C. R.; Egle, T.; Kersell, H.; Oliver-Meseguer, J.; Salmeron, M. B.; Madix, R. J.; Sautet, P.; Friend, C. M. Dynamics of Surface Alloys: Rearrangement of Pd/Ag(111) Induced by CO and O2. *J. Phys. Chem. C* **2019**, *123* (13), 8312–8323. https://doi.org/10.1021/acs.jpcc.8b08849.

(7) Gao, F.; Wang, Y.; Goodman, D. W. CO Oxidation over AuPd(100) from Ultrahigh Vacuum to near-Atmospheric Pressures: CO Adsorption-Induced Surface Segregation and Reaction Kinetics. *J. Phys. Chem. C* **2009**, *113* (33), 14993–15000. https://doi.org/10.1021/jp9053132.

(8) Patel, D. A.; Kress, P. L.; Cramer, L. A.; Larson, A. M.; Sykes, E. C. H. Elucidating the Composition of PtAg Surface Alloys with Atomic-Scale Imaging and Spectroscopy. *J. Chem. Phys.* **2019**, *151* (16). https://doi.org/10.1063/1.5124687.